TKK Dissertations 107
Espoo 2008

POWER TRANSMISSION LINE FAULT LOCATION BASED ON CURRENT TRAVELING WAVES

Doctoral Dissertation

Abdelsalam Mohamed Elhaffar

Helsinki University of Technology
Faculty of Electronics, Communications and Automation
Department of Electrical Engineering

TKK Dissertations 107
Espoo 2008

POWER TRANSMISSION LINE FAULT LOCATION BASED ON CURRENT TRAVELING WAVES

Doctoral Dissertation

Abdelsalam Mohamed Elhaffar

Dissertation for the degree of Doctor of Science in Technology to be presented with due permission of the Faculty of Electronics, Communications and Automation for public examination and debate in Auditorium S3 at Helsinki University of Technology (Espoo, Finland) on the 25th of March, 2008, at 12 noon.

Helsinki University of Technology
Faculty of Electronics, Communications and Automation
Department of Electrical Engineering

Teknillinen korkeakoulu
Elektroniikan, tietoliikenteen ja automaation tiedekunta
Sähkötekniikan laitos

Distribution:
Helsinki University of Technology
Faculty of Electronics, Communications and Automation
Department of Electrical Engineering
P.O. Box 3000
FI - 02015 TKK
FINLAND
URL: http://powersystems.tkk.fi/eng/
Tel. +358-9-4511
Fax +358-9-451 5012
E-mail: abdelsalam.elhaffar@tkk.fi

ISBN 978-951-22-9244-8
ISBN 978-951-22-9245-5 (PDF)
ISSN 1795-2239
ISSN 1795-4584 (PDF)
URL: http://lib.tkk.fi/Diss/2008/isbn9789512292455/

TKK-DISS-2436

Multiprint Oy
Espoo 2008

ABSTRACT OF DOCTORAL DISSERTATION	HELSINKI UNIVERSITY OF TECHNOLOGY P.O. BOX 1000, FI-02015 TKK http://www.tkk.fi

Author   Abdelsalam Mohamed Elhaffar

Name of the dissertation
Power Transmission Line Fault Location based on Current Traveling Waves

Manuscript submitted October 20th, 2007	Manuscript revised January 10th, 2008

Date of the defense   March 25th, 2008

☒ Monograph	☐ Article dissertation

Faculty	Faculty of Electronics, Communications and Automation
Department	Department of Electrical Engineering
Field of research	Power systems
Opponent(s)	Prof. Mustafa Kizilcay and Dr. Seppo Hänninen
Supervisor	Prof. Matti Lehtonen
Instructor	Prof. Matti Lehtonen

Abstract

Transmission lines are designed to transfer electric power from source locations to distribution networks. However, their lengths are exposed to various faults. Protective relay and fault recorder systems, based on fundamental power frequency signals, are installed to isolate and the faulty line and provide the fault position. However, the error is high especially in transmission lines. This thesis investigates the problem of fault localization using traveling wave current signals obtained at a single-end of a transmission line and/or at multi-ends of a transmission network. A review of various signal processing techniques is presented. The wavelet transform is found to be more accurate than conventional signal processing techniques for extracting the traveling wave signals from field measurements.

In this thesis, an optimization method has been developed to select the best wavelet candidate from several mother wavelets. The optimum mother wavelet was selected and used to analyze the fault signal at different details' levels. The best details' level, which carries the fault features, was selected according to its energy content. From the line and network data, the traveling wave speed is calculated for each line using the optimum mother wavelet at different detail levels. Accurate determination fault location depends on the proper details wavelet level as well as the propagation speed. A high frequency current transformer model has been verified experimentally using impulse current signals at the high voltage laboratory, Helsinki University of Technology.

Single-end method has been studied for several transmission line configurations, including lines equipped with/without overhead ground wires, counterpoises, or overhead ground wires and counterpoises. The time difference between the aerial and ground mode has also been investigated for these line configurations.

Multi-ended method, using recordings sparsely located in the transmission network, has been proposed to overcome the weakness of the single-end method. The method is based on extracting the fault transient signals from at least two monitored buses and using the double-end method assisted by the shortest path algorithm is used to find the minimum travel time of these signals to the nearest bus.

Validation of the fault location is performed using the ATP/EMTP transient simulations. The method is verified using field data from five traveling wave recorders installed at pre-selected buses of the Finnish 400-kV transmission network.

The algorithm will allow utilities to accurately locate line faults the knowledge of transient current signals, network topology, and the shortest-path algorithm. The thesis, which genuinely provides an economic approach to fault location of transmission systems consistent with today's needs, provides a good foundation for further developments.

Keywords   transmission lines, fault location, traveling waves, current transformers, signal processing, wavelet transform.

ISBN (printed)	978-951-22-9244-8	ISSN (printed)	1795-2239
ISBN (pdf)	978-951-22-9245-5	ISSN (pdf)	1795-4584
Language	English	Number of pages	108 p. + app. 14 p.

Publisher   Helsinki University of Technology, Faculty of Electronics, Communications and Automation

Print distribution   Helsinki University of Technology, Faculty of Electronics, Communications and Automation

☒ The dissertation can be read at http://lib.tkk.fi/Diss/2008/isbn9789512292455

Acknowledgement

When I was a protection engineer, I found power system protection and fault location an interesting job after commencing my career. However, the development in digital signal processing and numerical techniques applied to protection systems motivated me to study this subject area. Till now, I consider the subject of power system protection as a hobby. When I started my study in TKK, I found that accurate location of power line faults is a crucial point in deregulated electricity networks. At this point, I would like to express my sincere gratitude to Prof. Matti Lehtonen for his invaluable guidance, encouragement, and support throughout this work. Also, the fruitful discussions with Dr. Naser Tarhuni, Dr. Hassan El-Sallabi, Dr. Nagy Elkalashy, and Dr. Mohammed Elmusrati have been greatly helpful in preparing this thesis. I also acknowledge the language corrections made by Mr. Emad Dlala. I am also grateful to the high voltage laboratory team, who offered the possibility for current transformer tests. I owe special thanks to the Finnish electricity transmission operator (FinGrid Oyj) for providing the traveling wave measurements of the 400-kV network. The financial support provided by the Libyan Authority of Graduate Studies and Helsinki University of Technology are thankfully acknowledged. Thanks to the Fortum personal grant (B3) for supporting the writing of this dissertation in 2008. My deepest thanks also go to my family for their patience and support during the preparation and writing of this thesis.

Espoo, February 20^{th}, 2008

Abdelsalam Elhaffar

Abbreviations

ATP	Alternative Transients Program
ATPDraw	A preprocessor for ATP
CCA	Cross Correlation Analysis
CT	Current Transformer
CWT	Continuous Wavelet Transform
DFT	Discrete Fourier Transform
DWT	Discrete Wavelet Transform
EMTP	Electromagnetic Transient Program
EHV	Extra High Voltage($\geq$ 400-kV)
FFT	Fast Fourier Transform
GMR	The self Geometric Mean Radius
GMD	The Geometric Mean Distance
GPS	Global Positioning System
GW	Ground Wire
HP	High-Pass filter
IED	Intelligent Electronic Devices
LCC	Line/Cable Constants program
MTD	Mean Time Delay
MThr	Mean Threshold value
MaxPower	Maximum value of the power delay profile
SCADA	Supervisory Control And Data Acquisition
SNR	Signal to Noise Ratio
STFT	Short Time Fourier Transform
TW	Traveling Wave
TWR	Traveling Wave Recorder
TDR	Time Domain Reflectometery
Ts	Sampling Time [sec]
T_i	Current transformation matrix
WTC	Wavelet Transform Coefficients
WCF	Wavelet Correlation Function

Symbols

α	Attenuation constant [Nepers/m]
Y	Admittance [℧]
C	Capacitance[F]
C_{ps1}	Capacitance between the primary winding (P) and secondary (S1) of the CT
C_{s1s2}	Capacitance between the secondary (S1) and secondary (S2) of the CT
C_{s1}	Capacitance between the secondary (S1) and the ground of the CT
Z_0	Characteristic impedance [Ω]
G	Conductance [℧]
ψ	Electric flux [A.s]
L	Inductance [H]
Z_p	Leakage impedance of the CT primary
Z_{s1}	Leakage impedance of the CT secondary 1
L_{m1}	Magnetizing inductance of secondary (S1) of the CT
R_{m1}	Magnetizing resistance of secondary (S1) of the CT
Z_{scs1}	Measured short circuit impedance from the CT primary (P) to secondary (S1)
ϕ	Magnetic flux [Wb]
Ψ	Mother wavelet
v	Propagation speed [km/s]
γ	Propagation constant
R	Resistance [Ω]
Z_{b1}	Secondary burden of secondary (S1) of the CT
t	Time [s]

Table of Contents

List of Tables

List of Figures

Chapter 1

Introduction

An electric power system comprises of generation, transmission and distribution of electric energy. Transmission lines are used to transmit electric power to distant large load centers. The rapid growth of electric power systems over the past few decades has resulted in a large increase of the number of lines in operation and their total length. These lines are exposed to faults as a result of lightning, short circuits, faulty equipments, mis-operation, human errors, overload, and aging. Many electrical faults manifest in mechanical damages, which must be repaired before returning the line to service. The restoration can be expedited if the fault location is either known or can be estimated with a reasonable accuracy. Faults cause short to long term power outages for customers and may lead to significant losses especially for the manufacturing industry. Fast detecting, isolating, locating and repairing of these faults are critical in maintaining a reliable power system operation. When a fault occurs on a transmission line, the voltage at the point of fault suddenly reduces to a low value. This sudden change produces a high frequency electromagnetic impulse called the traveling wave (TW). These traveling waves propagate away from the fault in both directions at speeds close to that of light. To find the fault, the captured signal from instrument transformers has to be filtered and analyzed using different signal processing tools. Then, the filtered signal is used to detect and locate the fault. It is necessary to measure the value, polarity, phase, and time delay of the incoming wave to find the fault location accurately. The main objective of this thesis is to analyze the methods of the fault location based on the theory of traveling waves in high voltage transmission lines [1]. The importance of this research arises from the need to reduce the interruptions of electricity, especially for interconnecting transmission lines and to reduce the repair and restoration time especially in areas with difficult terrain. The restoration time also includes the time to find the fault location. This can be attained by reducing the error in the fault distance estimation.

There is no doubt that quick effective repair and maintenance processes directly lead to improve the power availability to the consumers which, consequently, enhance the overall efficiency of the power networks. These concepts of availability, efficiency and quality have an increasing importance nowadays due to the new marketing policies resulting from deregulation and liberalization of power and energy markets. Saving time and effort, increasing the power availability and avoiding future accidents can be directly interpreted as a cost reduction or a profit increasing.

In this thesis, we have developed single and multi-end methods of traveling wave fault location which use current signal recordings of the Finnish 400-kV network obtained from traveling wave recorders (TWR) sparsely located in the transmission network. The TWRs are set to record 4 milliseconds of data using an 8-bit resolution and a sampling rate of 1.25 MHz. The record includes both pre-trigger and post-trigger data. Although the single-ended fault location method is less expensive than the double-ended method, since only one unit is required per line and a communication link is not required, the errors remain high when using the advanced signal processing techniques [2]. Furthermore, the fault location error needs more improvement considering single-end method. Multi-end method shows a promising economical solution considering few recording units.

1.1 Literature Review

The subject of fault location has been of considerable interest to electric power utility engineers for a long time. Fault detection and location methods that have been proposed and implemented so far can be broadly classified as those using the power frequency phasors in the post-fault duration [3] - [12], using the differential equation of the line and estimating the line parameters [13] - [19], and using traveling waves including traveling wave protection systems [20] - [42]. The traveling wave technique has been applied to the protection of transmission systems with several practical implementations [43] - [66]. Traveling wave techniques are more accurate than reactance techniques in overhead line fault location, providing accuracies in the range of 100 - 500 m. In [67], a detailed review of different fault location techniques was presented. Traveling wave-based overhead line fault locators are classified by mode of operation - types A, B, C, D, and E [24], [26], [32].

Type A, is a single-ended passive method which uses the transient captured at only one end of the circuit and relies on the busbar and other connected lines to present a sufficiently large discontinuity to cause some of the arriving energy to be reflected back into the faulty line where it will be re-reflected from the fault. When a flashover occurs at the fault point, it launches two waves, which travel in opposite directions away from the fault position. The fault arc is assumed to remain ionized for an extended period of time and to present a resistance much lower than the characteristic impedance of the line so that almost all of the energy in the transients arriving at the fault point is totally reflected. The impedances presented by the substation busbars at sending and receiving ends are also assumed to be much lower than the characteristic impedance of the line so that any traveling waves are again totally reflected back into the faulty line. Type A transients are produced at both ends of the line. At the sending-end bus, the time interval between first two consecutive pulses is proportional to the distance to the fault point from the sending end bus. In practice, the effective fault resistance may not cause total reflection of the energy arriving at the fault and some fraction will pass through, appearing at the opposite end of the line. Under these conditions, the transients will be more complex and may require careful analysis to identify the correct pulses. Further complications arise if the arc at the fault point extinguishes prematurely. However, it is not important when the fault arc is distinguished by itself. The difficulty increases further in situations where there are multiple paths over which pulses can travel and/or where intermediate discontinuities cause the original pulses to subdivide and produce additional pulses and reflections.

Type B is a passive double-ended method. The arrival of the transient generated by the fault at one end of the line is used to start a timer. The timer is stopped by a signal, which is sent from a detector that indicated the arrival of the fault generated transient at the far end. Hence, the fault position can be calculated if the line length is known.

Type C is an active single-ended method that involves injecting an impulse into the line when a fault is detected and it is usually referred to as time-domain reflectometery (TDR). The fault distance was calculated using the time difference between the injection of pulse and the receipt of the reflection from the fault arc. Difficulties of analyzing the TW transients may arise for Type A if the duration of the fault arc is short or the effective fault resistance is high. The difficulty increases when there are multiple paths and/or intermediate discontinuities. Interpretation problems are eliminated with type D mode of operation, which does not depend on multiple reflections between the substation busbar and the fault but rather on the time of arrivals of the initial TW transients at both line ends. The duration of the fault arc in the period following the breakdown is no longer important nor do line discontinuities and multiple paths complicate the measurement. The crucial issue in type D mode is the provision of accurate time synchronization and telecommunication. To achieve accurate time tagging of the event, the detectors are synchronized to a Global Positioning System (GPS) clock that provides time synchronization accuracies of less than 1 μsec over the entire surface of the Earth under all weather conditions [38] - [42]. Telecommunication, which does not have to be online, can be used through any convenient channel including microwave, optical fibre or Supervisory control and data acquisition (SCADA) network [67].

Type E mode of operation is a single-ended mode that uses the transients created after reclosing a circuit breaker onto a dead line. It is similar to TDR used in cable fault location. Type E was originally developed to study the behavior of traveling waves on high voltage transmission lines without involving the use of actual fault throwing or waiting for faults to occur naturally. This technique could be used for the determination of the effective speed of propagation and also as a method of detecting and locating broken conductors where little or no fault current is flowing. In three-phase reclosing, the substation busbar and line circuit breaker act as three generators with firing times and output voltages which vary between the phases due to the different points-on-wave at which each pole pre-strikes. This means that the voltage injected onto each phase will vary in polarity and amplitude, as well as the time of application. It also means that the voltages applied to each phase on successive re-closures of the line breaker will be different.

Most of the fault location schemes are based on voltage traveling wave propagation on the transmission line. However, this dissertation focuses on current transient signals. The reason is that the conventional current transformers (CTs) can reproduce the current transients with sufficient accuracy in their secondary circuits up to several hundreds of kilohertz [57], [107], [108]. The high frequency signals are measured with an interposing split-core current transformer clamped on the substation protection secondary circuits of the conventional CT secondary circuits. Each interposing transducer includes a small air gap in the magnetic circuit creating a quadrature current transformer. The overall effect is similar to that of a Rogowski-coil, except that most of the magnetic circuit is composed of a high permeability material. Type A (single-ended) and type D (double-ended) traveling wave algorithms have been studied extensively in this dissertation. They have primarily been implemented by recording the time difference between successive reflections recorded at one end of the line and the arrival of the initial TW transient signals. To achieve this, different signal processing techniques have been employed, including cross correlation between the forward and backward traveling waves along the line [47] - [52], as well as wavelet analysis [57]. In the single-ended method, the fault transients, which is reflected from the fault point and arrive at the relay terminals, produce a highly correlated signal for a delay time equal to twice the traveling time of the transients to the fault location. This time can be then used to find the distance from the relay to the fault location. On the other hand, there are also some bottlenecks, which have already been reported in the literature [49]. These include: the problem of choosing a suitable time window for the correlation analysis, the requirement of high sampling rate and the associated computational burden, and the possibility of misidentification of faults due to excessive attenuation of signals, especially for remote faults.

1.2 Electromagnetic Transient Analysis

The simulation of the voltage and current transient is important for the design of the fault location algorithm, analysis of various possible fault conditions and the proper functioning of the fault locator. The graphical method of Bewley Lattice (1961) becomes a cumbersome technique for large networks and digital simulation methods are usually applied [1]. However, the general principle of the graphical approach has been used to develop computer programs applicable to large systems. A more powerful method has been developed by the Bonneville power adminstration known as EMTP [68]. The selected transient simulator for this thesis is the Alternative Transients Program (ATP/EMTP) [69]. The ATP is based on the Electromagnetic Transient Program (EMTP) used by the power engineers and researchers for transient simulations. The ATP contains extensive modeling capabilities for transmission lines, cables, breakers, loads, converters, protection devices, non-linear elements, electromagnetic coupling, and major power electronics devices and equipment. The ATP has an enhanced graphical user interface called ATPDraw as a preprocessor, which allows an easy entry of system topology and data [70]. The ATP/EMTP contains various models to represent overhead transmission lines. These models can account for tower geometry, bundling and earth resistivity. The user can select any of these models for overhead transmission lines such as lumped or distributed parameters; frequency independent or frequency dependent models. The choice of the overhead transmission line model is dependent on a number of factors, such as the length of the lines, the nature of the simulation (faults, surges, dynamic stability, etc), and the fidelity of the results. The following are the various options for transmission line models in the ATP/EMTP

[69]:

1. Bergeron line model is a distributed parameter model including the traveling wave phenomena. However, it represents the line resistances at both ends as lumped elements.
2. PI-model: Nominal PI-equivalent model with lumped parameters, which is suitable for short lines' simulation.
3. Noda-model: Frequency-dependent model. This algorithm models the frequency dependent transmission lines and cables directly in the phase domain.
4. Semlyen-model: Frequency-dependent simple fitted model. The Semlyen model was one of the first frequency-dependent line models. It may give inaccurate or unstable solutions at high frequencies.
5. JMarti: Frequency-dependent model with constant transformation matrix that is suitable for simulating traveling wave phenomena in long transmission lines

The most useful part is the Line/Cable Constants program (LCC) model where the geometrical and material data of the line/cable has to be given only. Skin effect, bundling and transposition can automatically be taken into consideration. JMarti frequency-dependent line model has been adopted in this thesis as it shows a good correlation with actual line responses [71].

1.3 A Typical Transmission System

The power system in Finland consists of power plants, the main grid, regional networks, distribution networks, and consumers of electricity. The Finnish system is a part of the Nordic power system together with the systems in Sweden, Norway and Eastern Denmark. Moreover, there is a direct current connection from Russia and Estonia to Finland, enabling connection between these systems which apply different principles. Correspondingly, the Nordic power system has been connected to the system in continental Europe through direct current connections.

Fingrid Oyj company is responsible for the operational planning and supervision of the main grid and for grid maintenance and grid development. The main grid serves power producers and consumers, enabling electricity trade between these throughout Finland and also across Finnish borders. The main grid in Finland encompasses approximately 4100 km of 400-kV

transmission lines, 2350 km of 220-kV transmission lines, 7500 km of 110-kV transmission lines and 106 substations. The Finnish grid has mainly been constructed using outdoor substations and transmission lines. Underground cables are rarely used. Gas-insulated switchgears are used, when the space available is very limited. Regional networks are connected to the main grid, and they transmit electricity regionally, usually by means of one or more 110-kV lines. Distribution networks are either connected directly to the main grid or they utilize the grid services through a regional network. Distribution networks operate at a voltage level of 0.4 to 110-kV [72].
The transmission system under investigation is a part of the Finnish power system which consists of 400-kV and 110-kV lines. The transmission network transmits the power from generators to the distribution systems which includes the generators' step-up transformer up to the 110-kV bushings of the 110/20 kV transformers. The 400-kV transmission network is effectively earthed at every substation, usually using a low-reactance earthing coil. There are only few transformer neutrals that are directly earthed.

The Finnish system is connected to the Russian transmission system by a back-to-back HVDC link connection for power importing only. Also several 400-kV AC lines and one HVDC link are connecting Finland with Sweden; a 220-kV AC line is connecting Finland with Sweden for both power import and export. At the northern Norwegian borders, Finland is connected to the generation area by a 220-kV line [74].

About 78 % of faults that occur in the transmission networks of the Finnish transmission system are earth faults during a period of 10 years until 2006. This gives a necessity for locating this kind of faults. In Finland, traveling waves considered to be the main fault location method at the 400-kV voltage level. Five traveling wave recorders (TWRs) were installed permanently at preselected substations so that they can cover all possible faults of the monitored grid. The challenge is how to locate the fault with only these five units using current traveling waves. The TWR is connected to the secondary circuits of conventional current transformers (CTs) through inductive split-core couplers with a sample rate of 1.25 MHz. The major transmission line construction is a flat horizontal configuration. All 400-kV lines are shielded with two ground conductors. In the 110-kV network, only 3.2 % of the 110-kV overhead lines are without shield wires [72], [73].

1.4 Organization of Thesis

This thesis consists of seven chapters including the introduction. Chapter 2 presents an introduction to the theory of traveling waves. Fault location signal processing techniques are discussed in Chapter 3. Current transformer high frequency modeling is discussed in Chapter 4. Analysis of the single-end method is illustrated in Chapter 5. The multi-ended method is introduced in Chapter 6. Finally, Chapter 7 concludes the dissertation and outlines future work.

1.5 Contributions

In this thesis, an improved single-ended method for earth fault location using wavelet correlation of the optimum details level for transient current signals has been proposed. The wavelet transform has been used to extract the high frequency content of the traveling wave signals from the recorded fault signals at different frequency bands. The use of wavelet correlation function provides a more accurate method in defining the reflections from the fault position in the transmission line and gives an improved method in fault location using traveling waves. The selection of the optimum wavelet has been performed using the minimum norm error between the original signal and the reconstructed one. The optimum details level has been selected using their maximum energy content and the dominant frequency of the transient signal. The main contribution of this part is the use of the time delay between the aerial and ground modes of the optimum details level of the current signal for unshielded transmission lines. This time delay is used to distinguish between remote-end and close-in faults. However, following an extensive analysis of recorded current TW signals from the 400-kV Finnish grid, the author has observed that most of the ground mode signal passes through the ground wires and only a small part of it passes through the ground. This may pose some difficulties in recognizing the time difference between the aerial and ground modes.

Alternatively, the author proposed the use of the second reflected signal's polarity to distinguish between close-in and remote-end faults.

Current transformer modeling is carried out and experimentally verified using high current impulse signals. The last contribution is the use of traveling wave recording units (TWR) for capturing the fault transient signals when the number. Then, using the double-end method assisted by the Dijkstra shortest path algorithm to find the minimum travel time of these signals to the measurement buses.

Chapter 2

Traveling Waves

Studies of transient disturbances on transmission systems have shown that changes are followed by traveling waves, which at first approximation can be treated as a step front waves. As this research is focused on traveling wave based fault location, it was decided to employ an introductory chapter to the basic theory of traveling waves.

2.1 Introduction

The transmission line conductors have resistances and inductances distributed uniformly along the length of the line. Traveling wave fault location methods are usually more suitable for application to long lines. A representation of an overhead transmission line by means of a number of pi-sections has been implemented using the Alternative Transient Program (ATP/EMTP) in which the properties of the electric field in a capacitance and the properties of the magnetic field in an inductance have been taken into account and these elements are connected with lossless wires.

Transmission lines cannot be analyzed with lumped parameters, when the length of the line is considerable compared to the wavelength of the signal applied to the line. Power transmission lines, which operate at 50-Hz and are more than 80-km long, are considered to have distributed parameters. These lines have the properties of voltage and current waves that travel on the line with finite speed of propagation. Traveling wave methods for transmission lines fault location have been reported since a long time. Subsequent developments employ high speed digital recording technology by using the traveling wave transients created by the fault. It is well known that when a fault occurs in overhead transmission lines systems, the abrupt changes in voltage and current at the point of the fault generate high frequency electromagnetic impulses called traveling waves which propagate along the transmission line in both directions away from the fault point.These transients travel along the lines and are reflected at the line terminals following the rules of Bewley's Lattice Diagrams [1]. Propagation of transient signals along multiphase lines can be better observed by decomposing them into their modal components. If the times of arrival of the traveling waves in the two ends of the transmission line can be measured precisely, the fault location then can be determined by comparing the difference between these two arrival times of the first consecutive peaks of the traveling wave signal. The main reasons behind choosing the current traveling wave transients in this research are that they are generally much less distorted than voltage transients and also the normal line protection current transformers can reproduce the current transient with sufficient accuracy in their secondary circuits.

2.2 The Transmission Line Equation

A transmission line is a system of conductors connecting one point to another and along which electromagnetic energy can be sent. Power transmission lines are a typical example of transmission lines. The transmission line equations that govern general two-conductor uniform transmission lines, including two and three wire lines, and coaxial cables, are called the telegraph equations. The general transmission line equations are named the telegraph equations because they were formulated for the first time by Oliver Heaviside (1850-1925) when he was employed by a telegraph company and used to investigate disturbances on telephone wires [75]. When one considers a line segment *dx* with parameters resistance (*R*), conductance (*G*), inductance (*L*), and capacitance (*C*), all per unit length, (see Figure 2.1) the line constants for segment *dx* are *R dx*, *G dx*, *L dx*, and *C dx*. The electric flux ψ and the magnetic flux ϕ created by the electromagnetic wave, which causes the instantaneous voltage *u(x,t)* and current *i(x,t)*, are

$$d\psi(t) = u(x,t)C\mathrm{d}x \tag{2.1}$$

and

$$d\phi(t) = i(x,t)L\mathrm{d}x \tag{2.2}$$

Calculating the voltage drop in the positive direction of *x* of the distance *dx* one obtains

$$u(x,t) - u(x+\mathrm{d}x,t) = -du(x,t) = -\frac{\partial u(x,t)}{\partial x}\mathrm{d}x = \left(R + L\frac{\partial}{\partial t}\right) i(x,t)\mathrm{d}x \tag{2.3}$$

If *dx* is cancelled from both sides of (2.3), the voltage equation becomes

$$\frac{\partial u(x,t)}{\partial x} = -L\frac{\partial i(x,t)}{\partial t} - Ri(x,t) \tag{2.4}$$

Similarly, for the current flowing through *G* and the current charging *C*, Kirchhoff's current law can be applied as

$$i(x,t) - i(x+\mathrm{d}x,t) = -di(x,t) = -\frac{\partial i(x,t)}{\partial x}\mathrm{d}x = (G + C\frac{\partial}{\partial t})u(x,t)\mathrm{d}x \tag{2.5}$$

If *dx* is cancelled from both sides of (2.5), the current equation becomes

$$\frac{\partial i(x,t)}{\partial x} = -C\frac{\partial u(x,t)}{\partial t} - Gu(x,t) \tag{2.6}$$

The negative sign in these equations is caused by the fact that when the current and voltage waves propagate in the positive *x*-direction, *i(x, t)* and *u(x, t)* will decrease in amplitude for increasing x. When one substitutes

$Z = R + \frac{\partial L(x,t)}{\partial t}$ and $Y = G + \frac{\partial C(x,t)}{\partial t}$

and differentiate once more with respect to *x*, we get the second-order partial differential equations

$$\frac{\partial^2 i(x,t)}{\partial x^2} = -Y\frac{\partial u(x,t)}{\partial t} = YZi(x,t) = \gamma^2 i(x,t) \tag{2.7}$$

$$\frac{\partial^2 u(x,t)}{\partial x^2} = -Z\frac{\partial i(x,t)}{\partial t} = ZYu(x,t) = \gamma^2 u(x,t) \tag{2.8}$$

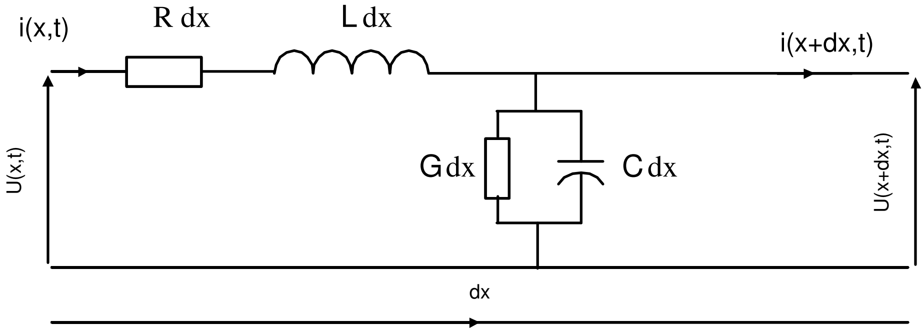

Figure 2.1: Single-phase transmission line model.

In this equation, γ is a complex quantity which is known as the propagation constant, and is given by

$$\gamma = \sqrt{ZY} = \alpha + j\beta \tag{2.9}$$

where, α is the attenuation constant which has an influence on the amplitude of the traveling wave, and β is the phase constant which has an influence on the phase shift of the traveling wave.

Equation (2.7) and Equation (2.8) can be solved by transform or classical methods in the form of two arbitrary functions that satisfy the partial differential equations. Paying attention to the fact that the second derivatives of the voltage *v* and current *i* functions, with respect to *t* and *x*, have to be directly proportional to each other, means that the solution can be any function as long as both independent variables *t* and *x* appear in the form [76]

$$u(x,t) = A_1(t)e^{\gamma x} + A_2(t)e^{-\gamma x} \tag{2.10}$$

and

$$i(x,t) = -\frac{1}{Z}[A_1(t)e^{\gamma x} - A_2(t)e^{-\gamma x}] \tag{2.11}$$

where *Z* is the characteristic impedance of the line and is given by

$$Z = \sqrt{\frac{R + L\frac{\partial}{\partial t}}{G + C\frac{\partial}{\partial t}}} \tag{2.12}$$

where A_1 and A_2 are arbitrary functions, independent of *x*.

2.3 The Lossless Line

Power transmission lines are normally of the three-phase type. However, it is much simpler to understand traveling wave concepts and associated methods by first considering wave propagation in single-phase lines. In the case of the lossless line, the series resistance *R* and the parallel conductance *G* are zero, the inductance and capacitance are constants. The transmission line equations become

$$\frac{\partial u}{\partial x} = -L\frac{\partial i}{\partial t} \tag{2.13}$$

and

$$\frac{\partial i}{\partial x} = -C\frac{\partial u}{\partial t} \tag{2.14}$$

since there is no damping, substituting the "steady wave" solution: $u = Z_0\, i$ into Equations (2.13) and (2.14),

$$Z_0\frac{\partial i}{\partial x} = -L\frac{\partial i}{\partial t} \tag{2.15}$$

and

$$\frac{\partial i}{\partial x} = -Z_0 C\frac{\partial i}{\partial t} \tag{2.16}$$

Dividing Equation (2.15) by Equation (2.16) yields

$$Z_0 = \sqrt{\frac{L}{C}} \tag{2.17}$$

which is the characteristic impedance of the lossless line. This implies that the voltage and current waves travel down the line without changing their shapes [77].

$$\frac{\partial^2 u}{\partial x^2} = LCu \tag{2.18}$$

Equation (2.18) is the so-called traveling-wave equation of a loss-less transmission line. The solutions of voltage and current equations reduce to [75]

$$u(x,t) = A_1(t)e^{\frac{x}{v}} + A_2(t)e^{-\frac{x}{v}} \tag{2.19}$$

and

$$i(x,t) = -\frac{1}{Z_0}[A_1(t)e^{\frac{x}{v}} - A_2(t)e^{-\frac{x}{v}}] \tag{2.20}$$

where v is the traveling wave propagation speed defined as

$$v = \frac{1}{\sqrt{LC}} \tag{2.21}$$

When Taylor's series is applied to approximate a function by a series,

$$A(t+h) = A(t) + hA'(t) + \left(\frac{h^2}{2!}\right)A''(t) + ... = (1 + hp + \frac{h^2}{2}p^2 + ...)A(t) = e^{hp}A(t) \tag{2.22}$$

where p is the Heaviside operator $p = \frac{\partial}{\partial t}$.

Applying this to Equation (2.19) and Equation (2.20), the solutions for the voltage and current waves in the time domain can be satisfied by the general solution (also as showed by D'Alembert [76]):

$$u(x,t) = A_1(t + \frac{x}{v}) + A_2(t - \frac{x}{v}) \tag{2.23}$$

$$i(x,t) = -\frac{1}{Z_0}\left[A_1(t + \frac{x}{v}) - A_2(t - \frac{x}{v})\right] \tag{2.24}$$

In this expression, $A_1(t + \frac{x}{v})$ is a function describing a wave propagating in the negative *x*-direction, usually called the backward wave, and $A_2(t - \frac{x}{v})$ is a function describing a wave propagating in the positive *x*-direction, called the forward wave [78].

2.4 Propagation Speed

From the voltage drop equation,

$$u(x,t) - u(x + \mathrm{d}x, t) = (L\mathrm{d}x)\,\frac{\partial i(x,t)}{\partial t} \tag{2.25}$$

since u = Z_0 i, then

$$i(x,t) - i(x + \mathrm{d}x, t) = \left(\frac{L}{Z_0}\mathrm{d}x\right)\frac{\partial i(x,t)}{\partial t} \tag{2.26}$$

Making $\frac{\partial i(x,t)}{\partial t}$ finite we get:

$$i(x,t) - i(x + \mathrm{d}x, t) = \left(\frac{L}{Z_0}\mathrm{d}x\right)\frac{i(x,t) - i(x + \mathrm{d}x, t)}{\mathrm{d}t} \tag{2.27}$$

If the wave propagates intact

$$v = \frac{dx}{dt} = \frac{Z_0}{L}v = \frac{1}{\sqrt{LC}} \tag{2.28}$$

which is the traveling wave propagation speed.

2.5 Reflection and Refraction of Traveling Waves

When an electromagnetic wave propagates along a transmission line with a certain characteristic impedance, there is a fixed relation between the voltage and current waves. But what happens if the wave arrives at a discontinuity, such as an open circuit or a short circuit, or at a point on the line where the characteristic impedance (Equation 2.17) changes. Because of the mismatch in characteristic impedance, an adjustment of the voltage and current waves must occur. At the discontinuity, a part of the energy is let through and a part of the energy is reflected and travels back. At the discontinuity, the voltage and current waves are continuous. In addition, the total amount of energy in the electromagnetic wave remains constant, if losses are neglected. Figure 2.2 shows the case in which an overhead transmission line is short-circuited at the first half of its length. The reflection coefficient for the voltage at the receiving end of the line is defined as

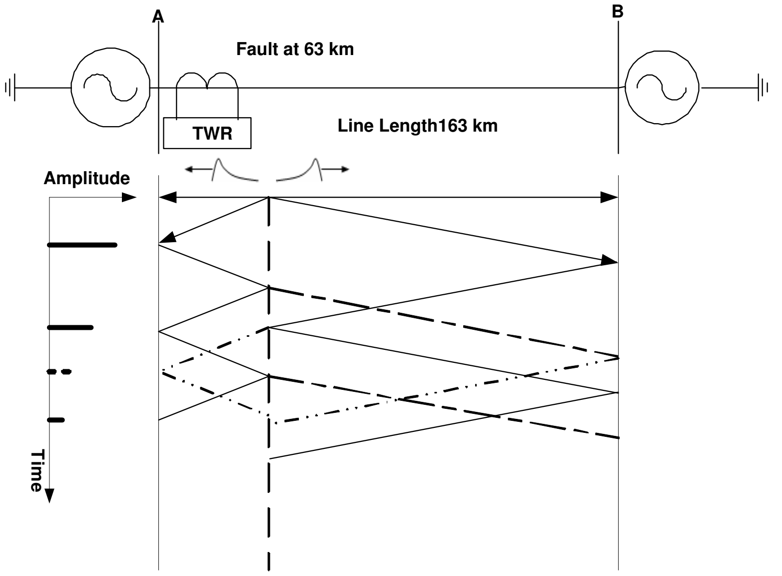

Figure 2.2: Lattice diagram for a fault at the first half of a transmission line

$$\rho_{rv} = \frac{Z_R - Z_0}{Z_R + Z_0} \tag{2.29}$$

Where Z_0 is a characteristic impedance of the line and Z_R is the termination impedance. Similar coefficients can be obtained for the currents, but the current reflection coefficient equals the negative of the voltage reflection coefficient value.

$$\rho_{ri} = \frac{Z_0 - Z_R}{Z_0 + Z_R} = -\rho_{rv} \tag{2.30}$$

As a special case, termination in a short circuit results in ρ_r = -1 for the voltage signals and ρ_{ri} = 1 for current signals. If the termination is an open circuit, Z_R is infinite and ρ_r = 1 in the limit for the voltage signal and ρ_{ri} = -1 for the current signal.

For a traveling wave while propagating through the termination, the transmission (refraction) coefficient can be calculated as

$$\rho_t = \frac{2Z_R}{Z_R + Z_0} = \rho_r + 1 \tag{2.31}$$

Therefore, for a line terminated in a short circuit, the voltage of the backward (or reflected) wave is equal and opposite to the voltage of the forward (or incident) wave. Similarly, the current of the backward (or reflected) wave is equal and in phase with the current of the forward (or incident) wave.

When a traveling wave encounters an inductance (i.e. transformer) at a terminal of a transmission line, the inductance appears to be an open circuit initially because the initial current in the inductor is zero. Gradually, the current starts increasing, and ultimately, the inductance appears to be a short circuit. The wave reflected by the inductor initially has the same polarity as the polarity of the incident wave [1]. The transformers have high inductive reactance and therefore, the voltage and current traveling waves reflected by a transformer have initially the same polarities as the polarities of the incident waves. The traveling waves reflected from a transformer, therefore, do not exhibit the reflections as observed in the waves reflected from buses on which no transformers connected to them. On the other hand, a capacitance in the path of traveling waves appears to the wave as a short circuit initially. Gradually, the charge builds up on the capacitor and the capacitor acts as an open circuit [1].

2.6 Modal Analysis

Three-phase lines have significant electromagnetic coupling between conductors. By means of modal decomposition, the coupled voltages and currents are decomposed into a new set of modal voltages and currents, which each can be treated independently in a similar manner to the single-phase line. In 1963, Wedepohl established the basic fundamentals of matrix methods for solving polyphase systems using the phenomena of modal theory [117]. The aim of this section is to emphasize the basic outlines of the modal theory. For this purpose, the basic equations for a single conductor were described in Section 2.2. Here, the introduced analysis is expanded to cover the polyphase lines. Modal transformation is essentially characterized by the ability to decompose a certain group of coupled equations into decoupled ones excluding the mutual parts among these equations. This can be typically applied to the impedance matrices for coupled conductors as shown in Figure 2.3, where Z_s is the self-impedance, Z_m is the mutual-impedance, Z_{m_i} are modal surge impedances for ground mode and two aerial modes (*i*= 0, 1 and 2). Three of the constant modal transformation matrices for perfectly transposed lines are the Clarke, Wedepohl, and Karrenbauer transformations [79], [80], [81]. For a three-phase fully transposed line, the Clarke's transformation matrix can be used to obtain the ground and aerial mode signals from the three-phase transients. Depending on the tower geometry, modal components will travel at different speeds along the faulted line. Hence, the recorded fault transients at one end of the line will have time delays between their modal components. These delays cannot be readily recognized unless the signals are further processed by appropriate transformations. For power system applications, the measured voltages and currents can be transformed into their modal quantities. By modal transform, a three-phase system can be represented by an earth mode and two aerial modes. Each mode has a particular speed and characteristic impedance. In this thesis, the aerial mode signal is used in the fault distance estimation. The modal components can be obtained by

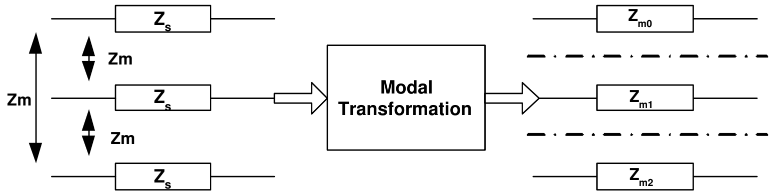

$$\begin{bmatrix} Z_s & Z_m & Z_m \\ Z_m & Z_s & Z_m \\ Z_m & Z_m & Z_s \end{bmatrix} \Rightarrow \begin{bmatrix} Z_{m_0} & 0 & 0 \\ 0 & Z_{m_1} & 0 \\ 0 & 0 & Z_{m_2} \end{bmatrix}$$

Figure 2.3: Modal transformation decoupling.

$$U_m = T_u^{-1} \times U_p \tag{2.32}$$

$$I_m = T_i^{-1} \times I_p \tag{2.33}$$

where *U* and *I* are the phase voltage and current components and the indices m and p are related to modal and phase quantities, respectively. T_u and T_i are the corresponding voltage and current transformation matrices. Thus, the modal impedance matrix Z_m can be found as

$$Z_m = T_u^{-1} \times Z \times T_i \tag{2.34}$$

For transposed lines, the transient current signals I_a, I_b, and I_c are transformed into their modal components using Clarke's transformation as follows [79]

$$\begin{bmatrix} I_0 \\ I_1 \\ I_2 \end{bmatrix} = \frac{1}{3} \begin{bmatrix} 1 & 1 & 1 \\ 2 & -1 & -1 \\ 0 & \sqrt{3} & -\sqrt{3} \end{bmatrix} \begin{bmatrix} I_a \\ I_b \\ I_c \end{bmatrix} \tag{2.35}$$

where I_0 is the ground mode current component, and I_1 and I_2 are known as the aerial mode current components for transposed lines. The ground mode current components I_0 are defined as zero sequence components of the symmetrical component system. The aerial mode current components I_1 flow in phase *a* and one half returns in phase *b* and one half in phase *c*. I_2 aerial mode current components are circulating in phases *b* and *c*.

Chapter 3

Fault Location Signal Processing Techniques

A traveling wave, a sharply varying signal, is a real challenge for the traditional mathematical methods. As a high-frequency signal, the traveling wave is difficult to separate from interference noise. In this regard, some signal processing techniques have been adopted. Typically, the traveling waves are mingled with noise as the traveling-wave-based fault location systems require a high sampling rate so that the fault information can be estimated accurately. In this chapter, various signal processing techniques are investigated concerning their application to fault location using traveling wave signals for overhead transmission line. These techniques enable the time-frequency representation of fault signals to be computed. Such computations are used to determine the most appropriate technique for the detection of the traveling waves under investigation. The analysis is carried out using TW output signals from the ATP/EMTP simulations for a typical power system with a single circuit overhead transmission line connecting two 400-kV buses as depicted in Figure 2.2.

3.1 Time Domain Approach

There has been a lot of attempts to determine the fault location using signal analysis in the time domain because of its simplicity. In this section, a review of some of these techniques is presented as especially those applied to traveling wave fault location.

3.1.1 Statistical Analysis

The objective of signal feature extraction is to represent the signal in terms of a set of properties or parameters. The most common measurements in statistics are the arithmetic mean, standard deviation and variance. All these parameters actually compute the value about which the data are centered. In fact, all measures of central tendency may be considered to be estimates of mean. The arithmetic mean of a sample may be computed as

$$\overline{x} = \frac{1}{n}\sum_{i=1}^{n} x_i \tag{3.1}$$

where x_i is the samples signal, $\bar{x}$ is the signal mean and *n* is the number of samples.
The standard deviation measures the dispersion of set of samples. It is most often measured by the deviation of the samples from their average. The sum of these deviations will be zero and the sum of squares of the deviations is positive. The standard deviation of a sample is computed as

$$s = \sqrt{\frac{1}{n-1}\sum_{i=1}^{n} (x_i - \overline{x})^2} \tag{3.2}$$

The variance is the average of the squared deviations as in the form

$$s^2 = \frac{1}{n-1}\sum_{i=1}^{n} (x_i - \overline{x})^2 \tag{3.3}$$

Another important parameter in statistical estimation method is called the auto-correlation coefficient, which measures the correlation between samples at different distance apart. It is closely related to convolution and, when applied to signals, provides a method of measuring the "similarity" between corresponding signals. The concept of cross-correlation analysis (CCA) is similar to ordinary correlation coefficient, namely that given *N* pairs of samples on two variables *x* and *y*, the correlation coefficient is given by [48]

$$R_{xy}(\tau) = \frac{1}{n}\sum_{k=1}^{n} (x_{k\Delta t+\tau} - \overline{x})(y_{k\Delta t} - \overline{y}) \tag{3.4}$$

where R_{xy} is the cross correlation function of the signals *x* and *y*, *n* is the number of samples, $\overline{x}$ is *x* mean, $\overline{y}$ is *y* mean and Δ *t* is sampling interval. The mean is removed to attenuate any exponential or power frequency signal. Correlation is a common operation in many signal processing techniques. Similar to the convolution except the function *x* is not "folded" about the origin but rather *x* is slided with respect to *y* and measure the area beneath. The delay at which the maximum correlation is achieved corresponds to the periodicity of both signals. The correlation between forward and backward current traveling waves can be evaluated using Equation (3.4). In this method, the similarity between the forward and backward current traveling wave shapes is compared and the correlation output of these waves gives the peaks. The time index of R_{xy} maximum value will give the fault position using the equation:

$$FD = \frac{v\ \tau}{2} \tag{3.5}$$

where *FD* is the distance from the measuring bus to the fault, *v* is the wave speed of the aerial mode (mode 1), and τ is the time delay of the correlation function maximum. A typical traveling wave signal is shown in Figure 3.1, where the *x* axes is converted to distance in km for a fault at 63-km from busbar A of the test case shown in Figure 2.2. The auto-correlation function of this signal is shown in Figure 3.2.

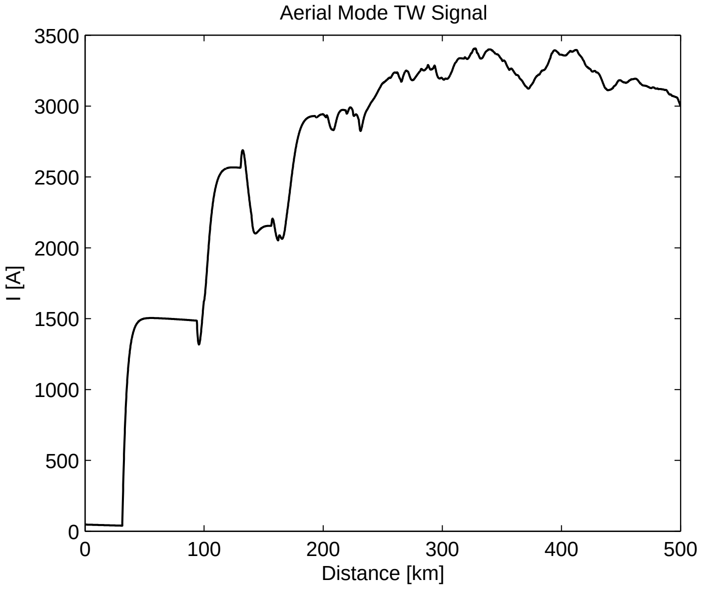

Figure 3.1: Aerial mode current signal for a fault at 63 km as a function of distance in km

Correlation techniques have been used in several traveling wave fault location schemes [47] - [52]. The disadvantages of the correlation techniques are the window length and the problem of identifying remote faults. The major disadvantage is the inaccurate fault distance estimation with high fault resistances. Cross correlation between the simulated and recorded current traveling wave signals also gives good results, but it needs continuous calibration according to the

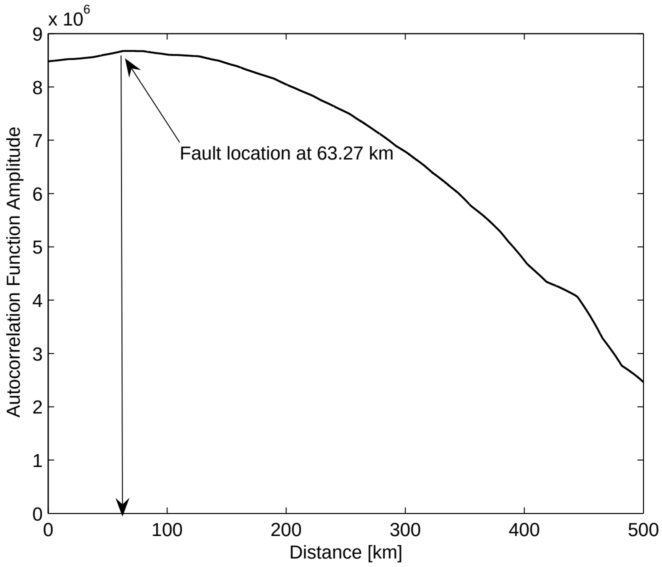

Figure 3.2: Auto-correlation function for a fault current signal at 63 km as a function of distance in km

change of the network topology [90].

3.1.2 Signal Derivative

The use of the first derivative of the current or voltage signals has been reported since a long time [93]. This kind of filtering is based on a data window of two samples for extracting the abrupt changes of the monitored signal. The first differences of the current samples can be expressed as:

$$\Delta I_n = I_{n+1} - I_n \tag{3.6}$$

where I_n is the n^{th} sample of the signal *I*.

Differentiation is known as a classical ill-posed problem or unstable process; in systems that perform differentiation, small differences in the input signal lead to large differences in the output signal and inadequate accuracy. This sequence filter is the simplest of all filters and uses minimum number of samples. However, its output I' is sensitive to even small changes of the TW signal *I* as depicted in Figure 3.3. The standard approach to such ill-posed problems is to convert them to well-posed problems by smoothing the input data [91]. Alternatively, a three-sample sequence filter, which is based on the second difference of the TW current samples is considered. The second difference filter; with three samples window; can be expressed as

$$\Delta I_n = I_{n+1} - 2I_n + I_{n-1} \tag{3.7}$$

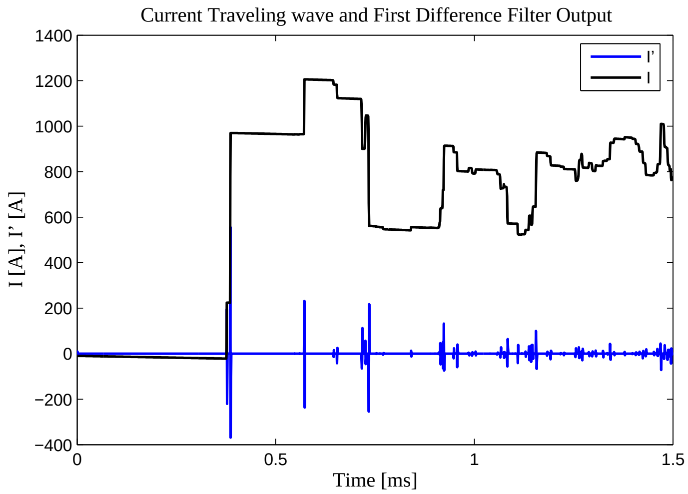

Figure 3.3: Current traveling wave I and first difference filter output I′ [A]

where *n* is the sample number. Thus, a system $y = Hx$ with an impulse response $h(n) = [1/2, 0, -1/2]$ approximates the discrete first derivative. On the other hand, a system $y = Gx$ with an impulse response $g(n)$ = [1, -2, 1] approximates the second derivative. It is noted that the second difference detected abrupt changes in signals and produced a zero response within flat and linearly sloped signal regions. The disadvantage of this filter is that the presence of even a small amount of noise in the signal can lead to wild variations in its derivative at any time instant. Also, the traveling signal is attenuated for a frequency dependent transmission line model and high fault resistance, so the output signal is relatively small as shown in Figure (3.4). These filters can be implemented in the fault locator algorithm and it should have a high

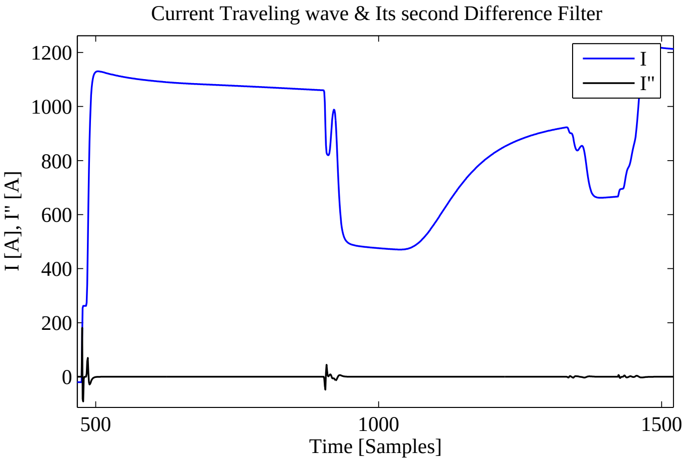

Figure 3.4: Current traveling wave (blue) and its second difference output (black) as a function of time in samples

signal-to-noise ratio (SNR). This means that a better fault locator has a higher response to the edge within a traveling wave signal than to the surrounding noise.

3.2 Frequency Domain Approach

Fourier transform-based fault location algorithms have been proposed since a long time. Most of the proposed algorithms use voltages and currents between fault initiation and fault clearing [92]. To find out the frequency contents of the fault signal, several transformations can be applied, namely, Fourier, wavelet, Wigner, etc., among which the Fourier transform is the most popular and easy to use.

3.2.1 Fourier Transform

Fourier transform (FT) is the most popular transformation that can be applied to traveling wave signals to obtain their frequency components appearing in the fault signal. Usually, the information that cannot be readily seen in the time domain can be seen in the frequency domain. The FT and its inverse give a one-to-one relationship between the time domain *x(t)* and the frequency domain *X(ω)*. Given a signal *I(t)*, the FT *FT(ω)* is defined by the following equation:

$$FT\left(\omega\right)=\int\limits_{-\infty}^{\infty} I(t)\cdot e^{-j\omega t}dt \tag{3.8}$$

where ω is the continuous frequency variable. This transform is very suitable for stationary signal, where every frequency components occur in all time. The discrete form of the FT can be written as

$$DFT\left[k\right]=\frac{1}{N}\sum_{n=1}^{N} I\left[n\right]\cdot e^{-j\frac{2\pi kn}{N}} \tag{3.9}$$

where $1\leqslant k\leqslant N$. The FT gives the frequency information of the signal, but it does not tell us when in time these frequency components exist. The information provided by the integral corresponds to all time instances because the integration is done for all time intervals. It means that no matter where in time the frequency *f* appears, it will affect the result of the integration equally. This is why FT is not suitable for non-stationary signals. The FT has good results in the frequency-domain but very poor results in the time domain [94]. When the current surge hits the fault point, it is reflected with the same sign and travels back to the source end of the line [95]. Then, it is reflected again from the source end with the same sign and returns back to the fault point. Since the duration of this complete cycle is 4τ, (τ is the propagation time of the surge from the source end to the fault point) the main component of the current signal after the circuit beaker opening has a frequency equal to

$$f = \frac{1}{4\,\tau} \tag{3.10}$$

so that the distance to the fault may be obtained as

$$FL = \frac{v}{4\,f} \tag{3.11}$$

3.3 Time-Frequency-Domain Approach

The traveling wave based fault locators utilize high frequency signals, which are filtered from the measured signal. Discrete Fourier Transform (DFT) based spectral analysis is the dominant analytical tool for frequency domain analysis. However, the DFT cannot provide any information of the spectrum changes with respect to time. The DFT assumes the signal is stationary, but the traveling wave signal is always non-stationary. To overcome this deficiency, the Short Time Fourier Transform and the Wavelet Transform allow to represent the signal in both time and frequency domain through time windowing function. The window length determines a constant time and frequency resolution. The nature of the real traveling wave (TW) signals is nonperiodic and transient; such signals cannot easily be analyzed by conventional transforms. So, Short Time Fourier Transform and the Wavelet Transform must be selected to extract the relevant time-amplitude information from a TW signal. In the meantime, the SNR ratio can be improved based on prior knowledge of the signal characteristics.

3.3.1 Short Time Fourier Transform

To overcome the shortcoming of the DFT, short time Fourier transform (STFT, Denis Gabor, 1946) was developed. In the STFT defined below, the signal is divided into small segments which can be assumed to be stationary. The signal is multiplied by a window function within the Fourier integral. If the window length is infinite, it becomes the DFT. In order to obtain the stationarity, the window length must be short enough. Narrower windows afford better time resolution and better stationarity, but at the cost of poorer frequency resolution. One problem with the STFT is that one cannot determine what spectral components exist at what points of time. One can only know the time intervals in which certain band of frequencies exist. The STFT is defined by following equation:

$$STFT(t,\omega) = \int_{-\infty}^{+\infty} I(t) \cdot W(t-\tau) \cdot e^{-j\omega t} dt \tag{3.12}$$

where *I(t)* is the measured signal, ω is frequency, *W(t-*τ*)* is a window function, τ is the translation, and *t* is time.

To separate the negative property of the DFT described above, the signal is to be divided into small enough segments, where these segments (portion) of the signal can be assumed to be stationary. These transforms can be displayed in a three dimensional system (Amplitude of transform, frequency, time). And it is clearly seen in time and frequency domain. To get better information in time or frequency domain, parameters of the window can be changed. As aforementioned, narrow windows give good time resolution, but poor frequency resolution. Wide windows give good frequency resolution, but poor time resolution. Thus, it is required to compromise between the time and frequency resolutions. For example, a function may contain a high peak on an interval while it is small elsewhere. This function could represent a current wave packet, which is just a peak traveling from one point to another in a transmission line. A Fourier series will not do as well when representing this function because the sine and cosine functions, which make up the Fourier series, are all periodic and thus it is hard to focus on the local behavior of this wave packet.

3.3.2 Wavelet Transform

The wavelet multiresolution analysis is a new and powerful method of signal analysis and is well suited to traveling wave signals [96]. Wavelets can provide multiple resolutions in both time and frequency domains. The windowing of wavelet transform is adjusted automatically for low and high-frequencies i.e., it uses short time intervals for high frequency components and long time intervals for low frequency components. Wavelet analysis is based on the decomposition of a signal into ‘scales’ using wavelet analyzing function called ‘mother wavelet’. The temporal analysis is performed with a contracted, high frequency version of the ‘mother wavelet’, while the frequency analysis is performed with a dilated, low frequency version of the ‘mother wavelet’. Wavelets are functions that satisfy the requirements of both time and frequency localization. The necessary and sufficient condition for wavelets is that it must be oscillatory, must decay quickly to zero and must have an average value of zero. In addition, for the discrete wavelet transform considered here, the wavelets are orthogonal to each other. Wavelet has a digitally implementable counterpart called the discrete wavelet transform (DWT). The generated waveforms are analyzed with wavelet multiresolution analysis to extract sub-band information from the simulated transients. Daubechies wavelets are commonly used in the analysis of traveling waves [118]. They were found to be closely matched to the processed signal, which is of utmost importance in wavelet applications. Daubechies wavelets are more localized i.e., compactly supported in time and hence are good for short and fast transient analysis and provide almost perfect reconstruction. However, there are some other wavelets show a good correlation with the transient signals and may be used in the analysis. Several wavelets have been used in this thesis. The comparison is presented in section (3.3.4). Due to the unique feature of providing multiple resolution in both time and frequency by wavelets, the sub-band information can be extracted from the original signal. When applied to faults, these sub-band information are seen to provide useful signatures of transmission line faults, so that the fault location can be done more accurately. By randomly shifting the point of fault on the transmission line, a number of simulations are carried out employing the ATP/EMTP. The generated time domain signals for each case are transferred to the modal domain using Clark’s transformation. Then, the aerial mode signal is analyzed using wavelet transform. From the different decomposed levels, only one level is considered for the analysis. This level has the highest energy level output and the dominant frequency of the transient.

Waveforms associated with the traveling waves are typically non-periodic signals that contain localized high frequency oscillations superimposed on the power frequency and its harmonics. DFT was found to be not adequate for decomposing and detecting these kinds of signals because it does not provide any time information. On the other hand, the STFT takes the time dependency of the signal spectrum into account. However, the time-frequency plane cannot give both accurate time and frequency localizations. The Wavelet transform allows time localization of different frequency components of a given signal like the STFT but its transformation functions called wavelets which adjust their time widths to their frequency in such a way that higher frequency wavelets will be narrow and lower frequency ones will be broader. Wavelet’s time frequency resolution provides a useful tool for decomposing and analyzing fault transient signals.

Given a function *x(t),* its Continuous Wavelet Transform (CWT) is defined as follows:

$$CWT(a,b) = \frac{1}{\sqrt{a}} \int\limits_{-\infty}^{+\infty} x(t)\ \Psi^*(\frac{t-b}{a})\ dt \tag{3.13}$$

The transformed signal is a function with two variables *b* and *a*, the translation and the scale parameter respectively. Ψ*(t)* is the mother wavelet, which is a band-pass filter and Ψ^* is the complex conjugate form . The factor $\frac{1}{\sqrt{a}}$ is used to ensure that each scaled wavelet function has the same energy as the wavelet basis function. It should also satisfy the following admissible condition:

$$\int\limits_{-\infty}^{\infty} \Psi(t)\ dt = 0 \tag{3.14}$$

The term translation refers to the location of the window. As the window is shifted through the signal, time information in the transform domain is obtained. *a* is the scale parameter which is inversely proportional to frequency. High scales give a global information of the signal (that usually spans the entire signal), whereas low scales give a detailed information of a hidden pattern in the signal that usually lasts a relatively short time. In practical applications, low scales (high frequencies) do not last for long, but they usually appear from time to time as short bursts. High scales (low frequencies) usually last for the entire duration of the signal.

Wavelet transform of sampled waveforms can be obtained by implementing the DWT, which is given by:

$$DWT(k,n,m) = \frac{1}{\sqrt{a_0^m}} \sum_n x\,[n]\ \ \Psi(\frac{k - nb_o a_0^m}{a_0^m}) \tag{3.15}$$

where Ψ*(t)* is the mother wavelet, and the scaling and translation parameters *a* and *b* in (3.13) are replaced by a_0^m and $nb_o a_0^m$ respectively, *n* and *m* being integer variables. In the standard DWT, the coefficients are sampled from the CWT on a dyadic grid.

The wavelet coefficients (WTC) of the signal are derived using matrix equations based on decomposition and reconstruction of a discrete signal. Actual implementation of the DWT involves successive pairs of high-pass and low-pass filters at each scaling stage of the DWT. This can be thought of as successive approximations of the same function, each approximation providing the incremental information related to a particular scale (frequency range). The first scale covers a broad frequency range at the high frequency end of the spectrum and the higher scales cover the lower end of the frequency spectrum however with progressively shorter bandwidths. Conversely, the first scale will have the highest time resolution. Higher scales will cover increasingly longer time intervals [116].

3.3.3 Filter Bank

A time-scale representation of a digital signal is obtained using digital filtering techniques. The DWT analyzes the signal at different frequency bands with different resolutions by decomposing the signal into a coarse approximation and detail information. The DWT employs two sets of functions, called scaling functions and wavelet functions, which are associated with a low-pass and high-pass filters. The multi-stage filter bank implement the DWT using the low-pass mother wavelet $H_0(n)$ and its halfband highpass filter dual, $H_1(n)$ [121]. After the filtering, half of the samples can be eliminated according to the Nyquist's rule, since the signal now has a highest frequency of $f/2$ instead of f [122]. The signal therefore can be downsampled by 2, simply by discarding every other sample. The output of the low-pass filter is filtered again in high and low-pass filters until DC value is reached.

This procedure is repeated as shown in Figure (3.5) without the down-sampling block after the high-pass filters. H_0 and H_1 are low-pass and high-pass filters respectively. The outputs of the high-pass filter are the original signal in different scaling. Their sum is the DWT. In this thesis, the analysis is performed at a sampling frequency of 1.25 MHz. For the chosen sampling frequency and three wavelet details levels, the maximum frequency considered is 625 kHz. Down sampling by two at each succeeding level. Frequency range of level 1 is from 625 to 312.5 kHz, that of level 2 is from 312.5 to 156.25 kHz, and is 156.25 to 78.125 kHz for level 3. The frequency range is halved when the level increases. At the lowest level, level 1, the mother wavelet is the most localized in time and damps most rapidly within a short period

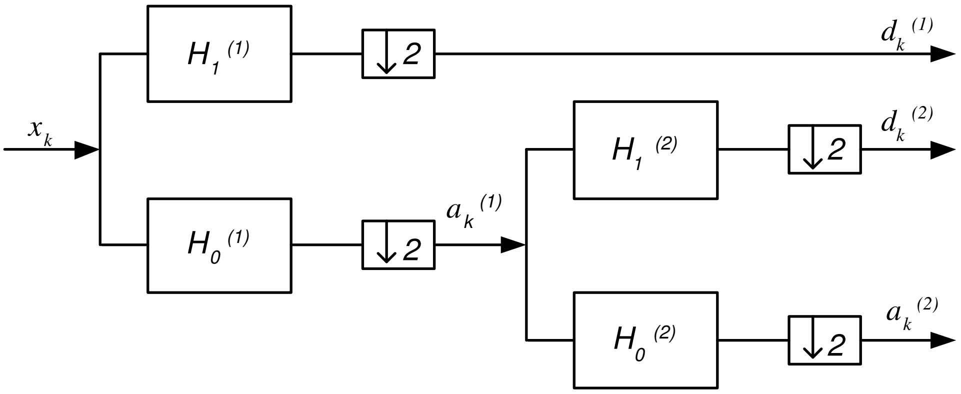

Figure 3.5: Wavelet transform filter bank

of time. As the wavelet goes to higher levels, the analyzed wavelets become less localized in time and damp less because of the dilation nature of wavelet transform analysis.

3.3.4 Mother Wavelet Selection

While, in principle, any admissible wavelet can be used in the wavelet analysis, several wavelets have been tested to extract the best TW signal features using the Wavelet toolbox incorporated into the MATLAB program [119], [120]. The considered mother wavelets for finding the fault locations are Daubechies wavelets, Coiflets, Symlets, and Biorthogonal wavelets [118]. These wavelets are discretely represented in MATLAB. The best mother wavelets have a high correlation with the high frequency traveling wave signals in a typical transmission networks. Smoothness and regularity of the wavelet are the main factors that can be used for testing the mother wavelet [101]. In this section, the difference between the original and the reconstructed signals was the main criterion for selecting the optimum mother wavelet as follows:

$$error = I_1 - \acute{I_1} \tag{3.16}$$

where I_1 the original signal and $\acute{I_1}$ is the reconstructed signal. Then the Euclidean length of the error vector is computed by the norm function incorporated in MATLAB program. An example of the above mentioned mother wavelet comparison is depicted in Figure 3.6 where

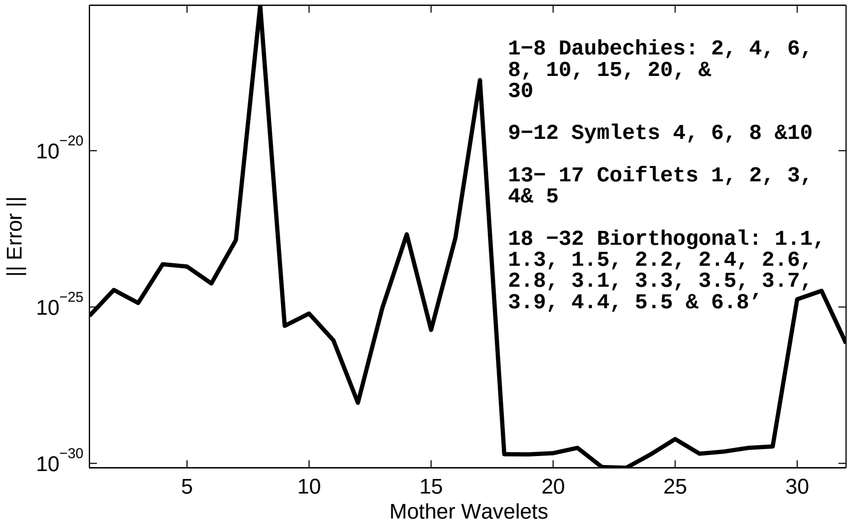

Figure 3.6: Mother wavelet function error analysis

the mother wavelets from 1 to 8 are Daubechies wavelets: db2, db4, db6, db8, db10, db15,

db20, and db30, mother wavelets from 9 to 12 are: Symlets sym4, sym6, sym8, and sym10. Mother wavelets from 13 to 17 are Coiflets coif1, coif2, coif3, coif4 and coif5.
Mother wavelets from 18 to 32 Biorthogonal wavelets: bior1.1, bior1.3, bior1.5, bior2.2, bior2.4, bior2.6, bior2.8, bior3.1, bior3.3, bior3.5, bior3.7, bior3.9, bior4.4, bior5.5 and bior6.8. Biorthogonal wavelets show a good correlation with the fault signal. This is investigation can be performed each time the fault location algorithm is carried out.

3.3.5 Wavelet Details Selection

Wavelet analysis has been used to determine the TWs that arrive at the relaying point as a result of faults and switching operations. This can be achieved through the analysis of details' spectral energy of the current traveling wave signal. The optimum level of wavelet details' coefficients is selected based on its energy content over an window interval of twice of the transmission line travel time and is defined as

$$DE_j = \sum_{k=N-M}^{N} D_j^2(k) \tag{3.17}$$

where $M = 2\ (\frac{TT}{dt})$ is the number of samples of the moving window which depends on the travel time *TT* of the transmission line under investigation, *dt* is the sampling interval, *N* is the number of samples of the recorded signal, D_j is the *j*-th wavelet details coefficients and DE_j is the *j*-th details energy [64], [103], [104].
The same principle is applied for the distinguishing between various transients such as faults, unloaded line switching, and transformer energization. Permanent faults has minimum details energy among other transients as depicted in Figure 3.7. The fault transients have the lowest energy contents compared to the line and transformer energization. For choosing the level for the TW fault transient, the details level that has the highest frequency of all levels is selected using Fourier transform as shown in Figure 3.8. These transients have been produced by ATP/EMTP simulations on a typical 400-kV transmission line as described in the appendix.

3.4 Wavelet Correlation Function

The correlation function can be interpreted as a wavelet transform. The CWT coefficient shown in Equation (3.13) represents how well a signal and a wavelet match. Hence, CWT expresses

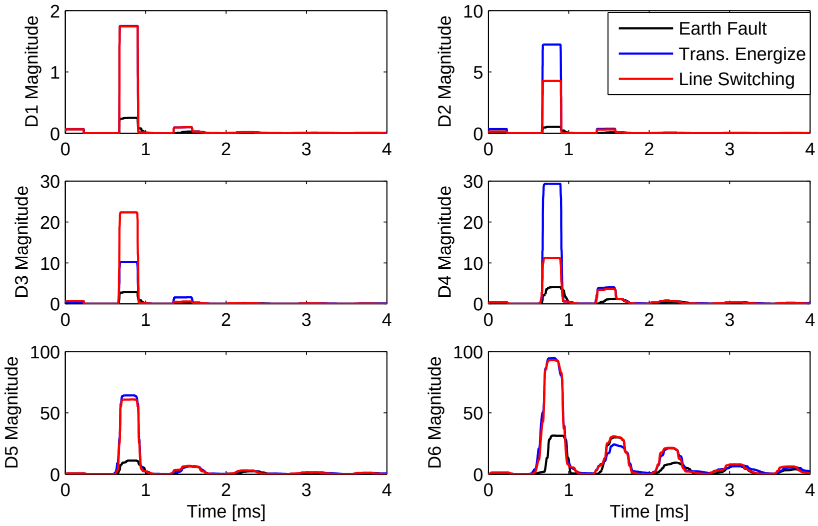

Figure 3.7: Spectral energy of various transients

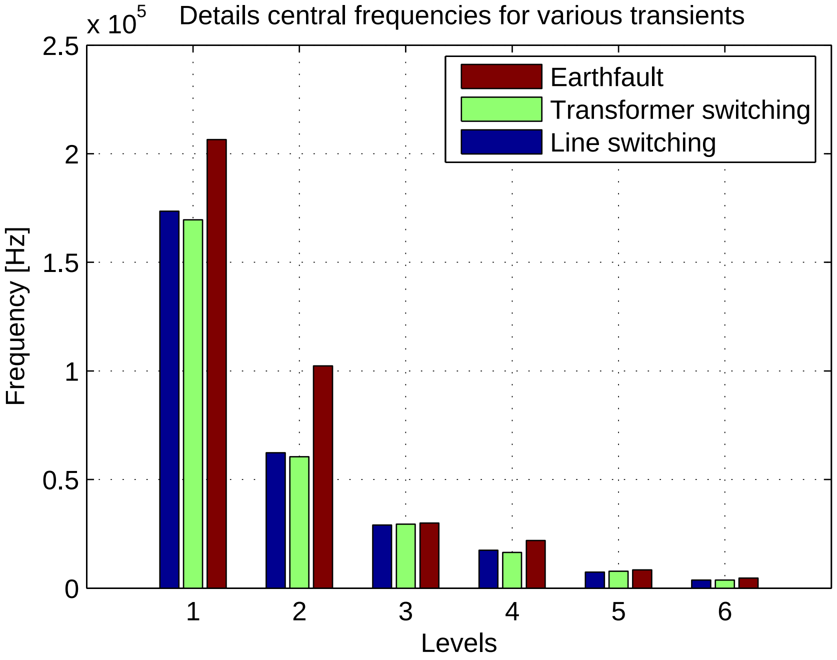

Figure 3.8: Details' level frequency of various transients

the degree of correlation between a wavelet and the signal being investigated. Moreover, the correlation of two signals in the time domain can be replaced by the correlation of their wavelet transforms in the wavelet transform domain [124]. The inner product of two signals f_1 and f_2, in the time domain, can be written as

$$\langle f_1(u), f_2(u) \rangle = \int\limits_{-\infty}^{\infty} f_1(u) f_2(u) du \tag{3.18}$$

The inner product of two functions can be obtained by a two-dimensional integration of the wavelet transforms in the wavelet domain as follows[125]:

$$\langle f_1, f_2 \rangle = \frac{1}{C_g} \int\limits_{-\infty}^{\infty} \frac{1}{a^2} \int\limits_{-\infty}^{\infty} W_\Psi f_1(a, b) W_\Psi f_2(a, b) db\ da \tag{3.19}$$

where *a* is the scale and *b* is the translation of the wavelet transform and C_g is the admissibility constant depending on Ψ. From (3.4) and (3.14); the template signal x_i - $\overline{x}$ can be interpreted as a mother wavelet, because it is compactly supported and has a sum of zero. Therefore, the correlation function can be reformulated as a DWT:

$$R_{f_1 f_2} = \sum_m \sum_n W_\Psi f_1(m, n) W_\Psi f_2(m, (n + \tau)) \tag{3.20}$$

When the wavelet analysis is applied to the current signals, the details' levels can be calculated and the sub-band information of the abrupt changes in the signals are given. Then, the correlation operation can be executed within each level. Therefore, the fault can be located using the period of the wavelet correlation function (WCF) given by (3.20) [125]. By denoting the WCF delay by τ, and the propagation speed by v, the fault distance *x* from the sending end to the fault location is found using (3.5).

3.5 Traveling Wave Speed Estimation

The fault distance estimation is highly sensitive to the TW speed of propagation. Therefore, a thorough analysis is carried out in this section on different methods for calculating the speed of propagation.

For a three-phase fault at the end of a 163-km transmission line, the TW signal is filtered using wavelet analysis. Also, a transfer function feature of the Transient Analysis of Control System (TACS) as a high pass filter in ATP/EMTP simulations with a proportionality constant of 6.4 $\times 10^{-8}$ and a time constant of 0.1 μs to take the effect of current transformers into account. The optimum mother wavelet was calculated as ’bior2.4’ for aerial-mode signals and ’bior2.6’ for ground-mode signals using the method described in subsection (3.3.4). Each details level of the DWT coefficients has different central frequency and speed of propagation. The TW speed has been calculated using three methods at each details level using MATLAB and ATP/EMTP software simulations as follows

1. Thresholding: As the second reflected signal is highly attenuated, the threshold values were taken from 1$\%$ to about 20 $\%$ of the maximum value of the first signal packet. Normally, there will be some values that will give unreasonable propagation speeds (too high or too low values) which can be discarded, and those close to the speed of light should be considered.
2. The maximum of the first two consecutive peaks of the power delay profile of the details signals.
3. The Mean Time Delay (MTD): The wavelet coefficients are squared at each level to get the power delay profile. The first two signal packets are captured using a threshold value and a wavelet sample window . The mean time delay of the details power profile is calculated as

$$\bar{\tau} = \frac{\sum\limits_{k=1}^{N} D(t_k)t_k}{\sum\limits_{k=1}^{N} D(t_k)} \tag{3.21}$$

Generally, the TW speed is calculated using the following formula:

$$Traveling \quad Wave \quad Speed = \frac{2 \times LineLength}{t_2 - t_1} \tag{3.22}$$

where $t_2 - t_1$ is the time difference between two consecutive signals of the details level. The propagation speed, which has been calculated using Line/Cable Constants program (LCC) incorporated in ATP/EMTP, considers the dominant transient frequency at which the transient solution of the traveling wave equation is performed in ATP/EMTP. The physical layout of the transmission line is input to LCC program of ATP/EMTP, i.e. average height above ground, conductor spacing, and resistance. In this example the TW speed was 291774 km/s. The TW speed at three DWT levels has been calculated using the three different methods mentioned above. The first method is performed by taking a staged thresholds from 1 $\%$ to 20 $\%$ of the maximum value of the signal squared. The second one is achieved by calculating the delay at the maximum value of the signal squared. The last method is to estimate the time difference of the TW arrivals using the MTD of the first two consecutive packets of the details signal. The MTD is calculated by capturing the first and second traveling wave packet signals of the power of details' coefficients using thresholding from a very small value (0.001) up to about 0.2 times the maximum value of the first peak of the details signal. Then, the MTD for each packet is calculated. The reason of using these methods is that the mother wavelet is oscillatory and when it arrives at the fault locator, its arrival time is somewhere between the wavelet start and end values for a specified threshold. First, the first and second packets of the square of DWT details' coefficients (WTC^2 is usually called the power delay profile) at each level are estimated. Secondly, the MTD of each packet is calculated using (3.21), and finally, the speed of propagation is calculated using (3.22) . A single-phase to ground fault was simulated at the end of a typical 400-kV transmission line with 112-km length. The propagation speed is automatically calculated and the results are listed in Table 3.1. As depicted in Table 3.1, the propagation speed of the traveling wave has different values at different frequencies [126], where *v(Th)* is the speed of propagation using the delay at a different threshold levels, *v (Max)*

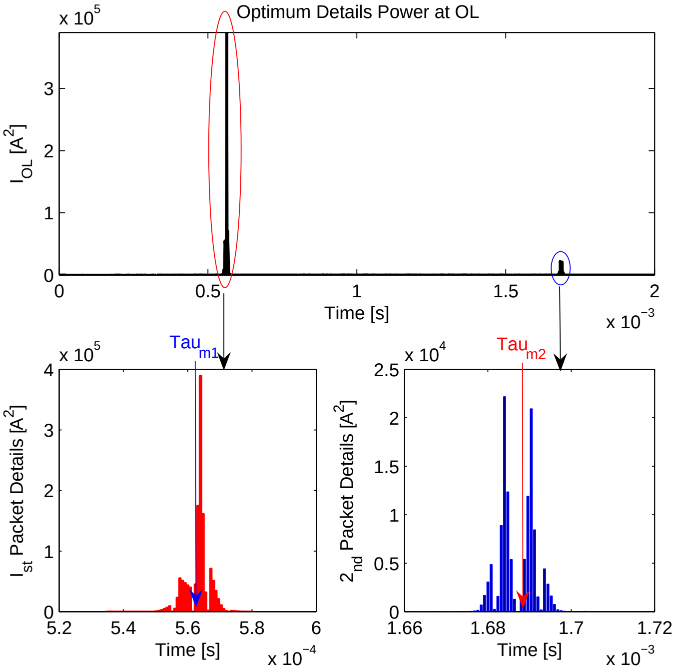

Figure 3.9: Mean delay for details Level power delay profile

Table 3.1: *Propagation speed using: thresholding, maximum power, and mean delay*

Method	HP Filter	level 1	level 2	level 3
v (Th)	289830	290660	289010	290040
v (Max)	289830	290660	291070	288190
v (τ_{Mean})	290101	290660	290313	290437

is the speed of propagation using the delay at the maximum power of the details' coefficients (WTC^2) and *v* (τ_{Mean}) is the speed of propagation using the MTD. Figure 3.10 shows the traveling wave speeds at three frequency bands normalized to the speed of light. The results reveal that the speed can be calculated at different thresholds and has a great effect on the distance fault calculations. At high frequency band (level 1), the propagation speed is constant (about 97.02$\%$ of the speed of light) when using all the aforementioned methods. Thus, at each details level, the fault location can be found using the same propagation speed of the same level.

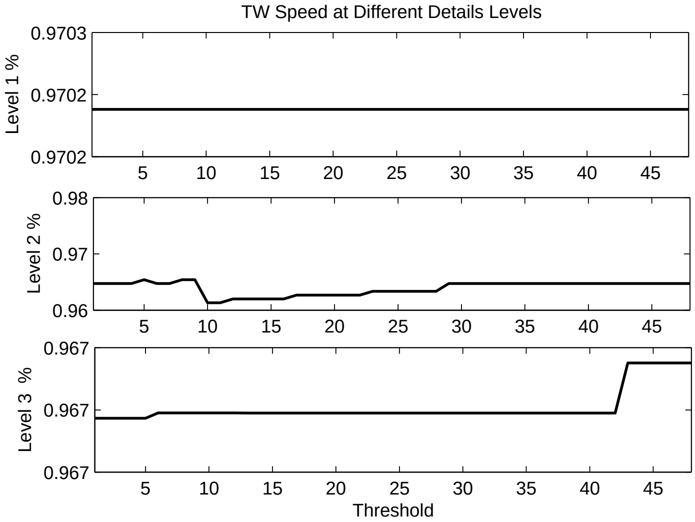

Figure 3.10: Traveling wave speed using thresholding as a percentage of light's speed

3.6 Summary

In this chapter, a review of signal processing methods applied to fault location algorithms based on traveling wave signals was presented. Current traveling waves were used because they can be extracted from the conventional current transformers leading to a cost effective design. Time-based methods were found suitable for pre-processing and filtering. Fourier-based method can give the frequency contents of the traveling wave signal for pre-processing without giving the time information of the fault signal. The simulations show that those methods based on time-frequency analysis can give more accurate estimates for the fault location. The WT is a good tool for analyzing fault signals. To improve the accuracy of the fault location, an optimum mother wavelet is selected based on the minimum error between the original and reconstructed fault signal.

Chapter 4

Current Transformer Modeling

A current transformer (CT) transforms the line current into values suitable for standard protective relays and also isolates the relays from line voltages. The CT has two windings, designated as primary and secondary, which are insulated from each other. There are various types of primary windings arrangements. The secondary is wound on an iron core. The primary winding is connected in series with the circuit carrying the line current to be measured, and the secondary winding is connected to protective devices, instruments, meters, or fault locators. The secondary winding supplies a current in direct proportion and at a fixed relationship to the primary current.

Conventional substation CTs are usually used for monitoring the traveling wave transients, in particular, traveling wave fault location algorithms. However, the accuracy of these algorithms primarily depends on the characteristics of the CTs. One of the main reasons for using the CTs in traveling wave fault locators is their wide range transfer function spectrum. The modeling of the CTs has been a large research-area for several decades for monitoring high frequency current signals [107], [108]. Most of these research efforts studied the CTs in the low and medium frequency ranges. The main objective of this chapter is to investigate the CT high frequency model and its influence on the traveling wave fault location algorithms.

Two main methods of modeling the CTs are developed in this thesis based on two different applications: time domain modeling for nonlinearity at the low frequencies and frequency dependence modeling for high frequencies. The latter is emphasized using transfer functions since traveling waves have a range of several kHz frequencies. The model is correctly represented by linear elements at higher frequencies because most of the flux is a leakage flux.

A detailed representation of the complete CT is not a practical proposition in terms of computation requirements. In general, the secondary of the CT needs to be modeled in detail only, with the rest of the system represented by an appropriate equivalent. However, the use of an equivalent circuit based on the fundamental frequency model is inadequate for transient simulation, because of the presence of other frequency dependent components.

Based on the relationship between the time and frequency domains, an effective frequency-dependent CT model is developed here. In the time domain the system impulse response is convolved with the input excitation. In the frequency domain the convolution becomes a multiplication; if the frequency response is represented correctly, the time domain solution will be accurate.

In this chapter a comprehensive analysis of the current transformer behavior at high frequency ranges is presented. MATLAB programs have been developed to estimate the parameters of the equivalent circuits in low and high frequency ranges. These programs were developed using the equivalent circuit scheme and the system identification toolbox in MATLAB. The secondary windings are located in the CT tank at the bottom of the U-shaped primary winding. The CT measurements are carried out for a 110-kV CT at the high voltage hall of the Department of Electrical Engineering, Helsinki University of Technology. The general purpose CT model cannot be established for different CT structures and different voltage levels. Earlier research works were done in [90] and [109] at transmission level CT and different structures. However, these models did not take into account the detailed parameters of the CT model.

The modeling of the CT can be classified as terminal (or black box) models and detailed (or internal) models. The method used in this thesis is based upon the terminal models using recorded time response from impulse tests. An impulse signal is applied to the CT terminal and the required time responses are recorded using a digitizer. The digital recorded time signals are Fourier transformed to obtain the frequency spectra from which the desired transfer functions are calculated.

4.1 Experimental Measurements

The modeling of the CT is divided into two parts: the low frequency and high frequency models. The low frequency model parameters of the CT are estimated using open and short circuit tests at the power frequency. At low frequency, the stray capacitances have negligible effects. A stable-output power analyzer was used in the measurements. Open circuit tests were only measured from the secondary windings while the short circuits were measured from both the primary and secondary sides. Since the inductance and resistance of the secondary windings dominate the impedance at a low frequency, the parameters can be easily calculated using open and short circuit tests at the power frequency. The CT used in this measurement was a 110-kV, 200/5 hair-pin type, with three secondary windings as shown in Figure 4.1. The CT has also a capacitive layer, which may be used for voltage monitoring. The nameplate data are listed in Appendix B. There are several methods to measure the transfer function of a CT model. For high frequency modeling, open and short circuit impulse tests were carried out. The primary winding was fed from an impulse current signal measured using a wide-band current transformer (Pearson transducer) and the output current on each secondary winding was measured using a calibrated resistance R_{sh} equals to 0.4905 Ω. The monitored signals were recorded by an 8-bit, 150-MHz digital oscilloscope controlled by a computer, which saves the data in an ASCII format. The test setup is shown in Figure 4.2. Such a high frequency model is complicated for a CT representation. On the other hand, a black-box model of the input-output representation is easier as it does not need a detailed representation of the CT components. Before the transfer function calculations are carried out, moving average filtering is applied. This is important to remove the noise in the signals of the test records. The primary current

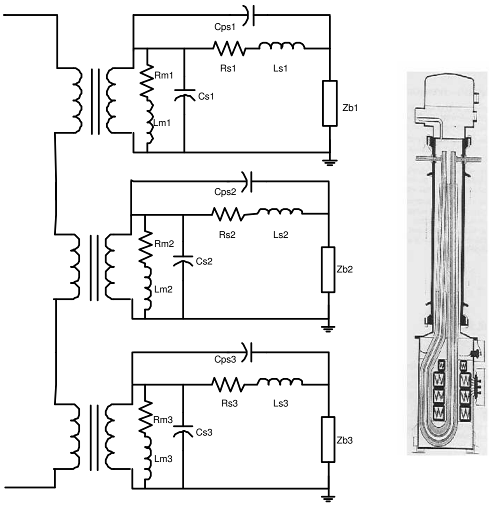

Figure 4.1: CT high frequency equivalent circuit and its cross sectional view

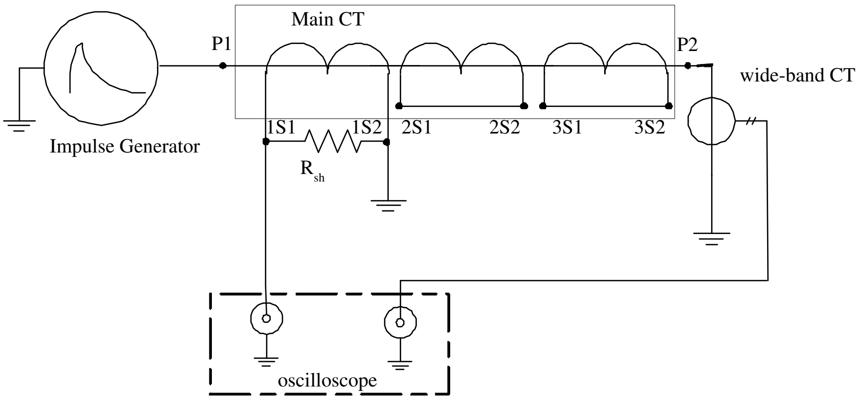

Figure 4.2: CT transfer function test circuit

was measured using Pearson transducer with an output of 0.1 V/A. The transfer function was calculated using the DFT of the input and output current signals. The transfer function was plotted as a function of the frequency and the resonance frequency values for the CT was located and recorded.

4.2 Low Frequency Model

The conventional CT model was adopted for low frequency modeling neglecting the stray capacitances. The open circuit test determines the equivalent core loss resistance and the magnetizing reactance. The short-circuit test determines the winding equivalent resistances and the leakage reactances. Using a stable-output power analyzer, the values of L_s and R_s of the CT equivalent circuit in Figure 4.1 are obtained by measuring the inductance and resistance of the primary winding with the secondary winding being short circuited. The same procedure has been carried out from the secondary windings number 1, 2, and 3, where the primary was short circuited. When the secondary winding was short circuited, the existence of L_m and R_m can be ignored. Since the impedance Z_m is high, the series elements R_s and L_s can be ignored when the open-circuit test was carried out from the secondary winding's side. Since the secondary windings have separate iron cores, the magnetizing branch parameters for each core can be directly calculated. As aforementioned, the short circuit tests were performed from the primary and secondary windings [13] . The measured quantities are as follows:

$$Z_{scp} = Z_p + \frac{Z_{s1}Z_{s2}Z_{s3}}{Z_{s1}Z_{s2} + Z_{s2}Z_{s3} + Z_{s1}Z_{s3}} \tag{4.1}$$

$$Z_{scs1} = Z_{s1} + \frac{Z_p Z_{s2} Z_{s3}}{Z_p Z_{s2} + Z_{s2} Z_{s3} + Z_p Z_{s3}} \tag{4.2}$$

$$Z_{scs2} = Z_{s2} + \frac{Z_{s1} Z_p Z_{s3}}{Z_{s1} Z_p + Z_p Z_{s3} + Z_{s1} Z_{s3}} \tag{4.3}$$

$$Z_{scs3} = Z_{s3} + \frac{Z_{s1} Z_{s2} Z_p}{Z_{s1} Z_{s2} + Z_{s2} Z_p + Z_{s1} Z_p} \tag{4.4}$$

where Z_{scp}, Z_{scs1}, Z_{scs2}, and Z_{scs3} are the measured short circuit impedances from the primary winding, secondary windings s1, s2 and s3 respectively. The impedances Z_p, Z_{s1}, Z_{s2}, and Z_{s3} are the leakage impedances of the primary winding, secondary windings s1, s2 and s3 respectively. Figure 4.2 shows the short-circuit test from the primary, which Z_{scp} can be calculated from. The same procedure is carried out for the other windings to obtain a four measured quantities Z_{scp}, Z_{scs1}, Z_{scs2}, and Z_{scs3}. Equations (4.1) to (4.4) can be solved iteratively using simple numerical methods such as the Gauss-Seidel method. The result is shown in Figure 4.3 in which a stable solution was achieved after 5 iterations. The results are summarized in Tables I and II of Appendix B. In the open-circuit test, the magnetizing impedances were

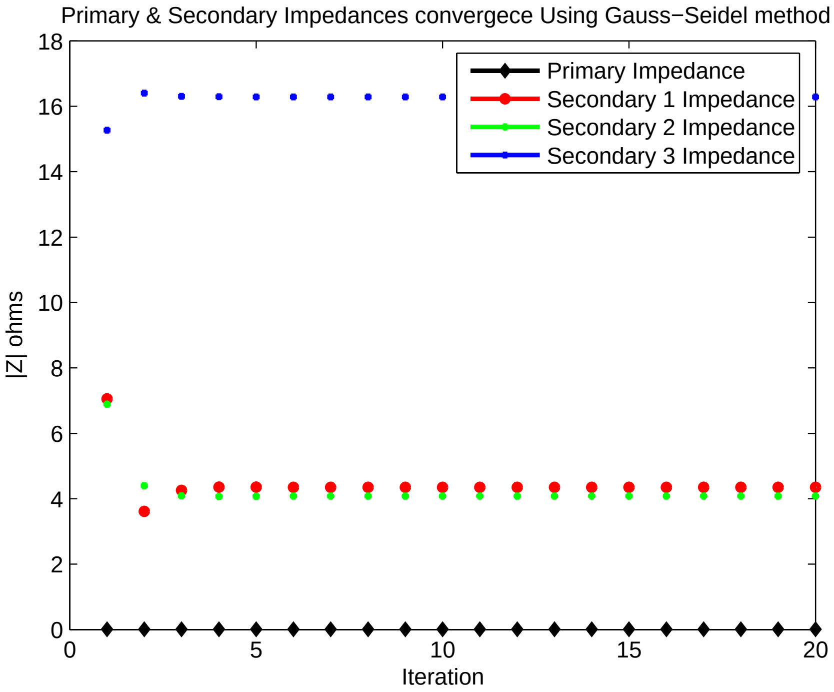

Figure 4.3: CT primary and secondary impedances short circuit test results.

measured for each secondary side because there are three secondary windings with separate magnetic cores. A core is utilized for measuring purposes and the other two cores are utilized for protective relaying purposes. The power frequency voltage was applied to the secondary windings separately and the impedance at their terminals was measured while the primary was open. The magnetization impedance Z_{m1} can hence be calculated using open circuit tests and the results are illustrated in Tables IV and V of Appendix B.

$$Z_{m1} = R_{ms1} + jX_{ms1} \tag{4.5}$$

where $Q_{os1} = \sqrt{(I_{os} \times V_{os1})^2 - P_{os1}^2}$, $R_{ms1} = V_{os1}^2/P_{os1}$, $X_{ms1} = V_{os1}^2/Q_{os1}$. R_{ms1} and X_{ms1} are the secondary winding 1 magnetizing resistance and reactance. The same procedure can be applied to the secondary windings 2 and 3. At power frequency, the primary current should be corrected according to the following correction factors according to the secondary winding being considered [13]

$$I_p = CFs_n \times I_s \tag{4.6}$$

where: *n*= 1, 2, or 3 and

$$CFs_1 = 1 + \frac{z_{s1}}{z_{m1}} \tag{4.7}$$

$$CFs_2 = 1 + \frac{z_{s2}}{z_{m2}} \tag{4.8}$$

$$CFs_3 = 1 + \frac{z_{s3}}{z_{m3}} \tag{4.9}$$

The magnetization characteristic is inserted in the L_m branch considering low frequency transients. However, the magnetization branch has a negligible effect at high frequency traveling wave transients as the flux ceases to penetrate the magnetic core of the CT.

4.3 High Frequency Model

At higher frequencies winding shunt capacitances representing the capacities of the CT windings can no longer be ignored. The capacitance is distributed around the secondary winding. The capacitance of the primary winding is very small when referred to the secondary. Consequently it has been omitted from the model. For simplicity, a lumped parameter model is considered . The capacitance of the secondary winding in parallel to the magnetizing branch was considered because it has a large effect on the CT output at higher frequencies. The equivalent circuit of Figure 4.1 includes secondary winding capacitances and primary to secondary capacitances. C_{sn} represent the capacities of the n^{th} secondary windings, C_{psn} represent the primary to n^{th} secondary windings, R_{sn} and X_{sn} are resistance and reactance of the i^{th} secondary winding, (*n* =1, 2 and 3). Z_{bn} is the n^{th} secondary burden. The inter-winding capacitance due to the coupling between the primary and secondary windings are approximately measured by short circuiting both the primary and secondary windings and using frequency response from the impulse test to calculate the inter-winding capacitances [110], [111], [112]. The results of an impulse test of the inter-winding capacitances are shown in Figure I8 and Figure I9 of Appendix B. The curves show negative values in some cases because of the interaction between the secondary winding near their terminals. This may effect the calculation of the CT transfer function and may give different transfer functions according to the experimental setup. Therefore, it is recommended to perform several tests in different arrangements of the experimental setup to cancel these effects.

Leakage inductance and winding capacitance are distributed components, but they are represented by equivalent lumped components. To model the CT at higher frequencies, open-circuit tests were conducted from the secondary windings while the short-circuit tests were performed from both the primary and secondary windings using impulse signals [113]. The measurements produce some resonance frequencies at which the secondary and primary impedances resonate. It is justified to only consider the equivalent capacitance of the secondary winding in the equivalent circuit of the CT, neglecting that of the primary winding. A small number of primary turns makes capacitance coupling between the primary turns negligible. In other words, the capacitance currents, which are flowing between adjacent turns of the primary, form an extremely small part of the primary current. Shunt capacitances C_{s1}, C_{s2} and C_{s3} represent the capacities of the secondary windings s1, s2, and s3, respectively as shown in Figure 4.1.

The test setup of the capacitance of the primary to secondary-winding s1 is shown in Figure 4.4. The same procedure is followed for measuring the other inter-winding capacitances. As for calculating the distributed capacitances of the windings, which affect the performance at high frequencies, an approximate representation is possible, enabling the calculation of the first resonance frequency. This consists of representing the overall capacitance effect by means of a single equivalent parasitic capacitance *C*, placed immediately after the CT. In order to limit the value of the parasitic capacitance, a suitable arrangement of the winding is achieved by employing many alternating and superimposed layers. The secondary winding capacitances

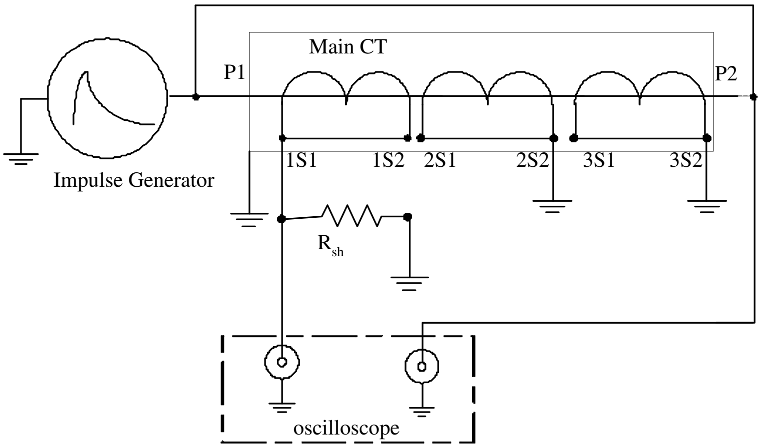

Figure 4.4: CT primary to secondary winding 1 capacitance test

C_{s1}, C_{s2} and C_{s3} can be calculated from the first resonance point from the relation

$$\omega_0 = \frac{1}{\sqrt{Ls \times Cs}} \tag{4.10}$$

The CT performance is valid up to this point beyond which the transformation error rises rapidly.

4.4 Transfer Function

The transfer functions of the CT are defined as frequency dependencies of the ratios of respective currents and voltages on the CT terminals referred to the supply currents.

The frequency response measurements were conducted using standard 1.2/50 μs low impulse voltage signals for open-circuit tests and non-standard 2.2/6 μs current signals for short-circuit test. The first resonance frequency is found for each secondary winding from its corresponding spectrum. Then, the secondary winding shunt capacitances C_{s1}, C_{s2} and C_{s3} can be calculated. Consequently, based on these tests, the frequency dependent correction factors can be obtained using the calculated parameters of the CT as shown in Appendix B

$$CFs_n = 1 + \frac{Zs_n}{Zm_n} + \frac{Zs_n}{Zc_n} \tag{4.11}$$

where Zcn is the capacitive impedance, Zm_n is the magnetizing impedance, Zs_n is the leakage impedance of the n^{th} secondary winding, (*n* = 1, 2 and 3).

The capacitance can be calculated using the inductive reactance calculated from the open and short-circuit measurements discussed in Section 4.2. From (4.10), the secondary winding capacitances at the first resonance frequency were calculated as depicted in Table VI of Appendix B. The transfer function $H(\omega)$ has been determined by the quotient of the Fourier-transformed input signal $X(\omega)$ and its response signal $Y(\omega)$ as [108]

$$H(\omega) = \frac{Y(\omega)}{X(\omega)} \tag{4.12}$$

The CT is modeled as a two-port linear network with constant parameters. The input/output characteristic is defined by

$$I_2(\omega) = [H(\omega) + B(\omega)Z_b(\omega)]I_1 \tag{4.13}$$

where Z_b is the secondary burden impedance of the CT. In practice the burden impedance is low so that the term $B(\omega)$ Zb (ω) is negligible [108]. The function $H(\omega)$ represents the frequency response or the transfer function of the CT. The CT was tested with a non-standard lightning impulse current signal with a small resistive burden for simplification. The test technique consists of applying a signal to the input of the transformer and recording both input and output signals. The analysis of the experimental captured data permitted the derivation of the CT transfer function.

Some practical problems arise when applied to transmission level CTs where high currents should be applied in addition to the noise generated by the high voltage sources [109]. The measurement instruments add some distortions to the waveform to be measured. The system identification toolbox of MATLAB R14 was used to find a state space CT model using different identification models of the identification toolbox (e.g prediction error and Box-Jenkins models) [114]. The measured and estimated model output is depicted in Figure 4.5. The secondary to ground capacitance is effectively reduced by grounding procedure of the CT secondary circuit. The combined effect of the secondary winding capacitance and the primary to shield capacitance is pronounced at 35 kHz, 33 kHz, and 48 kHz for secondary windings s1, s2 and s3 respectively. Hence, the CT is capable of capturing high frequency traveling wave signals up to these frequencies.

Split-core inductive couplers are connected directly to the secondary of the CTs for removing DC decaying signals. They are also tested and their transfer function calculated using the system identification tool box of MATLAB [114]. Different identification models have been

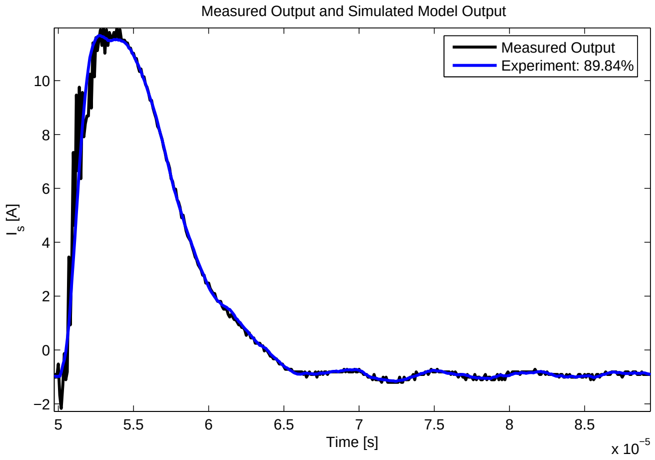

Figure 4.5: A CT secondary measured and simulated output current.

investigated and compared. The Box-Jenkins model gives accurate results as shown in Figure (4.6). From the impulse current measurements, the overall transfer function was plotted aa a

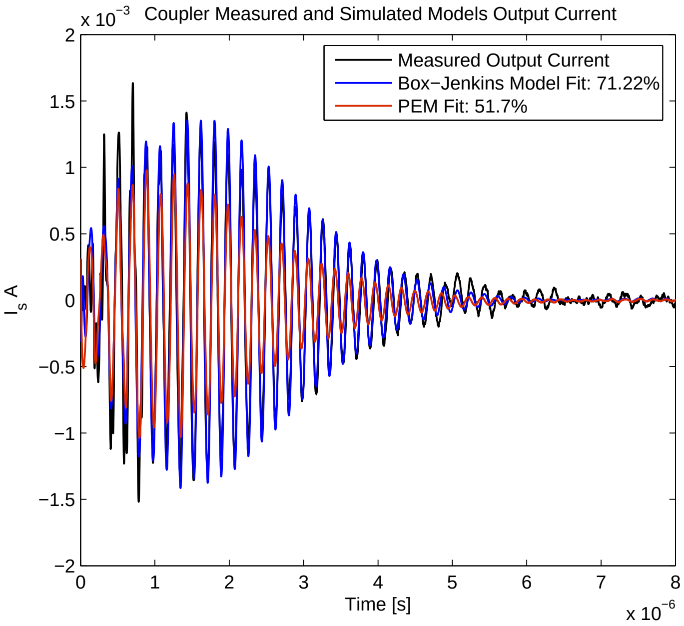

Figure 4.6: Inductive coupler model comparison

function of the frequency. Therefore, the resonance frequency values for the CT, wiring and coupler was located and recorded [115]. The overall transfer function bode plot of both the main CT and the inductive couplers is shown in Figure 4.7. Considering the bilateral interaction between the ATP/EMTP simulated network and TACS field, the transfer function of the measuring system of the CT, secondary wiring and split-core inductive couplers are inserted in the ATP/EMTP model of a 110-kV network model in addition to the secondary wiring cable

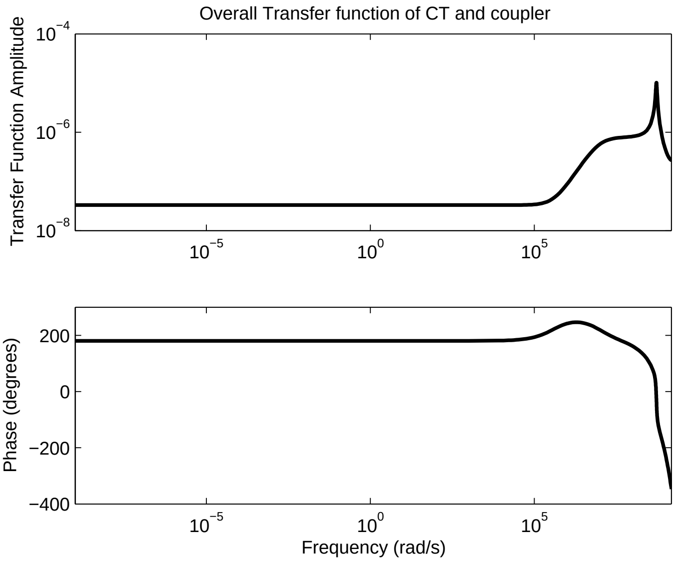

Figure 4.7: Overall transfer function of both the CT and the inductive coupler

from the CT to the TWR as shown in Figure 4.8.

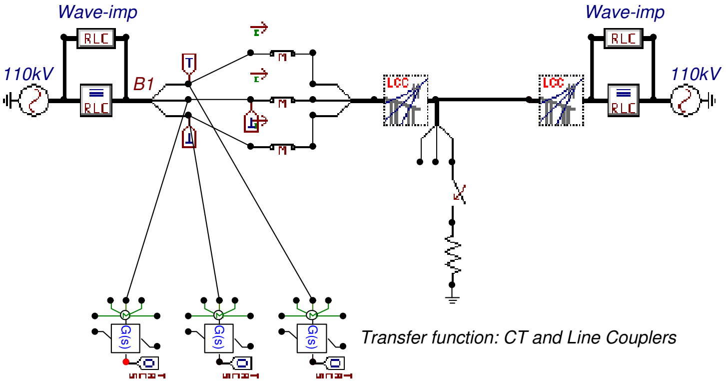

Figure 4.8: Simulated 110-kV transmission line with the transfer function of the CT and the secondary wiring

4.5 Summary

The secondary winding capacitance has the most dominant effect on the CT behavior at high frequencies and the capacitance of the primary winding becomes mall when referred to the secondary side. Consequently, capacitance of the primary winding is assumed to be negligible. However, different high frequency models can be derived depending on the CT structure and the frequency range of interest. The secondary wirings of the test setup have an influence on the capacitance measurements, depending on the the cable length and characteristic. The effect of the secondary cables and other connected transducers to the CT secondary windings reduces the frequency range of the CT. It is recommended to use short secondary wiring cables and a few burdens on the CT secondary winding. The traveling wave can be directly detected from the CT without extra inductive couplers. The measurement results show that CTs can be used for monitoring high frequency current signals over a range up to 200 kHzs which is suitable for traveling wave based fault locators.

Chapter 5

Fault Location Using Single-end Method

5.1 ATP/EMTP Transmission Line Model

The electrical characteristics of a transmission line depend primarily on the construction of the line. The values of inductance and capacitance depend on the various physical factors. For example, the type of line, the tower geometry, and the length of the line must be considered. The effects of the inductive and capacitive reactances of the line depend on the frequency applied. In this chapter, each line span has been simulated with two cases: one with the distributed constant parameter model and the other with the Jmarti frequency-dependent model [71]. The frequency dependent model of Jmarti approximates the characteristic admittance and the propagation constant by rational functions. One of the limitations is that it uses a constant transformation matrix (T_i) to convert from mode domain to phase domain. However, for overhead lines T_i is not as important as it is for cables. The frequency dependence of the series impedance is most pronounced in the ground mode, thus making frequency-dependent line models more important for earth fault current and voltage transients. The simulation of the power system has been carried out by the ATP/EMTP using the ATPDraw preprocessor [70]. The overhead transmission line used in this work is based on a single circuit of the typical 400-kV three bundle-conductor, horizontal-construction line currently used on the Finnish transmission system. The average earth resistivity in the Finnish power system is 2300 Ω.m and the power system frequency of 50 Hz was used. The typical power system model and transmission line configuration chosen for the analysis are shown in Appendix A. The ATP/EMTP simulation is made using a sampling frequency of 1.25 MHz, which is the same sampling frequency of the installed traveling wave recorders (TWR) and it is high enough to capture the TW signals. The other transmission lines connected to bus A and B of Figure 5.1 are simulated using their surge impedances.

The recorded current signals considered for the analysis are generated by simulating the system on the ATP/EMTP program using the model shown in Figure (5.2). The chosen tower configuration for the modeled lines yields a propagation speed of 294115 km/s for the aerial mode and 234451 km/s for the ground mode. The transformation matrix is then calculated at 5 kHz. One of the main disadvantages of the ATP/EMTP program is its rough approximation of the current transformation matrix T_i at one frequency around the traveling wave dominant frequency of the transmission line. However, a detailed analysis of the frequency dependence of the traveling wave speed has been investigated.

The ground current distribution is not uniform. Therefore, it is necessary to know the distribution of the ground currents in order to calculate the impedance of the transmission line conductors with ground return. This problem has been analyzed by [82] and [83]. The use of Carson's series is not suitable for frequency-dependent lines, as it converges slowly at high frequencies. The number of terms required to obtain accurate results increases rapidly with frequency, thus complicating the fitting. Instead, the complex depth of penetration is used. When earth wires are continuous and grounded at each tower, ATP/EMTP assumes, for frequencies below 250-kHz, the earth wire potential to be zero along its length to allow for impedance matrix reduction.

Using the parameters of the described 400-kV line configuration in Figure 5.2, a MATLAB program was developed to calculate the frequency dependence of the transmission line impedance with ground return using the complex depth of ground return [89]. The aerial mode speed was found to be 2.9979×10^5 km/s, while the ground mode is frequency-dependent. Carson's approximate formula has been used in the calculation up to 500-kHz which is sufficient for traveling wave transient calculations [1], [111]. The ground mode impedance of the transmission line with ground return is in the form

$$Z_o = 3 \times (Z_{aa} - \frac{Z_{ag}^2}{Z_{gg}})\Omega/km \tag{5.1}$$

where

$$Z_{aa} = \frac{R_a}{3} + \frac{\omega\mu_o}{8} + j\frac{\omega\mu_o}{2\pi}ln\frac{D_e}{D_{aa}}\Omega/km \tag{5.2}$$

and D_e is the depth of the equivalent ground conductor which can be calculated using $D_e = 658.255\sqrt{\frac{\varrho}{f}}$, Z_{aa} is the self-impedance of the phase conductor with earth return, R_a is the resistance of one of the three conductors, and D_{aa} is the self geometric mean radius GMR_a of line conductors group. The angular frequency is $\omega = 2\pi f$ where f is the frequency and μ_o is the permeability of free space (μ_o=$4\pi \times 10^{-7}$). The self-impedance of the ground conductor with earth return is computed as

$$Z_{gg} = \frac{R_g}{2} + \frac{\omega\mu_o}{8} + j\frac{\omega\mu_o}{2\pi} ln\frac{D_e}{D_{gg}} \Omega/km \tag{5.3}$$

where R_a is the resistance of one of the two conductors and D_{gg} is the self GMR_g of the ground conductors group.

The mutual-impedance of the line conductor group and the ground conductor group with earth return is in the form

$$Z_{ag} = \frac{\omega\mu_o}{8} + j\frac{\omega\mu_o}{2\pi} ln\frac{D_e}{D_{ag}} \Omega/km \tag{5.4}$$

where D_{ag} is the self geometric mean distance GMD_{ag} between the line conductor group and the ground conductor group. The percentage of ground mode currents flowing into the ground wires are calculated using the following equation [89], [84], [79]

$$-\frac{I_{gw}}{3I_o} = \frac{Z_{ag}}{Z_{gg}} \times 100 \tag{5.5}$$

The results are shown in Figure 5.3 in which the ground current speed increases as the ground resistivity decreases. During earth faults, with no ground wires, all the currents flow through the earth. However, the analysis reveals that at high frequencies and high ground resistivity (as the situation in Finland), a large part of the high frequency current signal will propagate in the ground wires. This is depicted in Figure 5.4 in which the percentage of the earth fault current flowing into the earth is plotted from 50-Hz to 250-kHz. Furthermore, Figure 5.5 shows the percentage of the current flowing in the ground wires at the same frequency range. Both figures which are plotted for ground resistivities of 0.1, 1, 10 and 100 k Ω.m. using Carson's approximate formulas [84]. The ground wire current increases as the ground resistivity increases. For high frequency ranges, nonuniform ground resistivity and other frequency dependent parameters should be included [86], [87].

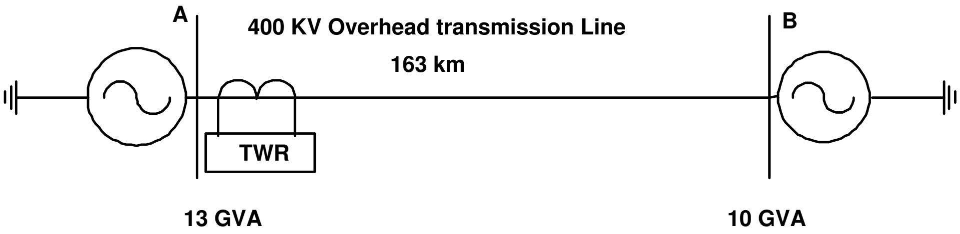

Figure 5.1: A typical power system model

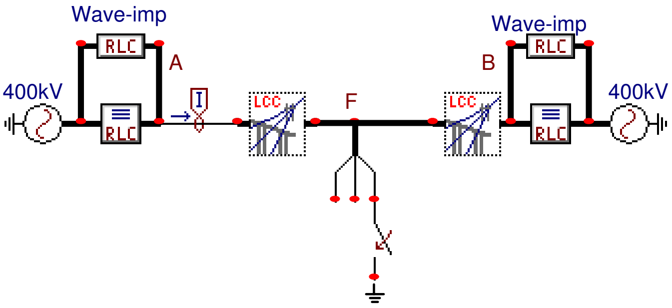

Figure 5.2: ATPdraw circuit of the simulated power system

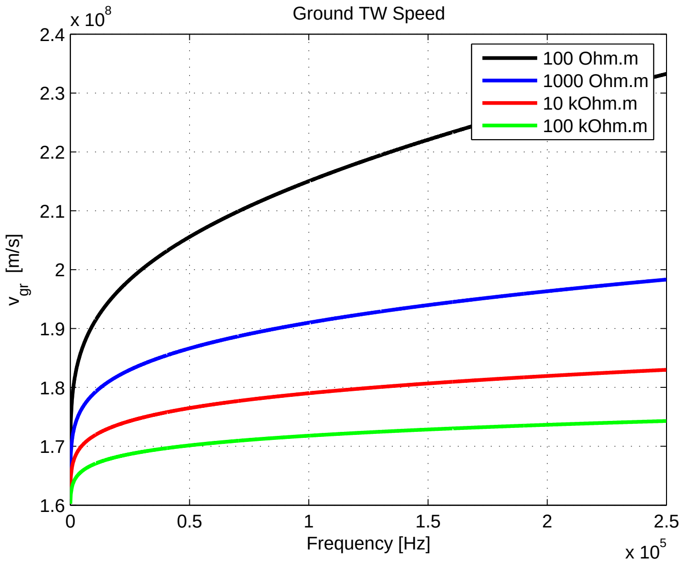

Figure 5.3: TW ground current signal speed for a 400-kV line

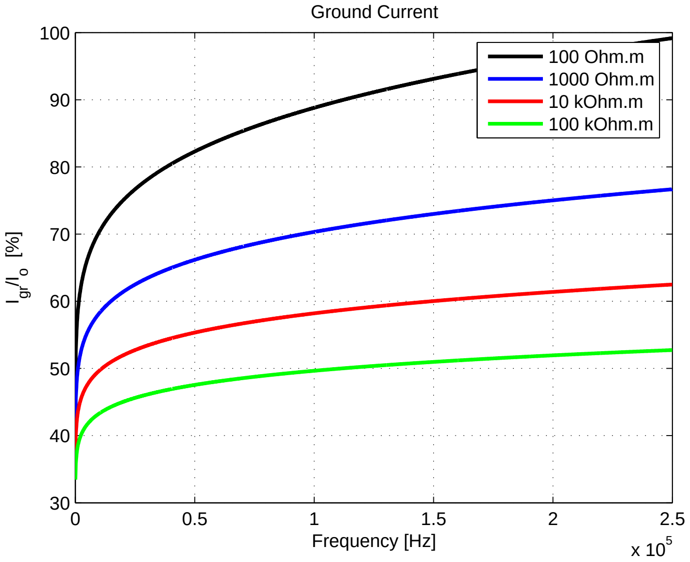

Figure 5.4: Percentage of TW ground current signals for a shielded 400-kV line

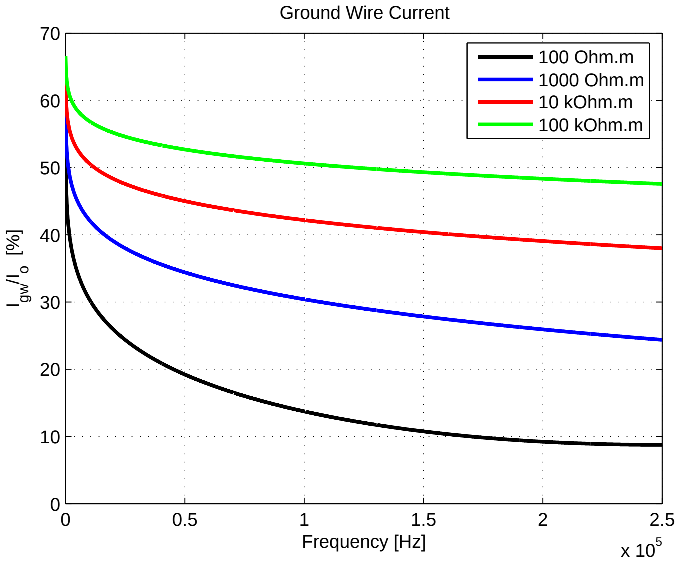

Figure 5.5: Percentage of the TW ground wire current signals for a shielded 400-kV line

5.2 Modal Components Time Delay

In [116], a method for distinguishing between close-in and far-end faults was presented for the voltage TW signals using the time delay between the aerial and ground modes. This phenomenon is discussed in a numerical example. However, this method can only be applied to overhead lines without ground wires and/or counterpoises, because the only path of the ground currents is through earth.

5.2.1 Numerical Example

For a TWR locator located at bus A, a sampling time of 0.8 μsec is used for all simulations and all lines are modeled with frequency dependent parameters. The horizontal tower configuration for the modeled lines yields modal propagation speeds of 294115 km/s for the aerial mode and 234451 km/s for the ground mode. The system is simulated at different locations along the line with a small fault resistance value. Examples for three-phase faults and single-phase to ground faults are presented. The Wavelet Transform Coefficients (WTC) are squared in order to obtain the maximum power of the signal. The maximum value of the signal power delay profile is used to calculate the time differences. As the current signal was acquired at a sampling rate of 1.25-MHz and the WT was used to extract the traveling waves, frequencies up to 625-kHz were considered which is enough for the TW transient frequency. Examples for three-phase faults and single-phase to ground faults are presented. The maximum accuracy obtained using the above mentioned sampling frequency depends on the TW speed and can be calculated as

$$x = \pm\tfrac{v\,Ts}{2} = \pm\tfrac{294115\times0.8\times10^{-6}}{2} = \pm118\text{ m} \tag{5.6}$$

Consider two faults at F$_1$ and F$_2$, for the power system shown in Figure 5.1 at close-in and remote-end distances respectively from bus A. For the close-in fault F$_1$, the lattice diagram of traveling current signals is shown in Figure (5.6) and for a remote-end fault F$_2$, the lattice diagram of traveling current signals is shown in Figure 5.7. For a close-in fault at point F$_1$, the fault locator TWR will record dt_{F1} as the time delay between the two consecutive transient wavefronts. It is easy to see that an identical time delay is likely to be recorded as dt_{F2} for a remote-end fault at point F_2. Thus, the traveling wave fault locator can work incorrectly unless an additional discriminant is available. Such a discriminant is provided by the DWT details of the aerial and ground modal components of the first arriving signals at t_{F1} and t_{F2}. The

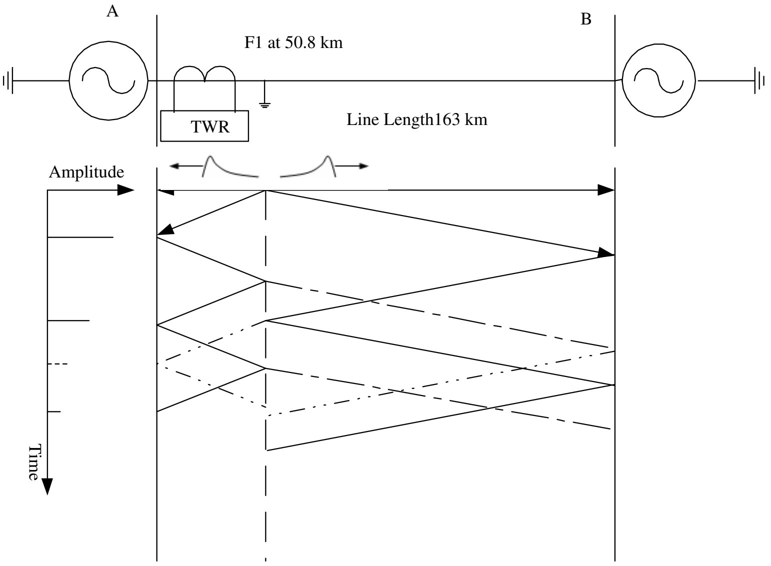

Figure 5.6: Close-in fault applied to the power system model

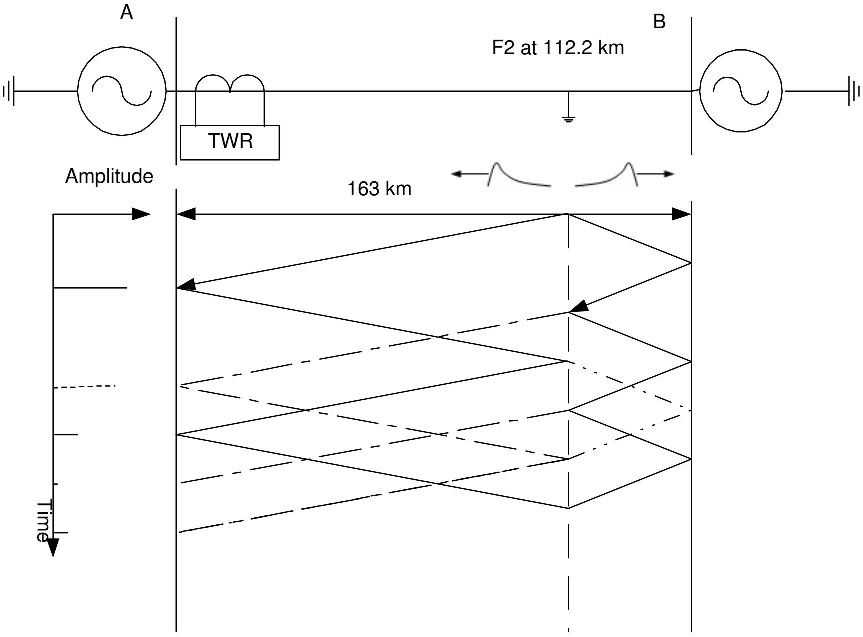

Figure 5.7: Remote end fault applied to the power system model

main idea is to utilize the time delay between the aerial and ground modal components of the incoming three-phase current signal to determine the region where the fault is located. Once the approximate region is determined, then the exact location of the fault will be calculated based on the DWT of the aerial mode (mode 1) signal.

- **Close-in Faults**

  - Three-phase faults: Figure 5.8 shows a three-phase fault aerial mode current signals for a three-phase fault at 50.8-km from bus A. The WTCs of the ground mode are found to be insignificant, hence this type of fault is classified as a short-circuit (ungrounded). Therefore, based on (5.7), the fault location can be calculated using the time difference between the first two peak values of WTCs at level 1, as follows:

$$x = \frac{v\ dt}{2} \tag{5.7}$$

$$x = \frac{294115 \times (651 - 220) \times 0.8 \times 10^{-6}}{2} = 50.705\ km. \tag{5.8}$$

In the case of three-phase faults, the fault location can be found directly since there are

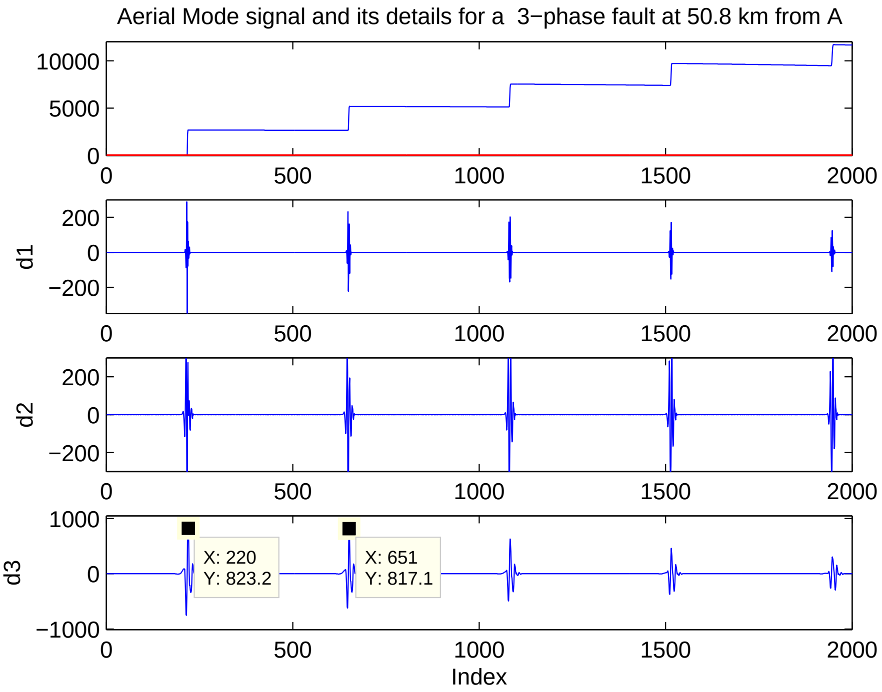

Figure 5.8: Three-phase fault aerial mode current signals for a three-phase fault at 50.8 km from A: the horizontal axis is the time in samples and the vertical axis is the signal magnitude in Amperes

no reflections from the remote-end bus.

- Single-phase faults: Figure 5.9 shows the detailed signal for a single-phase to ground fault located at 50.8-km from A. The first details signal obtained for aerial and ground modes are calculated at their DWT optimum details' level. The algorithm classifies the fault as grounded because the WTCs of the ground mode are significant. The time difference between these two signals is 0.0448-ms which is less than the time difference (0.0672-ms) produced by a fault located at the middle of the line. Hence, the fault is in the first half of the line respect to bus A (close-in fault). Now the fault location can be calculated from the optimum level which is at level 1 in this case [123]. Figure 5.10 shows that the second spike reflected from the fault position was at sample 651. Hence, the fault location can be calculated as: $x = \frac{294115 \times (651-219) \times 0.8 \times 10^{-6}}{2} = 50.823$ km.

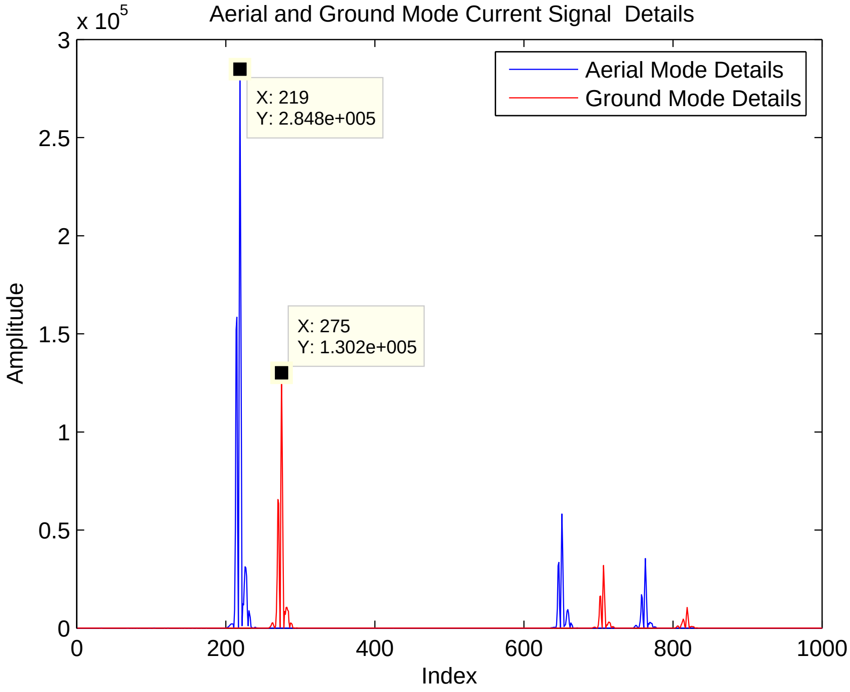

Figure 5.9: Aerial and ground mode details for a single-phase fault at 50.8-km from A: the horizontal axis is the time in samples and the vertical axis is the signal magnitude in Amperes.

- **Remote-end Faults**

- Three-phase faults: Figure 5.11 shows the detailed signal for a three-phase to ground fault located at 112.2-km from bus A. The algorithm classifies the fault as ungrounded since the WTCs of the ground mode are zeros. Hence, the fault distance *x* can be calculated using (5.7) as follows: $x = \frac{294115 \times (1427-479) \times 0.8 \times 10^{-6}}{2} = 111.2358$ km. The error is about 672 meters.

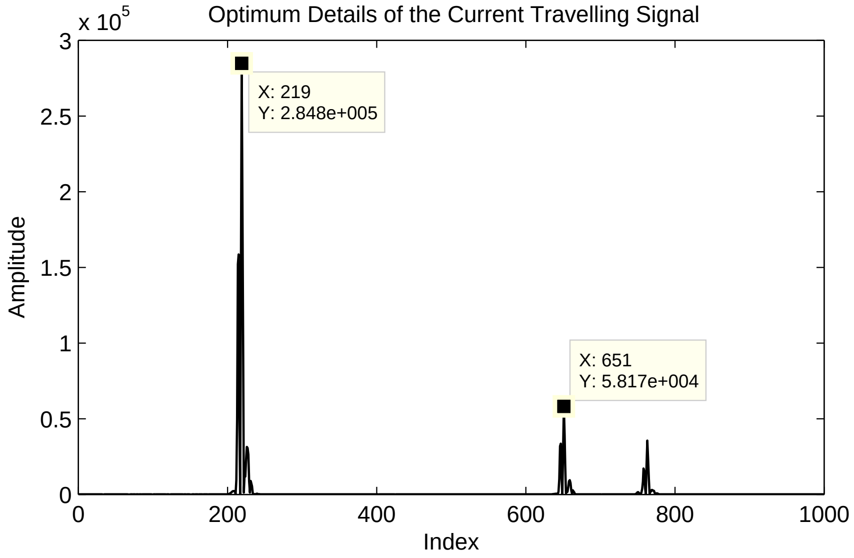

Figure 5.10: Optimum details of the aerial mode current traveling signal: the horizontal axis is the time in samples and the vertical axis is the signal magnitude in Amperes.

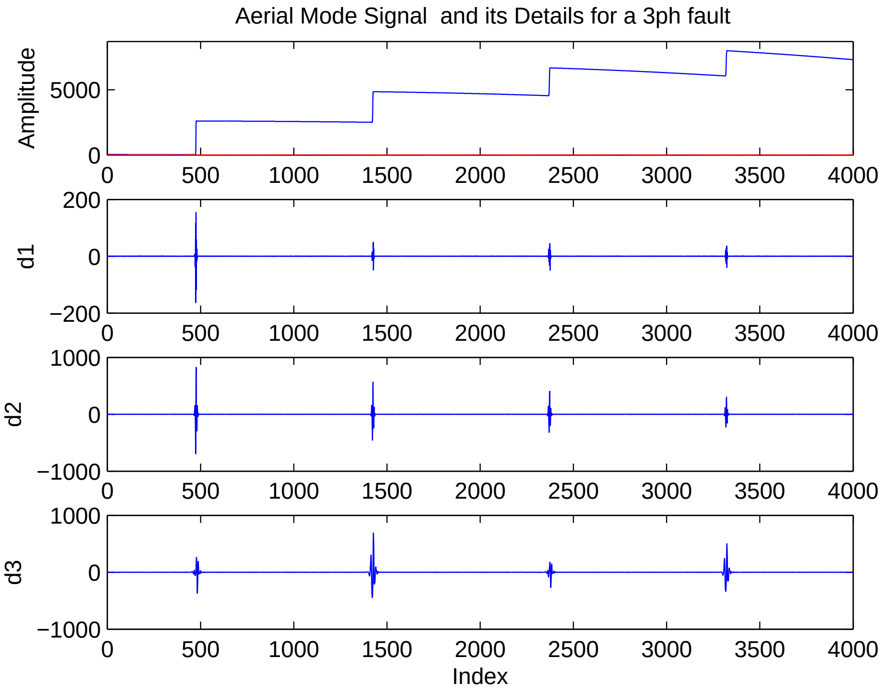

Figure 5.11: Three-phase fault aerial mode current signals for a three-phase fault at 112.2 km from A: the horizontal axis is the time in samples and the vertical axis is the signal magnitude in Amperes.

- Single-phase faults: Figure 5.12 shows the detailed signal for a single-phase to ground fault located at 112.2 km from bus A. The algorithm classifies the fault as grounded because the WTCs of the ground mode are significant. The time difference between these two signals is 0.1024 ms which is greater than the time difference produced by a fault located at the center of the line. Therefore, the algorithm classified the fault as grounded and located on the remote half of the transmission line with respect to bus A. In this case, the fault distance *x* is given by (5.7) but the time difference *dt* is replaced by

$$dt = \frac{2L}{v} - (t_2 - t_1) \tag{5.9}$$

where: L is the line length and $(t_2 - t_1)$ is the time difference between two consecutive peaks of the maximum value $|WTC|^2$ of the aerial mode (mode 1). Substituting (5.9) into (5.7) we can find the fault location *x* as:

$$x = L - \frac{v\,(t_2 - t_1)}{2} \tag{5.10}$$

Now the fault location can be calculated from the optimum level which was level 1 in

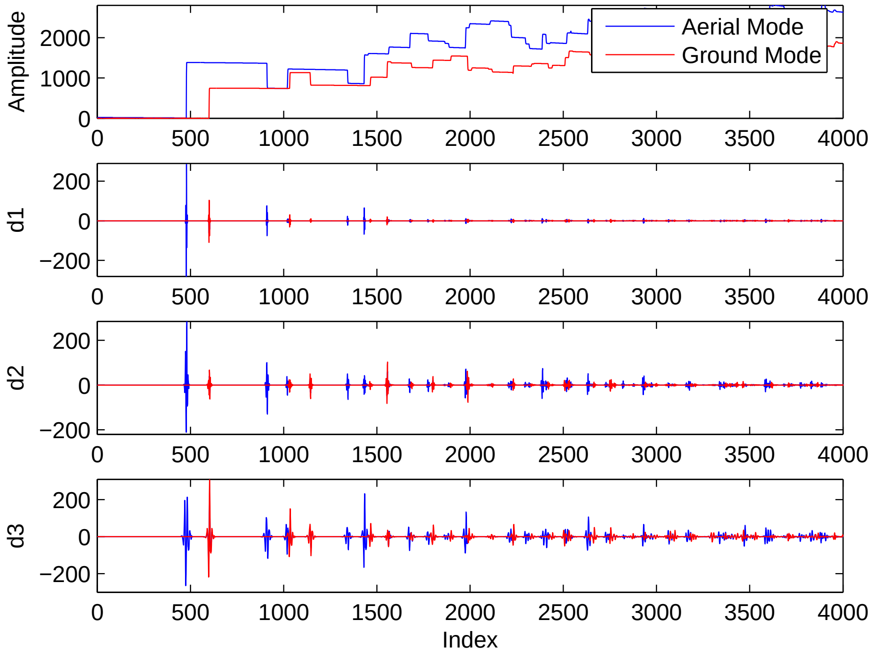

Figure 5.12: Aerial and ground mode details for a single-phase fault at 112.2 km from A: the horizontal axis is the time in samples and the vertical axis is the signal magnitude in Amperes.

this case as $dt = \frac{2\times163}{294115} - (915 - 475) = 0.75641$ ms.

The fault distance *x* can be calculated using (5.7) as follows:
$x = \frac{294115 \times 0.75641 \times 10^{-3}}{2} = 111.2358$ km
The error is about 964 meters. It can be shown that as the fault is moved far from the measuring end, the error is increased. This is because the TW signals suffer attenuation and distortions as they travel along the line.

5.2.2 Performance Evaluation

Several fault types, fault locations, fault inception angles and fault resistances were simulated by the ATP/EMTP. Therefore, the performance of the fault location techniques was verified using a set of cases whose results are reported and discussed. Results show that the single-ended technique is suitable for locating faults of unshielded EHV transmission lines. Also, the proposed fault locator performed accurately and reliably using simulated data obtained from the unshielded 400-kV transmission line. The distances are measured from A end of transmission line. The error of the fault location is calculated as follows:

$$error(\%) = \frac{Actual\ Fault\ Location - Calculated\ Fault\ Location}{Total\ Line\ Length} 100 \tag{5.11}$$

The intensity of a traveling wave largely depends on the angle of the voltage wave at the time of occurrence of the fault. When the fault inception angle is close to 90 degrees, the intensity of a generated traveling wave is the highest. The intensity of a traveling wave decreases with the deviation of the fault inception angle from 90 degrees. Traveling waves are not generated, if the voltage angle is close to 0 degrees at the time of occurrence of a fault. At small fault inception angles, the fault locator does not detect the transients, but it gives accurate results for fault inception angles (FIA) more than 5 degrees as shown in Table 5.1. Another factor that affects the traveling wave intensity is the distance. The traveling waves propagate with a finite speed and their intensity decreases as the distance traveled increases. A traveling wave originated at a farther location takes longer time to reach the fault locator than a wave originated at a nearer location.
Different locations of single-phase faults are applied at 10 km intervals of the transmission lines. The results of varying the fault location at a 90-degrees fault inception angle are shown in Figure 5.13.

At the middle distance, a reconstructive received signal appears from the remote bus, which

Table 5.1: *Fault location error for a fault at 63 km from A*

FIA	Calculated FL	Error %	Error [km]
0	0.8163	38.1495	62.1837
5	62.54	0.2822	0.46
10	62.54	0.2822	0.46
15	62.54	0.2822	0.46
20	62.54	0.2822	0.46
25	62.54	0.2822	0.46
30	62.54	0.2822	0.46
35	62.54	0.2822	0.46
40	62.54	0.2822	0.46
45	62.54	0.2822	0.46
50	62.54	0.2822	0.46
55	62.54	0.2822	0.46
60	62.54	0.2822	0.46
65	62.54	0.2822	0.46
70	62.54	0.2822	0.46
75	62.54	0.2822	0.46
80	62.54	0.2822	0.46
85	62.54	0.2822	0.46
90	62.54	0.2822	0.46

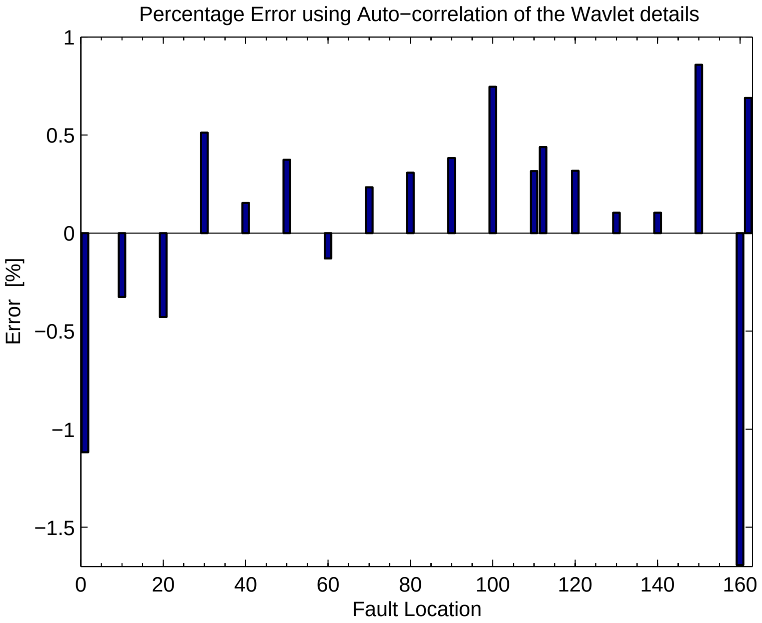

Figure 5.13: Percentage error as a function of fault location

makes the location of the fault. This case is analyzed for fault at half of the line and 49.69 and 50.92 percent of the transmission line length. The blind spots are located. The error is -0.6855 percent for a fault at 49.1 percent of the line while it is difficult to find the reflection from the fault at half of the line length in the case of stiff remote source impedance. This case is illustrated in Figure 5.14 in which the reflection is negligible for a fault at exactly half of the line length. The blind spots lie 500 m around the middle of the line length. The intensity of the traveling waves decreases when the fault resistance increases. The cases were simulated by modeling different resistances of the fault. The attenuation of the traveling wave signal has been calculated and the result is shown in Figure 5.15. From the previous results, it is concluded that the current traveling wave attenuates when fault resistance increases. Different cases were simulated by varying the values of the fault resistance from 0 to 200 Ω in steps of 10 Ω.

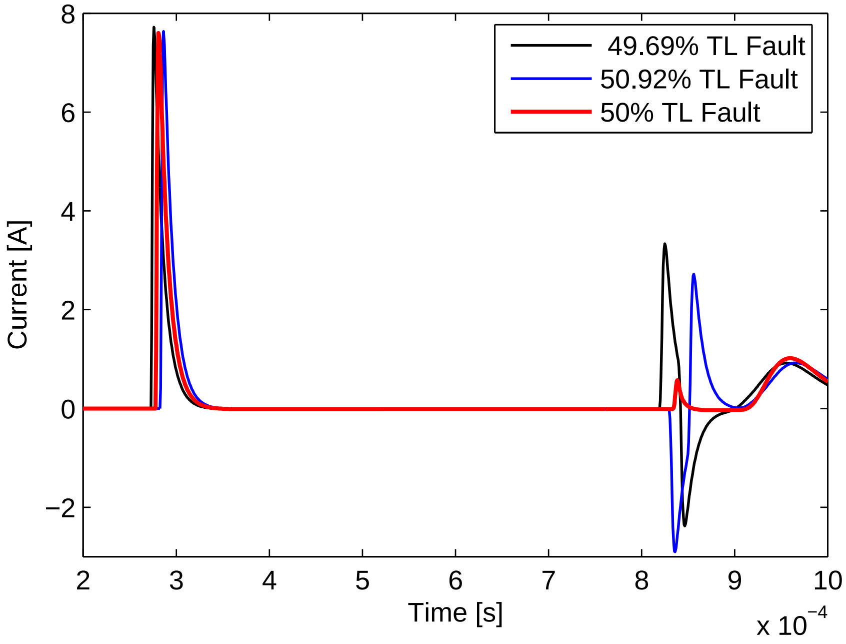

Figure 5.14: Reflected signal for faults close to half of the line length

The effect of the current transformers including the coupling transducers and the secondary wiring is uniform up to 100-kHz after which the error increases as can be concluded from Figure 4.7. Thus, for faults located at a distance less than 1.47 km from the measuring point, it is difficult for the algorithm to find the fault location when the transient frequency is higher than 100 kHz for a 163-km transmission line and a speed of propagation of 294330 km/s.

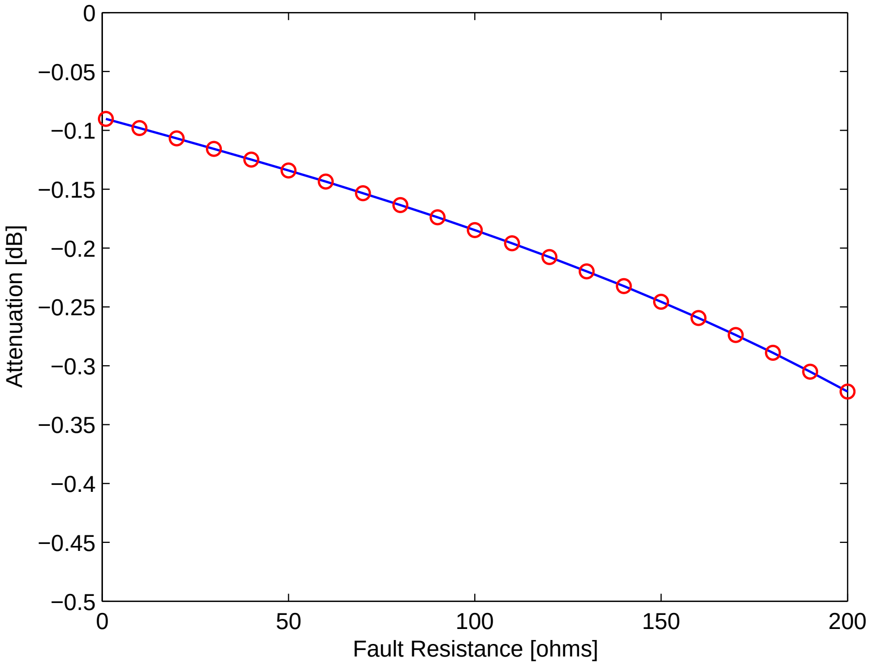

Figure 5.15: The attenuation of the current traveling signal for a fault at 63-km

5.3 Wavelet Correlation Function

The auto-correlation of different levels of the wavelet transform makes possible the extraction of periodicity in wavelet coefficients [125], [127]. The multi-level WCF described by (3.20) is used in the traveling wave fault location at each details level. From the simulation results, DWTs of levels higher than 3 have smaller values of peak amplitude. Therefore, only levels 1, 2, and 3 are used in the following simulations. When the DWTs of the modal current waves are available, the sub-band WT correlation operation can be executed within each level. Similar to the traditional correlation function, a template is extracted from the WT of the forward wave, which is centered around the first peak. This is because the maximum energy is concentrated at a certain level corresponding to a particular frequency and depending on the center frequency of the mother wavelet. This leads to the proper traveling wave speed for that specific transient event. The propagation speed is calculated for that level using the same transient for a fault at the end of the transmission line in the ATP/EMTP program. The maximum value of the WTC^2 at the selected level is used to calculate the time differences between two consecutive peak values. An example of the wavelet correlation for a fault at 50.8 km from busbar A is shown in Figure 5.16.

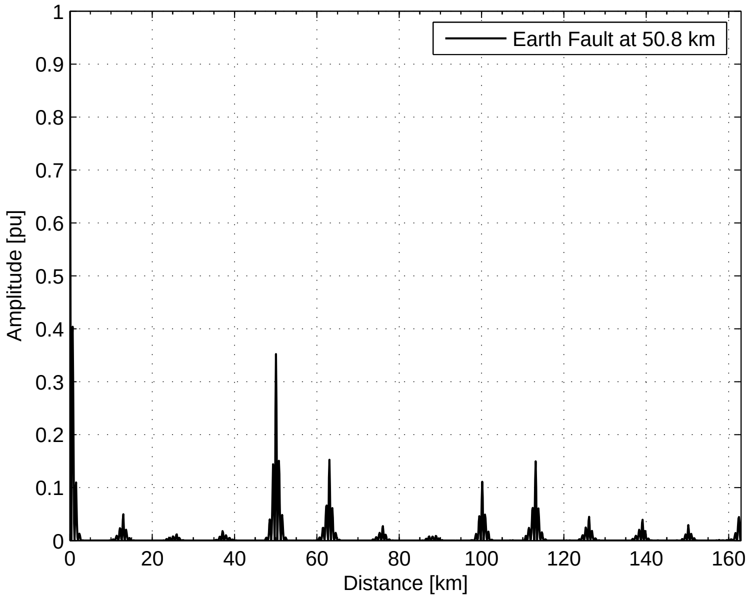

Figure 5.16: The wavelet correlation for a fault at 50.8 km from bus A

5.4 Performance Evaluation using ATP/EMTP

The ATP/EMTP solution with embedded ground wires in the LCC program cancels these ground wires. In this section, the modal components' delay method is used to calculate the fault location based on the TW current signals at one end of the line. The main idea is to utilize the inherent time delay between the different modal components of the incoming three-phase current signals for unshielded transmission lines. This is mainly performed to determine the region where the fault is located, either in the first or the second half of the transmission line length. Once the approximate region is determined, the exact location of the fault will be calculated based on the DWT of the aerial mode signal. Simulations are carried out using the ATP /EMTP program. All lines are modeled with the JMarti frequency-dependent parameter transmission lines. The steps of the method proposed for the transmission line fault location is given below [116]

- The signals are extracted from the current transformers and inductive couplers' output.
- The three-phase signals are transformed into the modal domain using Clarke's transformation matrix [79].
- The modal signals are decomposed using a multi-resolution analysis of the DWT and the WTCs are obtained.

- If the WTCs of the ground mode are zeros, the fault will be identified as ungrounded, and the fault distance will be given by (5.12):

$$x = \frac{v\ dt}{2} \tag{5.12}$$

where *x* is the distance to the fault, *v* the wave speed of the aerial mode (mode 1), and *dt* is the time delay between two consecutive peaks of the WTC power delay profile (WTC^2) in the aerial mode (*dt* = $t_2 - t_1$) of the recorded current signals at terminal bus A.

- If the WTCs of the ground mode are non-zero, the fault will be identified as grounded and the time difference between the aerial mode and the ground mode WTCs (t_{d0}) is compared with the time difference for a fault occurred at the middle of the line (t_{dm}).

  - If t_{d0} < t_{dm}, the fault occurs between the relaying-point bus and the mid-point (close-in fault) where the fault can be calculated using (5.12).

  - If t_{d0} > t_{dm}, the fault occurs between the mid-point and remote-end bus (remote-end fault). Some reflections from the remote-end will arrive at the sending station before the first reflection from the fault point. This introduces a complexity in recognizing the second peak, which corresponds to the reflection from the fault point, among the others. Moreover, the peak magnitudes are rapidly reduced as a result of the transmission line attenuation. In this case, the fault distance *x* is given by (5.12) but the time difference *dt* is replaced by:

$$dt = \frac{2L}{v} - (t_2 - t_1) \tag{5.13}$$

where *L* is the line length and ($t_2 - t_1$) is the time difference between two consecutive peaks of the absolute value wavelet coefficients WTC^2 of the aerial mode. Substituting (5.13) into (5.12), one can find the fault location *x* as

$$x = L - \frac{v\ (t_2 - t_1)}{2} \tag{5.14}$$

These signals were processed using the wavelet toolbox of MATLAB [119]. The system is simulated under several earth fault simulations at different locations, fault inception angles and fault resistances. Figure 5.17 shows modal current signals for a fault occurring at 50.8-km from busbar A. The proposed method calculates the fault location based on the sampled signals at one end for unshielded overhead transmission lines.

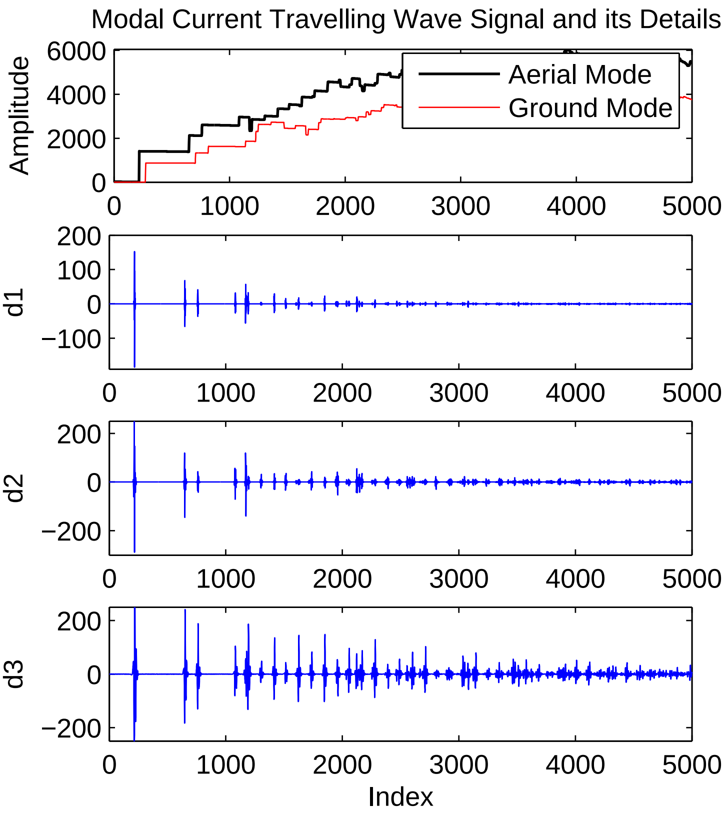

Figure 5.17: Aerial and ground mode signals and their details: the horizontal axis is the time in samples and the vertical axis is the signal magnitude in Amperes.

This method can only be applied to overhead lines without ground wires and/or counterpoises.

- else, calculate the fault distance using (5.12).

5.5 Effect of Grounding Wires and Counterpoises

Three other transmission line configurations have been analyzed where the line is equipped with overhead ground wires, counterpoises, and overhead ground wires and counterpoises. The time difference between the aerial and ground mode is significant if the line model used has embedded ground wires in the ATP/EMTP model or in practice, if there is no ground wire. In the ATP/EMTP simulation, this difference is about 24 μ sec (between the aerial and ground modes with and without ground wires that are embedded in the program) as shown in Figure 5.18. However, if the line is modeled using separate ground wires as phases, there will be no time difference between the modal components because part of the ground mode signal will propagate through the ground wires. On the other hand the LCC program considers the ground wire potential as if it has zero potential and all the ground mode component pass through the earth only. A comparison between the two cases is shown in Figure 5.19 for a phase-to-ground fault at a typical 128-km, 400-kV transmission line. The aerial and ground mode

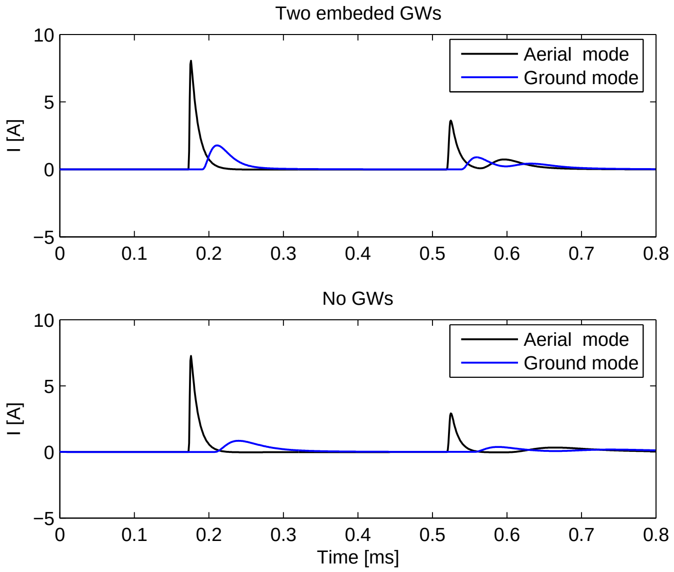

Figure 5.18: Aerial and ground mode high-frequency signals for a transmission line with and without ground wires

current signals arrived at about the same instant for separately modeled ground wires, while a considerable time delay exists between the aerial and ground mode for the case of embedded ground wires. The mother wavelet is selected automatically by the algorithm presented in Section 3.3.4 as ‘bior2.4’ for the aerial mode and ‘bior2.6’ for the ground mode. Figure 5.20,

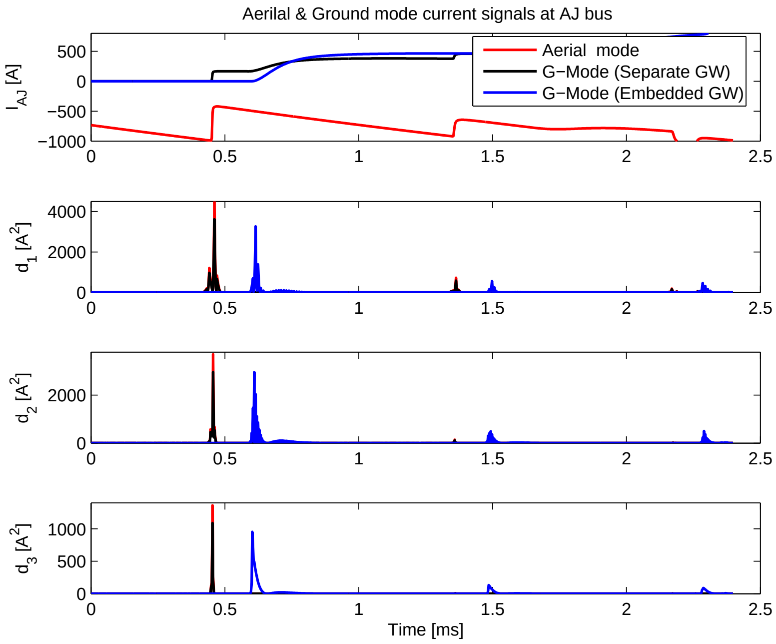

Figure 5.19: Aerial and ground mode signals of a simulated 400-kV earth fault at AJ-YL line

shows the aerial and ground mode DWT details at six levels. The ground mode signals arrive at the same instant as the aerial mode. For the case modeled with separate ground wires, the percentage of ground wire currents compared to the total ground mode currents are Fourier transformed and the results are presented up to 250 kHz in Figure 5.21. The ground wires carry a high percentage of the fault signal at different frequencies as shown in the second curve. The other combinations of the transmission line configurations is shown in Figure 5.22 in which Figure 5.22(a) shows without ground wires, Figure 5.22(b) shows the case with two ground wires, Figure 5.22(c) shows the case with only two counterpoise wires, and Figure 5.22(d) shows the case with both two ground wires and two counterpoises. As can be concluded, with transmission line equipped with ground wires or counterpoises or both, the ground mode TW signal arrives at the same instant as the aerial mode.

This phenomena makes the single-end method difficult to perform when modeling the GW separately. The aerial and ground mode time difference at a lower frequency band of DWT coefficients can be used. However, low frequency DWT details levels have low time resolution.

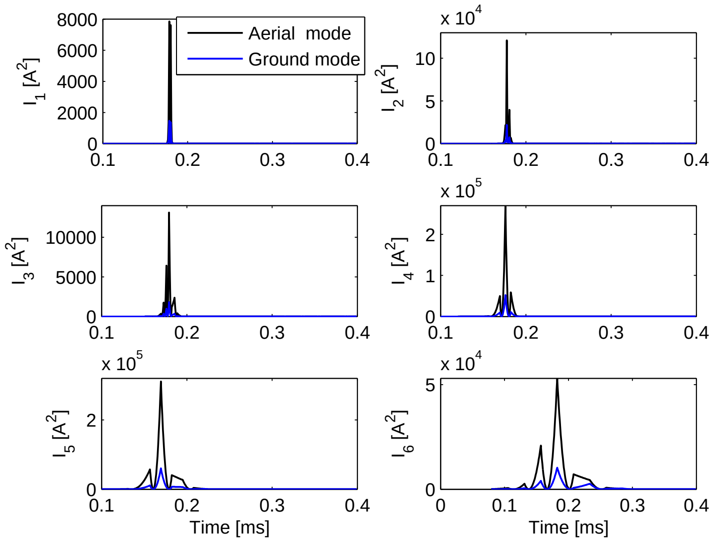

Figure 5.20: Aerial and ground mode DWT details for a transmission line with ground wires

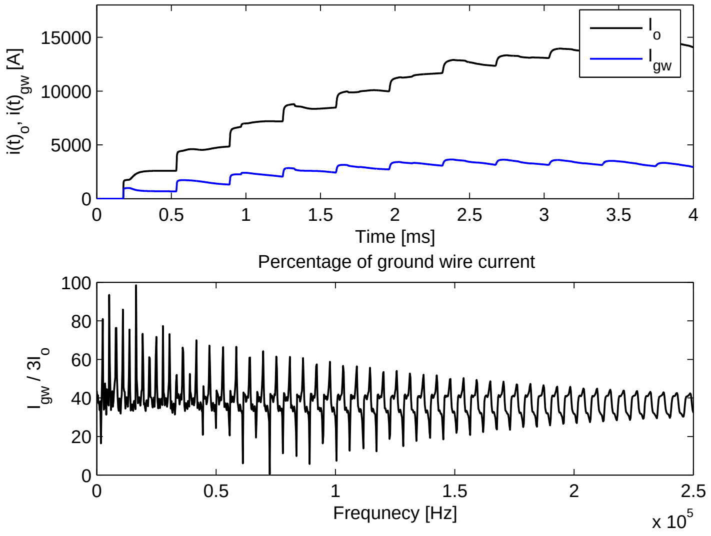

Figure 5.21: Aerial mode and ground-wire currents for different transmission line configurations

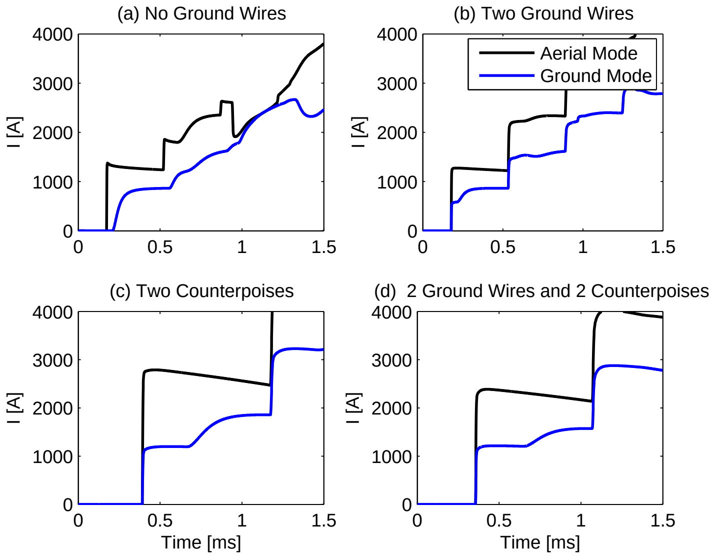

Figure 5.22: Aerial mode and ground mode currents

5.6 Investigation of 400-kV Line Practical Measurements

TW current measurements have been collected from FinGrid Oyj company, the transmission operator of the Finnish networks. The bus names are shown in the single line diagram of the 400-kV network in Appendix A. A real fault case at AJ-YL line was recorded by the TWRs for an earth fault at 244 km from YL between AJ-YL line. The TWR signals are depicted in Figure 5.23. These signals are analyzed using the single-end method and the aerial and ground mode details are extracted using the DWT analysis. Figure 5.24 demonstrates the aerial mode, the ground mode signals, and the DWT details at three details levels. It is evident that, at high frequencies, the time delay between the aerial and ground mode is negligible since a large part of the ground mode signal arrive at the TWR through the overhead ground wires. Multi-end method; which will be presented in Chapter 6, can be used to solve this problem using at least two TWR signals.

5.7 Investigation of 110-kV line Practical Measurements

There are few real fault cases that have been captured by the TWR recorders installed at a 110-kV line between Rautaruukki (RA)- Pyhäkoski (PY) substations. The line has a total length of 81.56 km with a TWR installed at both ends. The traveling wave signals have been analyzed using the DWT at six levels. The modal signals and their details are shown in Figure 5.25. The

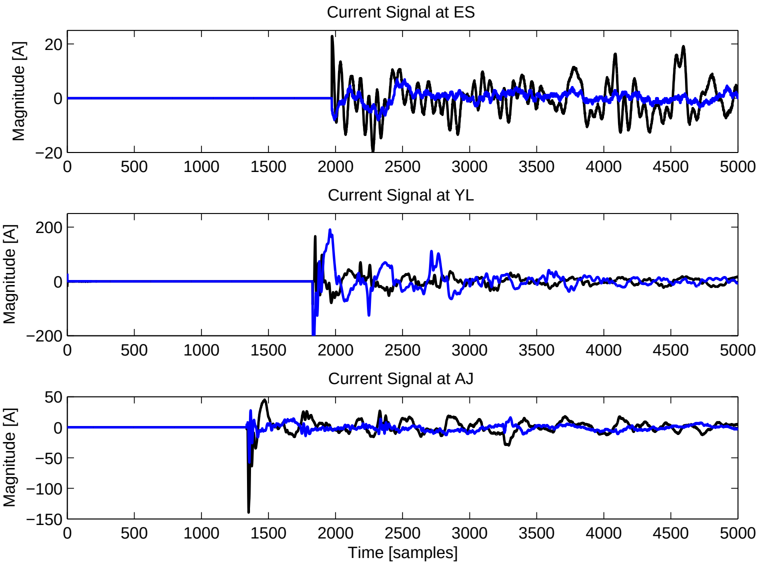

Figure 5.23: TWR current signals of a real 400-kV earth fault at AJ-YL line

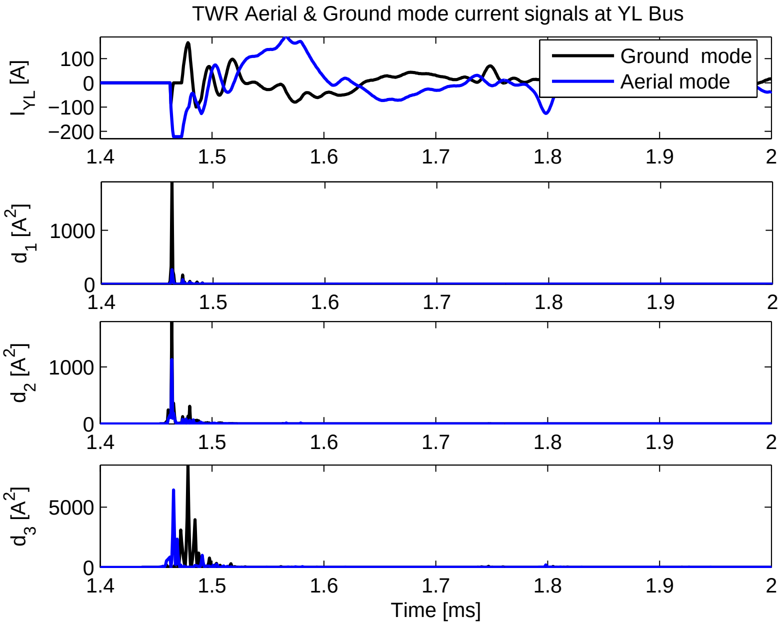

Figure 5.24: TWR Aerial and ground mode signals of a real 400-kV earth fault at AJ-YL line

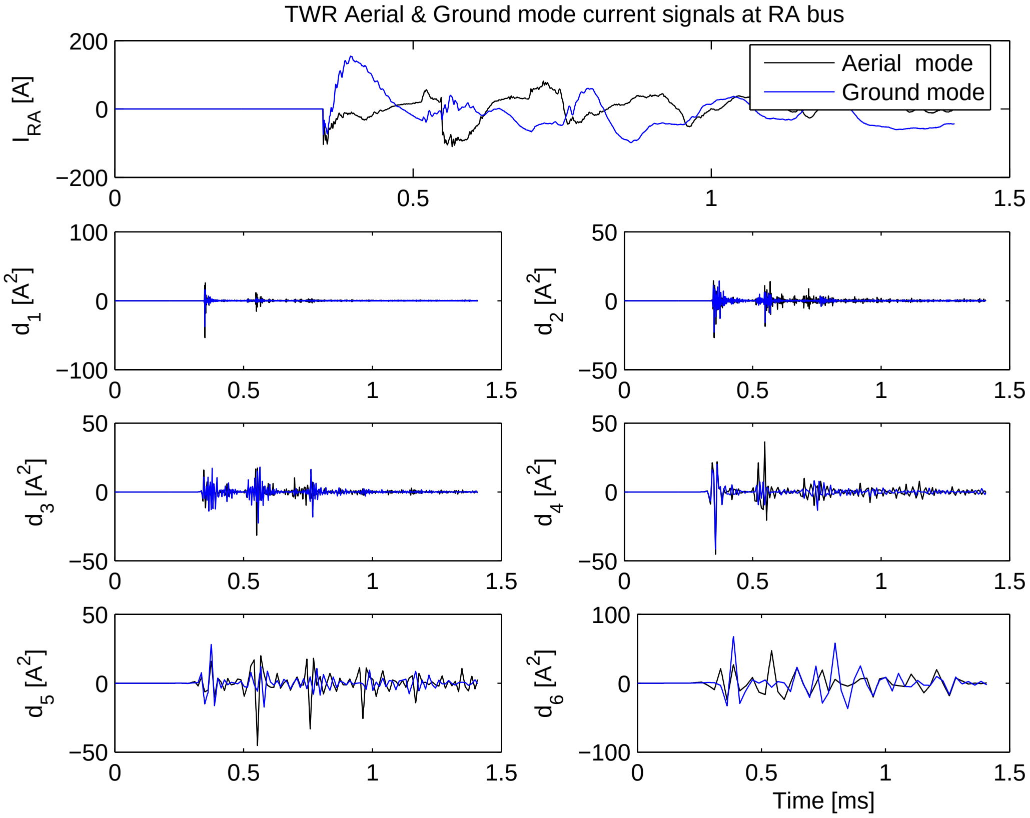

Figure 5.25: RA bus signals for a fault at 30.06-km from RA bus

signals recorded at PY- bus are depicted in Figure (5.26). Therefore, it is concluded that the time difference between aerial and ground modes is small and can only be estimated at low frequency bands. In practice, remote-end faults are difficult to find and sometimes impossible because of attenuation. To overcome this problem, each details WTC are multiplied by their absolute values as follows:

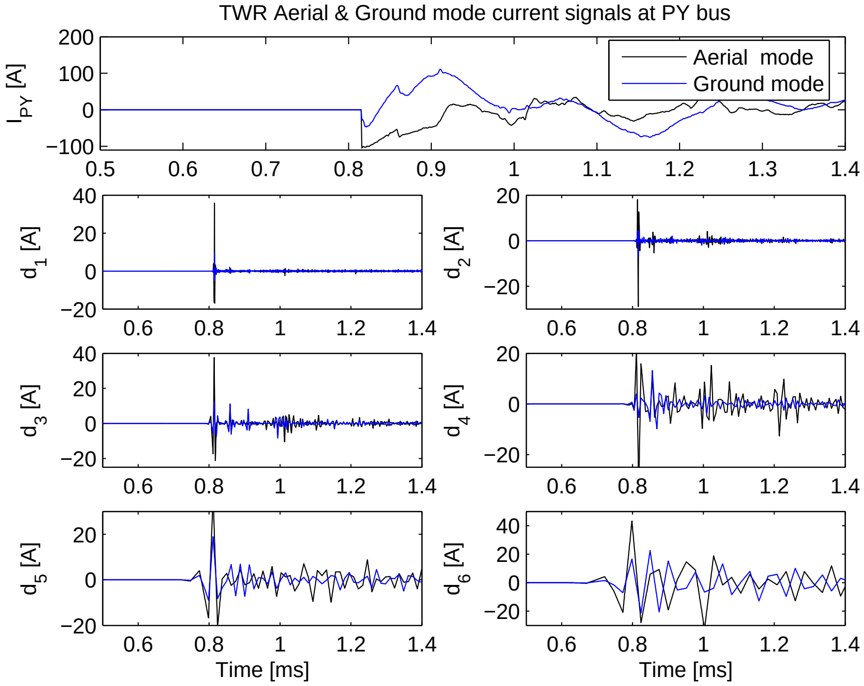

Figure 5.26: PY bus signals for a fault at 51.5 km from PY bus

$$DWT^{|2|} = DWT \times |DWT| \tag{5.15}$$

The polarities of the initial and first-reflection of the transient signal are compared. If the polarity of both transients differ, the fault location is located at the remote-end of the line as it is calculated by (5.9). The modal signals and their wavelet coefficients are depicted in Figure 5.28.

Alternatively, if both transients have the same polarity, which indicates a close-in fault, the fault location is calculates using (5.12). Figures 5.25 and 5.26 are repeated in Figure (5.27) and Figure (5.28) respectively, with a window of 0.6 s and three details levels for clarity. The distance estimates from both ends, using single-end method, were 30.27 km from RA bus and 52.61 km from PY- bus. This makes an average error of about 120.5 meters. As a conclusion, it is practical to use the polarity of the second reflected signal in transmission lines equipped with ground wires and/or counterpoises rather than using the delay difference of the modal components of the traveling wave signal.

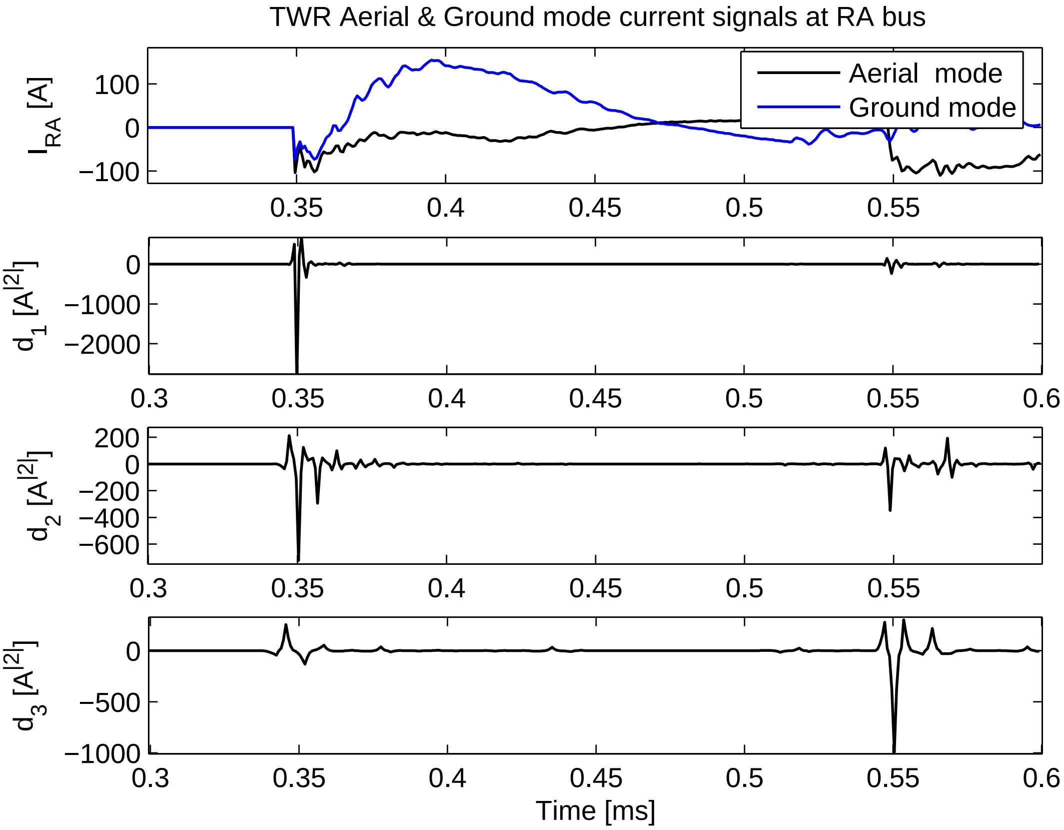

Figure 5.27: $DWT^{|2|}$ coefficients for a fault at 30.06 km from RA bus

5.8 Summary

As the method of modal components time delay does not give satisfactory results for lines equipped with ground wires and/or counterpoises, the solution of the single-end problem for faults at the second half of the line can be mitigated using the energy of the DWT details as discussed in Section 3.3.5. The details energy has lower values for a fault at the remote end of the line than those at the close in end of the line. Therefore, The energy method is used, in this case, to discriminate between close-in and remote-end faults. Furthermore, the polarities initial and reflected transient signals can be compared to distinguish between close-in and remote-end faults using (5.15).

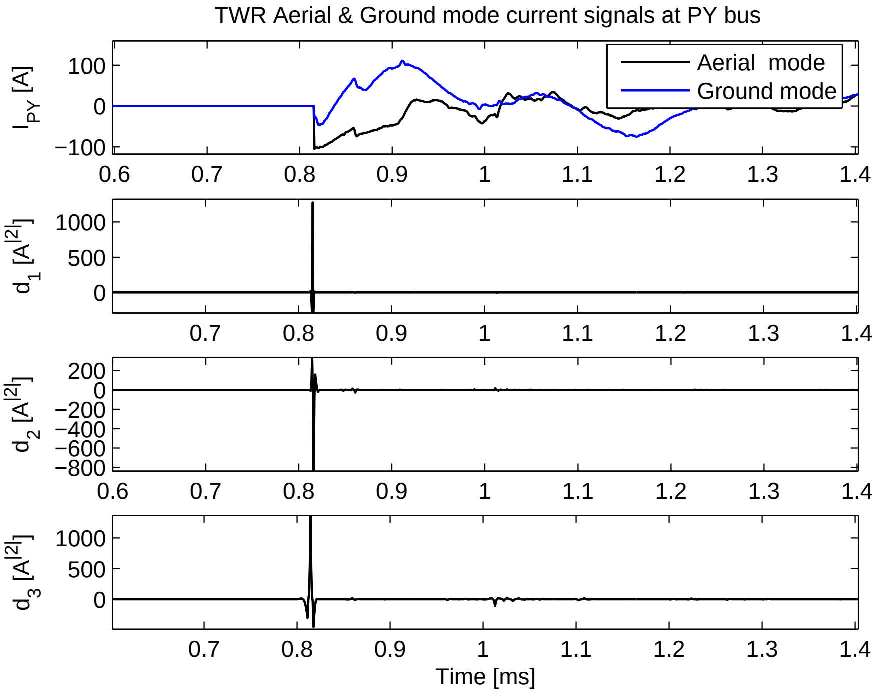

Figure 5.28: $DWT^{|2|}$ coefficients for a fault at 51.5 km from PY bus

Chapter 6

Multi-end Method

6.1 Introduction

Various methods and different techniques of fault location have been developed in the literature. In traveling wave-based method, the fault location can be found by comparing the arrival time of the initial and reflected transient signals at a single end of the line terminals. Single-ended methods show more economical advantages. In double-ended method, most of the research work was concentrated on two-end or three-terminal methods [130] - [135]. However, in meshed networks, the single-ended method has many disadvantages because of multiple reflections from different impedance discontinuities such as bus and transformers which arrive the measuring point from multiple paths. These multi-path reflections impose many difficulties in identifying the main reflection from the fault location. Moreover, the double-end method is uneconomical, as it requires a traveling wave recording units (TWR)installed at each monitored bus.

This chapter focuses on finding the fault location when there are few TWR installed at sparsely located buses in the transmission network. The power lines studied are part of the 400-kV Finnish EHV transmission system with few traveling wave recorders is shown in in Appendix A. This system has been modeled by the ATP/EMTP using the graphical user interface ATP-Draw [70], [69]. In practice, these TWR recorders are connected to inductive couplers which are basically a split-core current transformers connected to the secondary of the main current transformers of the substation. The simulations were performed using the ATP/EMTP program with the preprocessor ATPdraw as shown in Figure 6.1.

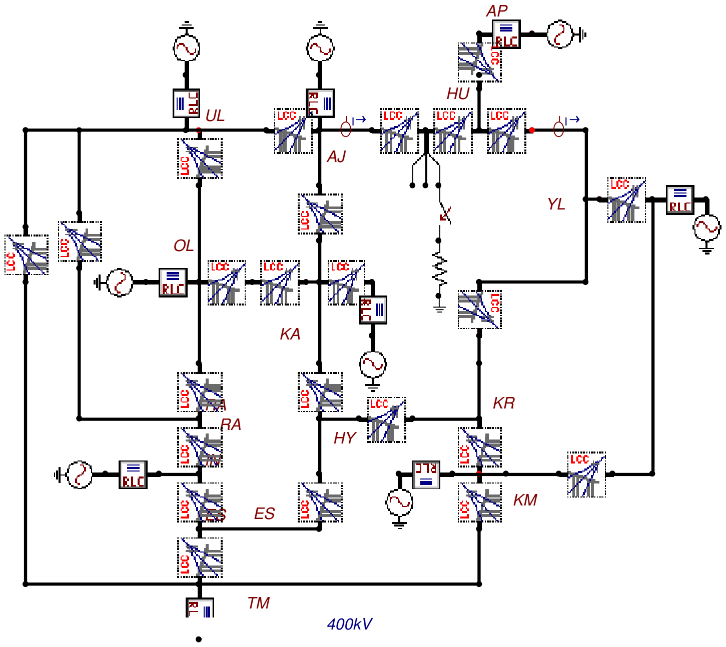

Figure 6.1: ATP/EMTP simulation of the 400-kV network

6.2 The Proposed Fault Locator Algorithm

The number of installed TWRs is usually less than the number of buses. Consequently, efficient methods are needed to find the fault from only those existing TWR units [130]. Recently, traveling waves and the wavelet transform of the current transients are used to extract initial arrival times of fault initiated waves reflected from the fault point. In [130], a method was developed to estimate the fault area using several recorders scattered throughout the system by comparing a fault signature record with calculated fault signatures. Considering few recording units installed at few monitored substations in the power system, the proposed algorithm uses the nearest two TWR to locate the fault point. The fault location is determined by accurately time-tagging the arrival of the first traveling wave signals at these monitored substations and comparing the time difference to the total propagation time of the lines [131]. The time reference signal can be attained using satellite from the Global Positioning System (GPS) [132] - [136]. The calculation of the fault distance is, therefore, carried out using double-end method and the captured signals of the pre-selected two TWRs [132], [133]. The signals are analyzed using the DWT. A method of selecting an optimum mother wavelet and an optimum level according to the signal's energy content was presented in Chapter 3. The minimum travel time of the current traveling wave signal traveling to the nearest TWR has been calculated using Dijkstra algorithm [137]. Dijkstra's algorithm is used for searching the shortest travel time in the transmission network. The shortest path is calculated by finding a path of minimum distance (weight) connecting two specified nodes in a weighted graph. Simulation results indicate good correlation between the estimated and actual fault locations for the studied network shown in Figure A-2. The line lengths are as listed in Table 6.2.

Table 6.1: *Line lengths of the transmission network*

Line	Lenghth [km]	Line	Lenghth [km]
OL- KA	163	OL-RA	14
OL-UL	47	KA-HY	131
KA-AJ	173	KA-TO	82
ES- HY	81	ES- RA	238
ES- TM	27	TM- UL	224
UL- RA	43	AJ-UL	233
AJ-HU	221	HU-YL	151
YL-KR	87	KM-TM	124
KR-HY	172	KR-KM	34
KM-YL	132		

The buses are named using two capital letters as an abbreviation for the TWR. The TWR are already installed at the Finnish 400-kV network in such a way that they monitor almost all the 400-kV lines. The TWR installed at substation buses OL, AJ, YL, and ES are used in this chapter. In certain areas there are more than two transmission lines in the monitored substation.

6.3 Faulty Line Estimation

If there is a traveling wave recorder installed at a substation, the detection of the faulty line can be found by comparing the polarity of the incoming transient current signals. First all the three-phase current signals are transformed to modal components. If all polarities are the same, the fault will be at the substation bus itself. If one of the line current signals has a different polarity from the other lines' signals, the line with different polarity is the faulty one as shown in Figure 6.2 [139], [140], [141]. The fault is simulated at the OL-KA line and the measurements are captured at OL bus of Figure 6.1. The results shown in Figure 6.2 confirms that the faulty line OL- KA polarity is different from the healthy ones.

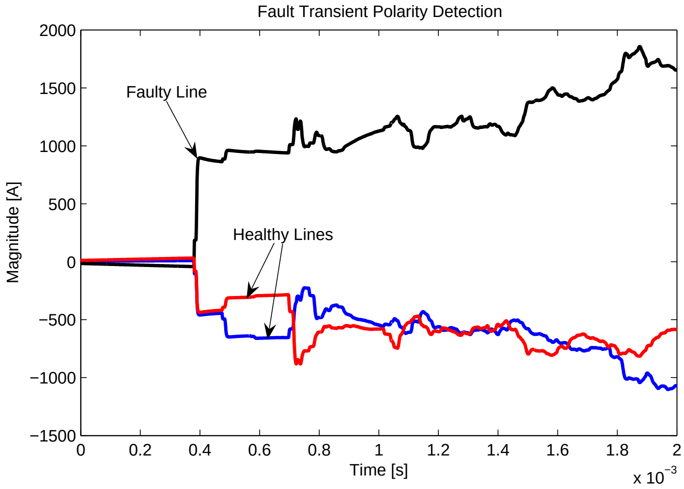

Figure 6.2: Modal current signals for faulty line detection

6.4 Multi-end Fault Location

The fault location can be calculated by comparing the arrival time of the initial transients at two substations A and B using the known propagation speed of the TW transient signals. Since different paths are taken by the TW signals, these waves arrive to different TWR recorder locations with different time delays. Each received signal component goes through a distinct transmission line and has a different signal strength and time delay. The fault location can be estimated using the arrival delays of a given fault transient at different locations in the power system knowing the minimum traveling time of these signals. The method used in this chapter assumes few recording units installed at few substations in the power system. The fault location is determined by accurately time-tagging the arrival of the traveling wave at these monitored ends of the transmission lines and by comparing the time difference to the total propagation time of the lines. The relevant lines and location of the current transducers are shown in Figure A-2.

This system has been modeled using the ATPDraw with three-phase current measurements at four substations: OL, AJ ,YL, and ES substation buses. A MatLab program has been developed to estimate the fault location from the first arrivals of the TW details' peak value of the nearest two TWR units. The minimum path for the traveling wave between the chosen two TWR units to the fault has been calculated using Dijkstra Algorithm [137]. Then, the fault distance is calculated by the double-end method using the chosen fault recording signals. For example, If an earth fault occurs at OL-KA line, the fault location can be calculated as follows:

$$FL_{OL} = \frac{Total \quad Length_{OL-AJ} + (T1_{OL} - T1_{AJ}) \times v}{2} \tag{6.1}$$

where $T1_{OL}$ is the traveling wave arrival time at end OL, $T1_{AJ}$ is the traveling wave arrival time at end AJ, $TotalLength_{OL-AJ}$ is the electrical line length between OL and AJ ends, and *v* is the propagation speed.

The fault location can be calculated by comparing the arrival time of the initial transients at two substations; OL and AJ, using the proper propagation speed of the transients, for instance, using the transmission line configuration in the LCC program. In some instances, however, recorded transients may only be available from one substation. In this case, the single-end method is the only solution to the problem.

The traveling-wave current data are sampled at 1.25 MHz and the signal is captured as a pre-fault and post-fault signals using a pre-determined threshold. The triggering is carried out using protection functions incorporated in distance relays. The signals are collected at a central computer for pre-processing and analysis. The DFT is the simplest method for finding the dominant high frequency signal. The fault transmitted signal follows many different paths before arriving at the receiving TWR, and it is the aggregate of these paths that constitutes the multi-path traveling wave signal propagation in meshed networks. The DWT itself represents a multi-path environment where each mother wavelet has its variation and decaying characteristic with time. A simple model for discrete multi-path TW models has the form

$$y(t) = \sum_{l=1}^{L} \alpha_l \Psi(t - \tau_l) \tag{6.2}$$

where $\Psi(t)$ is the band-pass WTC signal, α_l is the attenuation factor for the signal received on the l_{th} transmission line, and τ_l is the corresponding propagation delay. The arrival time of the TW signal can be found by time tagging with a threshold value at each DWT details level and finding the second TW arrival time using the same threshold. The speed of propagation using the delay at the maximum squared value of the wavelet details coefficients (WTC^2). To optimize the solution of the traveling wave locator, the propagation travel time delay of all transmission lines is calculated at different frequency bands of the DWT details levels for the simulated fault cases at the end of each transmission line. Then the propagation speed at each level is calculated using the previously calculated propagation times at each level. An optimal multi-end method to find the least error estimate for the fault distance is proposed and its implementation is shown in the flow chart of Figure 6.3.

1. For each TWR, the faulty transmission lines is detected based on the polarity of the TWR current signals as discussed in Section 6.3. Then, the signals are sent to the central computer with the network configuration at the instant of the fault.

2. The fault signal of each TWR is transformed to the modal domain.

3. The DWT of the aerial mode is performed as follows:

   - The optimum mother wavelet is selected based on the minimum error between the original and the reconstructed mother wavelet.
   - The optimum details level is selected based on its energy content.

4. The nearest two TWR signals are selected based on their received signal strength.

5. If the number of TWR signals is greater than one, calculate the nearest high TWR signal using the minimum propagation delay from the faulted line towards the nearest TWR. Otherwise, the single-end method is used.

6. For each TWR signal, the first packet of the received optimum detail coefficients of the power of fault signal is calculated to find the delay. The delay at maximum value of the delay profile is recorded for both TWR signals.

7. The double-end method is used to find the fault location using Equation (6.1).

8. If there is a Tee-off tapped line or an intermediate bus between the two TWR and the fault distance estimate was at that intermediate point, the fault will be either at that point or along the tapped transmission line. In this case, the average of the single-ended fault location method at both TWRs must be used. Some other sensing devices, such as wireless sensors, is proposed to be installed at the Tee-off point to detect the magnitude and the direction of the traveling wave signal. Moreover, the fusion of the protective relay detection operation with other intelligent electronic devices (IED) enhances the fault location estimation. This fault case is illustrated in Figure 6.4 for a fault on the line between KA and TO buses. $T1_{OL}$ and $T1_{AJ}$ are the traveling time of the first wave front to OL and AJ buses, respectively, and τ_{OK} and τ_{AK} are the travel time of the lines OK and AK, respectively.

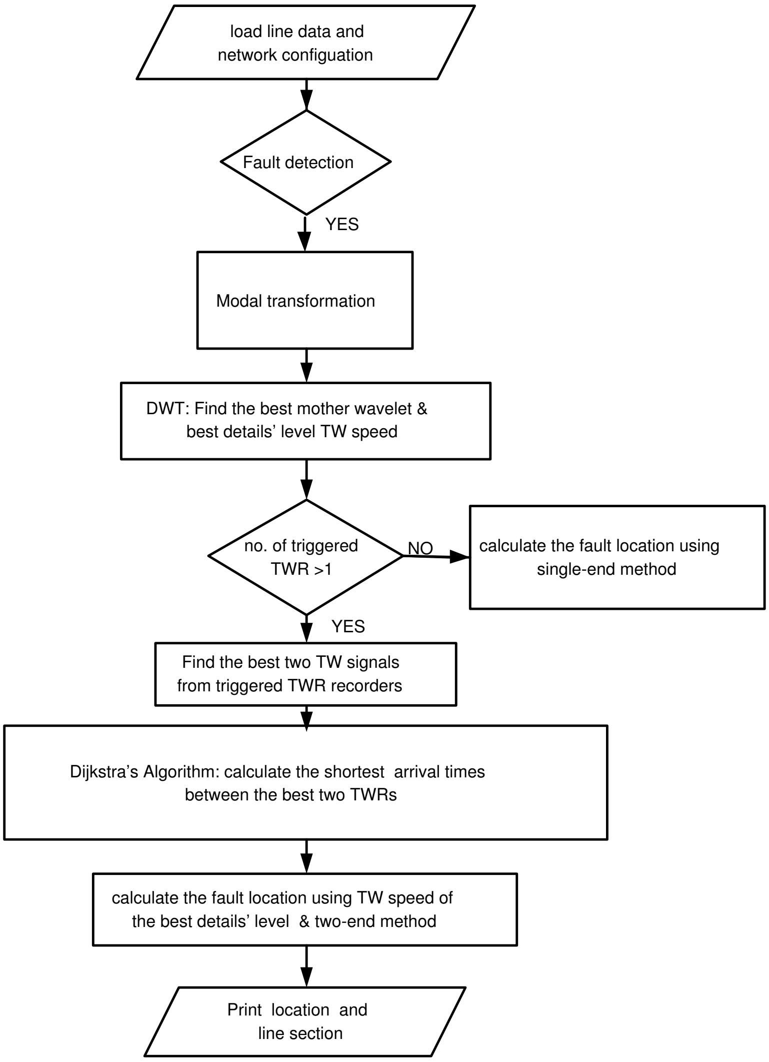

Figure 6.3: Multi-end traveling wave location algorithm

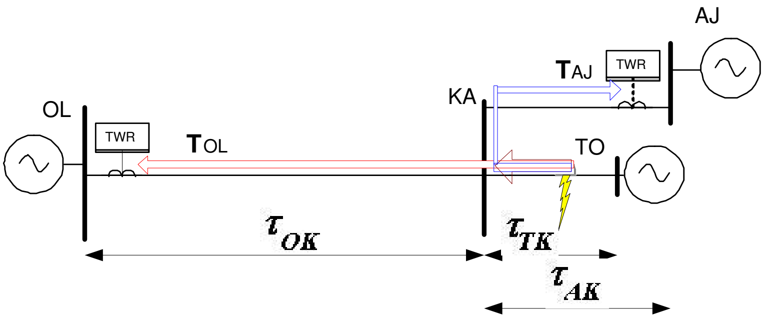

Figure 6.4: Fault location at for Teed transmission line

The multi-end method has been tested by simulating different fault locations for the Finnish 400-kV network using the ATP/EMTP. These faults are single-phase to ground faults between OL-KA buses and KA-TO buses of the transmission network of Figure A-2. The measured signals are at OL, AJ, YL, and ES buses for a window length of 4 msec. The signals have been filtered using a high-pass (HP) filter in the ATP environment using TACS (Transient Analysis of Control Systems) transfer function HP Filter. Also the fault location was calculated using the mean time delay method (MTD) which was presented in Section 3.5. Different threshold values were used to find the fault location and a mean threshold value (MThr) was selected. Finally the aforementioned methods were compared with the delay at the maximum value of the power delay profile (MaxPower) of the optimum wavelet details' coefficients. The results are shown in Table 6.2. The method of finding the maximum of the power of the fault signal (MaxPower) provides the minimum error for fault location. However, to calculate the time of the TW signal arrival, the speed of propagation of the same DWT details level should be used.

Table 6.2: *Fault location using multi-end method*

Fault Distance[km]	HP Filter	MTD	MThr	MaxPower	From Bus	to Bus
5	5.5797	5.7985	5.6926	5.0000	OL	KA
10	10.5647	10.3090	10.7720	10.5886	OL	KA
20	20.5349	20.8545	21.3924	19.9029	OL	KA
32.6	33.2873	33.3556	32.5899	32.9429	OL	KA
81.5	82.0946	82.0957	82.5751	81.3771	OL	KA
130.4	130.9018	130.8915	130.7132	130.7429	OL	KA
146.7	147.3642	147.1261	148.1445	147.5086	OL	KA
163	163.5946	163.2801	163.2670	163.3429	OL	KA
173	172.2895	172.7682	172.7330	172.6571	AJ	KA
1	1.2289	0.1008	0.2586	0.8212	KA	TO
5	4.9636	3.8106	3.9719	4.5469	KA	TO
10	10.7991	9.6072	9.7739	10.3683	KA	TO
16.4	18.0351	16.7950	16.9684	17.5869	KA	TO
41	42.3107	40.9087	41.1048	41.804	KA	TO
65.4	66.1195	64.5588	64.7770	65.5554	KA	TO
80	81.5251	79.8618	80.0944	80.9239	KA	TO

6.5 Error Analysis of the Traveling Wave Arrival Time

The calculation of the fault location is subject to various sources of uncertainty resulting from deviation of the calculated TW arrival time values from the actual ones. The main error sources are as follows:

1. Uncertainties in system modeling.
2. Estimation of modal quantities.
3. GPS timing error.
4. Transmission line attenuation.
5. Speed of propagation.
6. Transducer error.

The actual error is lying at a different location from what is estimated as the fault distance. This results from the various uncertainties involved in estimating the fault distance as mentioned before. To avoid this error, the bounds of the uncertainty for the fault estimation have to be estimated with the distance estimation. For example, the speed of propagation is bounded by the speed of light and the details level at which the transient has its maximum frequency.

The accuracy of the GPS received signal is a function of the error and interference on the GPS signal and the processing technique used to reduce and remove these errors. The same types of phenomena as found in microwave-range systems affect the GPS signals. Both types of systems are highly affected by humidity and multi-path. Humidity can delay a time signal up to approximately 3 m. Satellites low on the horizon will be sending signals across the face of the earth through the troposphere. Satellites directly will transmit through much less troposphere. Sunspots and other electromagnetic phenomena cause errors in GPS range measurements of up to 30 m during the day and as high as 6 m at night. Such errors are not predictable, but they can be estimated.

Multi-path is the reception of reflected, refracted, or diffracted signals in lieu of a direct signal. Multi-path signals can occur below or above the antenna. Multi-path magnitude is less over water than over land, but it is still present and always varying. If possible, the placement of the GPS receiver antenna should avoid areas where multi-path is more likely to occur (e.g., rock outcrops, metal roofs, substation roof-mounted heating, and air conditioning, outdoor switchgear, cars, etc.). Increasing the height of the antenna is one method of reducing multi-path at a reference station. Multi-path occurrence on a satellite transmission can last several minutes while the satellite passes overhead. Masking out satellite signals from the horizon up

to 15 degrees will also reduce multi-path effects.
Some error values summarized in [144] are as follows

- GPS time-keeping between receivers, 150 ns.
- GPS time tagging, 50 ns.
- TWR delay, 200 ns.
- Variations in CT secondary cable lengths, 500 ns.

Pre-fault data is buffered for 1.6 ms allowing for accurate GPS signal synchronization. The DSP memory is primarily for traveling wave signal storage with data for all channels continuously stored at approximately 1.25 MHz and a post-fault window of 12 ms with 8-bit resolution. An example of a real pre-fault signal is shown in Figure 6.5, where tagging the precise GPS time reference has different approaches. The maximum of the signal power ($I^2_{prefault}$) is adopted as it gives minimum error in fault location. There are different attempts to reduce the errors in the GPS signal but they are beyond the scope of this thesis [145], [146].

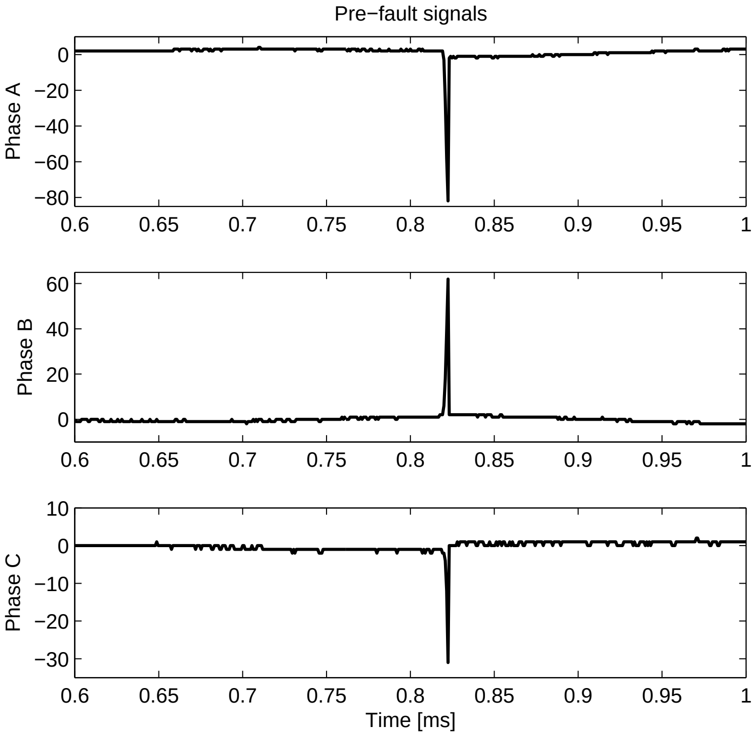

Figure 6.5: TWR pre-fault signals of a real 110-kV earth fault

6.6 Practical Investigation of a 400-kV Network Case

Measured fault traveling wave current signals at AJ, YL, ES, and OL buses were captured through the split-core CTs, which are connected across the secondary winding of the conventional CTs. All recordings are earth faults signals for the 400-kV network. These signals are analyzed using the DWT and the wavelet coefficients details output as depicted in Figure 6.6.

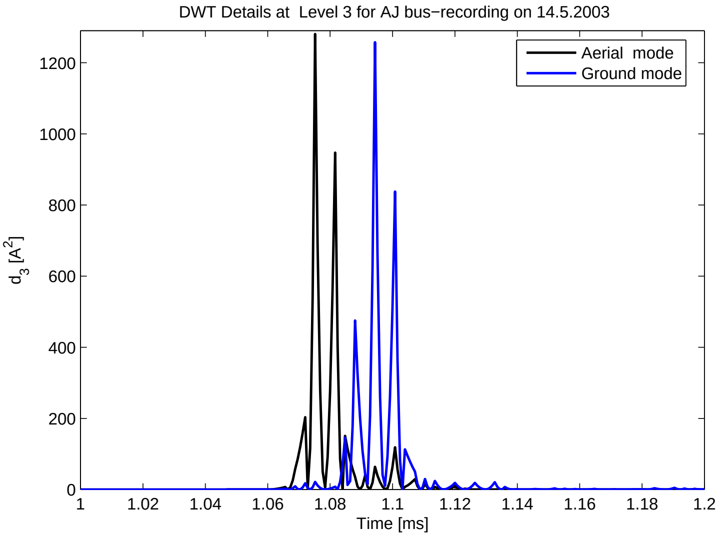

Figure 6.6: AJ bus aerial and ground mode details signal

This reveals the existence of the time difference between the aerial mode and the ground mode of a real fault signal at low frequency bands. However this difference is still small. The fault location is calculated using the optimum two recordings which were AJ and YL recordings. The signal strength of OL bus is low compared to AJ and YL signal strengths and therefore, it has been rejected from the calculation. Using the optimum details level, the fault was found at 197.88 km from AJ bus as shown in Table 6.3. The same situation has been simulated for a fault at 197.8 km from AJ bus using the ATP/EMTP case study of Figure 6.1. Applying the proposed multi-end method with the same fault location between AJ bus and YL bus yields similar results using three signal processing methods discussed in Section 6.4. From Table 6.3, the maximum of the power delay profile is the most effective method for finding the fault location [142], [143].

For another fault at 29.9 km from AJ bus, the fault was calculated using real TWR measurements as well as the ATP/EMTP simulations and the results are shown in Table 6.4.

Another case of fault location was estimated from the real recordings and simulation results

Table 6.3: *Fault location using TWR real and simulated fault signals at 197.8 km from AJ bus*

Fault Distance[km]	HP Filter	MTD	MThr	MaxPower	From Bus	Case
197.8	197.825	197.825	197.836	197.876	AJ	Recorded
	198.138	198.057	198.068	198.109	AJ	Simulated
174.2	174.096	174.175	174.164	174.124	YL	Recorded
	173.862	173.943	173.932	173.891	YL	Simulated

Table 6.4: *Fault location using TWR real and simualted fault signals at 29.9 km from AJ bus*

Fault Distance[km]	HP Filter	MTD	MThr	MaxPower	From Bus	Case
29.9	30.652	30.652	30.506	29.986	AJ	Recorded
	29.142	30.188	30.042	29.520	AJ	Simulated
342.1	342.391	341.348	341.494	342.014	YL	Recorded
	342.858	341.812	341.958	342.480	YL	Simulated

for a fault at 128 km from AJ bus. The results are shown in Table 6.5. The TWR signals are measured at ES bus, YL bus, AJ bus and are depicted in Figure 5.23 for an earth fault at 128 km from AJ bus. All the real faults were simulated using the network of Figure 6.1. Based on the previous results, the method of finding the fault from time tagging the maximum of the power delay profile is found to be the best one since it has the minimum error. The power delay profile can be found by squaring the optimum wavelet coefficients details of the aerial mode of traveling wave signal.

Table 6.5: *Fault location using TWR real and simulated fault signals at 128 km from AJ bus*

Fault Distance[km]	HP Filter	MTD	MThr	MaxPower	From Bus	Case
128	128.266	128.266	128.212	128.019	AJ	Recorded
	128.462	128.846	128.792	128.601	AJ	Simulated
244	244.121	243.734	243.788	243.981	YL	Recorded
	243.538	243.154	243.208	243.399	YL	Simulated

Chapter 7

Conclusions

This thesis presented a fault locator that is based on the characteristics of the traveling waves initiated from the fault. The signals are first decoupled into their modal components, and then transformed into the time frequency domain using the digital wavelet transform. This thesis has addressed the problem of fault distance estimation utilizing the measurements of current traveling wave signals from one end of a transmission line and a case of multi-end at sparsely located traveling wave locators.

The traveling wave theory was introduced in the second chapter and the properties of the traveling waves on transmission lines were also discussed. The objective of this thesis was to propose an automated technique based on traveling waves for finding the fault location in transmission lines and to test the performance of the technique compared to the existing ones.

The wavelet transform is extensively studied in this thesis to extract the traveling wave signals from the measurement in the CT secondary windings. An optimization method was carried out to select the best candidate of different mother wavelets. The selected mother wavelet was used to analyze the fault signal to different details. The best details level, which carry the fault features, was selected based on its high energy content.

The proposed method uses the measured fault current signals of the fault signals from conventional current transformers without the need of extra components. The experimental results reveal that CTs can be used for monitoring high frequency current signals over a range of several hundred kHz, which is suitable for traveling wave based fault locators. However, the CT construction, the filtering effects of the secondary wirings and other inductive couplers reduce the range down to 100 kHz.

The proposed method uses a single-ended method when there is one recording of the traveling wave fault signals. Based on the time difference between modes and between the reflected wavefronts within the aerial mode, the fault distance is calculated using high frequency band of the wavelet details coefficients. The error in fault location estimation is a function of the sampling rate and the speed of propagation. The techniques were tested using data generated by executing various cases in the ATP/EMTP. This method is based on modeling the overhead ground wires embedded in the ATP/EMTP or a transmission line without ground wires. However after investigating some real recordings collected using the traveling wave recorders allocated in the Finnish transmission system, it was found out that, at high frequencies, there is no time difference between the aerial and ground mode arrivals when the line is equipped with overhead earth ground wires and/or counterpoises. The main reason is that, at higher frequencies, the penetration of ground return currents into the ground is reduced but it is still existing at low frequencies. The applied fault cases on a transmission line in a selected power system were simulated using the ATP/EMTP. Various types of faults were applied at various locations on the transmission lines. The cases were also run by varying the fault resistance and the fault inception angle. The techniques provide correct results for different types of faults and for different values of the fault resistance. However, they produce high errors when detecting faults on a transmission line when the fault inception angle is close to zero degree. This behavior of the techniques is expected because traveling waves are not generated at this instant of the fault inception angle. However, the techniques can detect the fault when a fault occurs near to the fault locator.

Furthermore, an extension to the double-end method was proposed. Using only few TW recordings, the closest two TWR to the fault are found using Dijkstra's method. Using transmission line configuration data, the traveling wave speed is calculated by the DWT for each line using the optimum mother wavelet and details' level. The fault location is then calculated using the two nearest fault recorder units and the shortest time traveled by the TW fault signal. It is possible to achieve greater accuracy with the multi-end methods developed in this manuscript compared to the traditional fault location methods.

Further research is recommended to extend this thesis in the following concerns:

- Wireless traveling wave detection through directed antennas and/or other wireless sensors.
- Utilization of HV capacitive insulation tap currents of available CTs in fault location.
- Developing advanced signal processing techniques for analysing traveling wave signals.

- More detailed analysis of the traveling wave speeds for ground and aerial modes based on frequency-dependent transmission line models.

Bibliography

[1] L.V. Bewley, “Traveling waves on transmission systems”, Wiley, New York, 1951.

[2] D. Spoor and J. G. Zhu, “Improved single-ended traveling-wave fault-location algorithm based on experience with conventional substation transducers”, IEEE Transactions on Power Delivery, Vol. 21, 3, July 2006, pp. 1714 - 1720.

[3] T. Takagi, Y. Yamakoshi, J. Baba, K. Uemura and T. Sakaguchi, “A new algorithm of an accurate fault location for EHV/UHV transmission lines. Part I: Fourier transform method”, IEEE Trans. Power Appar. Syst. PAS - 100, 3, (1981), pp. 1316 - 1322.

[4] T. Takagi, Y. Yamakoshi, J. Baba, K. Uemura and T. Sakaguchi, “A new algorithm of an accurate fault location for EHV/UHV transmission lines. Part II: Laplace transform method”, IEEE Trans. Power Appar. Syst. 101, 3, (1982), pp. 564 - 573.

[5] T. Takagi, Y. Yamakoshi, M. Yamura, R. Kondow, and T. Matsushima, “Development of a new type fault locator using the one terminal voltage and current data,” IEEE Trans. Power Apparat. Syst., Vol. PAS-101, pp. 2892 - 2898, Aug. 1982.

[6] A. Wiszniewski, “Accurate fault impedance locating algorithm”, IEE Proc. 130, 6, (1983), pp. 311 - 314.

[7] L. Eriksson, M.M. Saha and G.D. Rockefeller, “An accurate fault locator with compensation for apparent reactance in the fault resistance negative sequence currents”, IEEE Transactions on Power Delivery, 5,1, (1990), pp. 79 - 84.

[8] S. A. Soliman, M. H. Abdel-Rahman, E. Al-Attar and M. E. El-Hawary, “An algorithm for estimating fault location in an unbalanced three-phase power system”, International Journal of Electrical Power and Energy Systems, Vol. 24, 7, Oct. 2002, pp 515 - 520.

[9] B.J. Mann and I.F. Morrison, “Digital calculation of impedance for transmission line protection”, IEEE Trans. PAS 90 1 (1971), pp. 270 - 279.

[10] A.G. Phadke, M. Ibrahim and T. Hlibka, “Fundamental basis for distance relaying with symmetrical components”, IEEE Trans PAS-96, 2, (1977), pp. 635 - 646.

[11] J. Izykowski, E. Rosolowski, M.M. Saha, P. Balcerek, M. Fulczyk, “Fault location on three-terminal overhead line and underground cable composite network”, Proceedings of 3rd International Symposium, Modern Electric Power Systems Ű MEPS, Wroclaw, Poland, Sep. 6 - 8 , 2006, pp. 283 - 288.

[12] J. Izykowski, E. Rosolowski, M.M. Saha, “Postfault analysis of operation of distance protective relays of power transmission lines”, IEEE Transactions on Power Delivery, Vol. 22, No. 1, January 2007, pp. 74 - 81

[13] M. Lehtonen, “Transient Analysis for Ground Fault Distance Estimation in Electrical Distribution Networks”, Ph.D. thesis, Technical Research Center of Finland 1992.

[14] B. Liana, M. M. A. Salamaa and A. Y. Chikhanib, “A time domain differential equation approach using distributed parameter line model for transmission line fault location algorithm”, Electric Power Systems Research, Volume 46, Issue 1 , July 1998, pp 1 - 10.

[15] A. Gopalakrishnan, M. Kezunovic, S.M.McKenna, D.M. Hamai, “Fault location using the distributed parameter transmission line model”, IEEE Transactions on Power Delivery, Volume 15, Issue 4, Oct. 2000 pp - 1169 - 1174.

[16] M. Kizilcay, P. La Seta, D. Menniti, M. Igel, “A new fault location approach for overhead HV lines with line equations”, IEEE Power Tech Conference Proceedings 2003, Bologna, 23 - 26 June 2003, Vol. 3, pages: 7.

[17] S. Jamali, V.Talavat, “Fault location method for distribution networks using 37-buses distributed parameter line model”, Eighth IEE International Conference on Developments in Power System Protection, Volume 1, 5 - 8 April 2004, Pp.:216 - 219 Vol.1.

[18] P. Imris and M. Lehtonen, “Transient based earth fault location in 110-kV subtransmission networks”, 15th Power Systems Computation Conference, PSCC 2005, Liege, Belgium, August 22 - 26, 2005.

[19] Y. Liao, “Algorithms for Power System Fault Location and Line Parameter Estimation System Theory”, SSST ’07., Thirty-Ninth South-eastern Symposium on March 2007, Pp.:189 - 193.

[20] J. Rohrig, “Location of Faulty places by measuring with cathode ray oscilloscope”, Elekticität Zeitschrift, 19th Feb. 1931, pp. 241 - 242.

[21] L. Lewis, “Travelling Wave Relations Applicable to Power System Fault Locators”, AIEE Transactions, 1951, pp. 1671 - 1680.

[22] T. Stringfield et. al., “Fault Location for Overhead Lines”, AIEE Transactions, August 1957, pp. 518 - 526.

[23] N. El-Hami, L. Lai, D. Daruvala, and A. Johns, “A new traveling-wave based scheme for fault detection on overhead power distribution feeders,” IEEE Trans. Power Delivery, Vol. 7, pp. 1825 - 1833, Oct. 1992.

[24] P.F. Gale, P.A. Crossley, B. Xu, Y. Ge, B.J. Cory, J.R.G. Barker, “Fault location based on travelling waves”, Fifth International Conference on Developments in Power System Protection, 1993, pp. 54 - 59.

[25] G. B. Ancell, N. C. Pahalawaththa, “Maximum likelihood estimation of fault location on transmission lines using traveling waves,” IEEE Trans. Power Delivery, vol.9, pp. 680 - 689, Apr. 1994.

[26] J. Stokoe, P.A. Crossley, P.F. Gale, “Practical experience with travelling wave fault locators on Scottish Power’s 275 and 400-kV transmission system”, Sixth International Conference on Developments in Power System Protection, (Conf. Publ. No. 434) 25 - 27 March 1997, pp. 192-196.

[27] J. Qin, X. Chen, J. Zheng, “Travelling wave fault location of transmission line using wavelet transform”, Power System Technology Proceedings, POWERCON ’98 International Conference, 18 - 21 Aug. 1998, Vol. 1, pp. 533 Ű 537.

[28] F. H. Magnago, A. Abur, “Fault location using wavelets”, IEEE Trans. Power Delivery, vol. 13, pp. 1475 - 1480, Oct. 1998.

[29] M.M. Tawfik, M.M. Morcos, “A novel approach for fault location on transmission lines”, IEEE Power Eng. Rev. 18, Nov. 1998, pp. 58Ű60.

[30] H. Zijun, C. Yunping, G. Qingwu, “A protection and fault location scheme for EHV line with series capacitor based on travelling waves and wavelet analysis”, International Conference on Power System Technology, Proceedings, PowerCon 2002, Vol. 1, Oct. 2002 pp. 290 - 294.

[31] M. K. Hoi, “Travelling wave fault locator experience on CLP power transmission network”, CEPSI Conf., Fukuoka, Japan, 2002. Paper T2-B-8.

[32] P. Crossley, M. Davidson, P. Gale, “Fault Location Using Travelling Waves”, IEE Colloquium on Instrumentation in the Electrical Supply Industry, 1993, Pp.: 6/1 - 6/3.

[33] J. Qin, X. Chen, J. Zheng, “Travelling wave fault location of transmission line using wavelet transform”, International Conference on Power System Technology Proceedings, 1998, POWERCON ’98, Vol. 1, 18 - 21 Aug. 1998, pp.533 - 537.

[34] H. Heng-xu, Z. Bao-hui, L. Zhi-lai, “A novel principle of single-ended fault location technique for EHV transmission lines”, IEEE Transactions on Power Delivery, Vol. 18, 4, Oct. 2003, pp. 1147 - 1151.

[35] D.W.P. Thomas, C. Christopoulos,Y. Tang, P. Gale,J. Stokoe, “Single-ended travelling wave fault location scheme based on wavelet analysis”, Eighth IEE International Conference on Developments in Power System Protection, Vol. 1, 5 - 8 April 2004, pp. 196 - 199.

[36] M. Gilany, D.K. Ibrahim, E. Tag Eldin; “Traveling-Wave-Based Fault-Location Scheme for Multiend-Aged Underground Cable System”, IEEE Transactions on Power Delivery, Jan. 2007, Vol. 22, 1, pp. 82 - 89.

[37] Hathaway Telefault TWS Technical Data Sheet, “Traveling wave locator”, H.V. TEST (PTY) LTD,South Africa, Online:$http : //www.hvtest.co.za/Company/PDF/Hathaway/TWS_{M}kIII_{B}rochure.pdf.$

[38] R.E. Wilson, “Uses of precise time and frequency in power systems”, Dept. of Eng., Idaho Univ., Moscow, ID; Proceedings of the IEEE Publication, Vol. 79, 7, July 1991.

[39] Z.Q. Bo, G. Weller, F. Jiang, Q.X. Yang, “Application of GPS based fault location scheme for distribution system”, International Conference on Power System Technology, POWERCON’98., 18 - 21 Aug. 1998 Vol. 1, pp. 53 - 57.

[40] W. Zhao, Y. H. Song, W. R. Chen, “Improved GPS travelling wave fault locator for power cables by using wavelet analysis”, International Journal of Electrical Power & Energy Systems, Vol. 23, 5, June 2001, pp. 403 - 411.

[41] K. Xiangjun, Z. Liu, X. Yin, “Fault location using traveling wave for power networks”, The 2004 Industry Applications Conference, 2004. 39th IAS Annual Meeting, IEEE, Vol.4, 3 - 7 Oct. 2004, pp. 2426 - 2429.

[42] P. Chen, B. Xu, J. LiA, “ Traveling Wave Based Fault Locating System for HVDC Transmission Lines”, PowerCon 2006. Oct. 2006, pp. 1 - 4.

[43] T. Takagi, J. Baba, K. Uemura, T. Sakaguchi, “Fault protection based on traveling wave theory, Part 1: Theory”, IEEE PES Summer Meeting, 1977, Mexico City, Mexico, Paper No. A 77, pp. 750 - 3.

[44] H. Dommel, J. Mitchels, “High speed relaying using traveling wave transient analysis”, IEEE PES Winter Power Meeting, New York, Jan. 1978, pp. 214 - 219.

[45] T. Takagi, J. Baba, K. Uemura, T. Sakaguchi, “Fault protection based on traveling wave theory. Part 2: Sensitivity analysis and laboratory test”, In: IEEE PES Winter Meeting, New York City, 1978, Paper No. A 78, pp. 220 - 226.

[46] M. Chamia, S. Liberman, “Ultra high speed relay for ehv/uhv transmission lines-development, design and application”, IEEE Trans. Power Apparatus Syst. PAS-97 (1978), pp. 2104 - 2116.

[47] P.A. Crossley and P.G. McLaren, “Distance protection based on traveling waves”, IEEE Trans. Power Apparatus Syst. PAS-102 (1983), pp. 2971 - 2983.

[48] Y. G. Paithankar and M. T.Sant, “A new algorithm for relaying and fault location based on auto-correlation of travelling waves ”, Electric Power Systems Research, Vol. 8, 2, March 1985, pp. 179 - 185.

[49] E. Shehab-Eldin and P.McLaren, “Traveling wave distance protection-problem areas and solutions”, IEEE Trans. Power Delivery, 3, (1988), pp. 894 - 902.

[50] M. Vitins, “A Correlation Method for Transmission Line Protection”, IEEE Transactions on Power Apparatus and Systems, Vol. PAS-97, 5, Sept. 1978, pp. 1607 - 1617.

[51] S. Rajendra, P. G. McLaren, “Traveling-wave techniques applied to protection of teed circuits: Principle of traveling wave techniques”, IEEE Trans PAS, 1985, 104, pp. 3544 - 3550.

[52] S. Rajendra, P. G. McLaren, “Traveling wave techniques applied to the protection of teed circuits: Multi phase/multi circuit system”,IEEE Trans PAS 1985, 104, pp. 3551 - 3557.

[53] M.M. Mansour, G.W. Swift, “A multi-microprocessor based travelling wave relay: theory and realization”, IEEE Trans Power Delivery, PWRD-1, 1, 1986, pp. 272 Ű 279.

[54] D. Thomas, A. Wright, “Scheme, based on travelling-waves, for the protection of major transmission lines”, IEEE Proc. C, 1988, pp. 63 - 73.

[55] A.T. Johns, R.K. Aggarwal, Z. Bo, “Non-unit protection technique for EHV transmission systems based on fault generated noise, Part 1: Signal measurement”, IEE Proc. C, 141, 1994, 2, pp. 133 - 140.

[56] A.T. Johns, R.K. Aggarwal, Z. Bo, “Non-unit protection technique for EHV transmission systems based on fault generated noise, Part 2. Signal processing”, IEE Proc. C, 141, 1994, 2, pp. 141 - 147.

[57] X. Dong, Y. Ge, B. Xu, “Fault position relay based on current traveling waves and wavelets”, IEEE Power Engineering Society Winter Meeting, 2000, Vol. 3, 23 - 27 Jan. 2000, pp. 1997 - 2004.

[58] A.M. Carter, A.T. Johns, R.K. Aggarwal, Z. BO, “Computer-aided design of a new non-unit protection scheme for EHV teed circuits”, IEE Proc. Gener. Trans. Dist. 143, 1996, Vol. 143, 2, pp. 142 - 150.

[59] Z.Q. Bo, M.A. Redfern, G.C. Weller, “Positional protection of transmission line using fault generated high frequency transient signal”, IEEE Trans. Power Deliv., Vol. 15, 3, 2000, pp. 888Ű894.

[60] Z. Q. Bo, G. Weller, T. Lomas, M. A. Redfern, “Positional Protection of Transmission Systems Using Global Positioning System”, IEEE Transactions on Power Delivery, Vol. 15, 4, Oct. 2000, pp. 1163 - 1168.

[61] E. Vazquez-Martnez, “A travelling wave distance protection using principal component analysis”, International Journal of Electrical Power and Energy Systems, Vol. 25, 6, July 2003, pp. 471 - 479.

[62] V.Pathirana, P. G. Mclaren, “A Hybrid Algorithm For High Speed Transmission Line Protection”, IEEE Transactions On Power Delivery, Vol. 20, 4, Oct. 2005, pp. 2422 - 2428.

[63] H.A. Darwish, A.M.I. Taalab, A.H. Osman, N.M. Mansour, O.P.Malik, “Experimental Evaluation of DWT-Based Current Spike Comparator for Line Protection”, Power Systems Conference and Exposition, PSCE ’06,IEEE PES, Oct. 29th- Nov. 1st, 2006, pp. 1371 - 1379.

[64] C. Aguilera, E. Orduna, G. Ratta, “Adaptive Noncommunication Protection Based on Traveling Waves and Impedance Relay”, IEEE Transactions on Power Delivery, Vol. 21, 3, July 2006, pp. 1154 - 1162.

[65] E. Vazquez, J. Castruita,O.L. Chacon, A. Conde, “A New Approach Traveling-Wave Distance Protection, Part I: Algorithm”, IEEE Transactions on Power Delivery, Vol. 22, 2, April 2007, pp. 95 - 800.

[66] C. Aguilera, E. Orduna, G. Ratta, “Directional Traveling-Wave Protection Based on Slope Change Analysis”, IEEE Transactions on Power Delivery, Vol. 22, 4, Oct. 2007, pp. 2025 - 2033.

[67] Power System Relaying Committee IEEE Std C37.114-2004, “IEEE Guide for Determining Fault Location on AC Transmission and Distribution Lines”, 2005, E-ISBN: 0-7381-4654-4.

[68] B. M. Weedy, B. J. Cory, “Electric Power Systems”, 4th edition, 1998, John Wiley & Sons Ltd.

[69] “Alternative Transient Program RuleBook”, 1987.

[70] L. Prikler, H. Hóildalen, “ATPDraw version 3.5 users’ manual”, SINTEF Energy Research AS, Norway, TR F5680, ISBN 82-594-2344-8, Aug. 2002.

[71] J. R. Marti, “Accurate modeling of frequency-dependent transmission lines in electromagnetic transients simulations”, IEEE Trans. Power Applicat. Syst., vol. PAS-101, pp. 147 - 157, Jan. 1982.

[72] The power system in Finland, FinGrid Oyj Company website: *http ://www.fingrid.fi/portal/in_english/company_info/power_system_in_finland*

[73] Fault statistics 2006. Retrieved from www.nordel.org.

[74] L. Pottonen, “A Method for the Probabilistic Security Analysis of Transmission Grids”, D. Sc. dessertation, TKK Dissertations 42, Espoo 2006, Available online: http://lib.tkk.fi/Diss/2005/isbn9512275929/index.html

[75] L. Sluis, “Transients in Power Systems”, 2001, John Wiley & Sons Ltd,ISBNs: 0-471-48639-6.

[76] R. J. Lopez, “Advanced Engineering Mathematics”, 1st edition, Addison-Wesley, 2001.

[77] H. W. Dommel, “Digital Computer Solution of Electromagnetic Transients in Single- and Multiphase Networks”, IEEE Transactions On Power Apparatus and Systems, Vol. PAS-88, 4, April 1969, pp. 388 - 399.

[78] J. P. Bickford, N. Mullineux, J. R. Reed, “Computation of power system transients”, Stevenage 1976 , IEE monograph series.

[79] E. Clarke. “Circuit analysis of AC power systems: symmetrical and related components”, Wiley, New York, (1943).

[80] P. Chowdhuri, “Electromagnetic Transients in Power Systems”, 1996.

[81] A.T. Johns, S.K. Salman, “Digital Protection for Power Systems”, P. Peregrinus, IEE, London, 1995

[82] R. Rudenberg, “Transient Performance of Electric Power Systems: Phenomena in Lumped Networks”, MIT press reprint, 1969.

[83] Carson, J.R., Wave propagation in overhead wires with ground return. Bell System Technical Journal, Vol. 5, 1926. pp. 539 - 554.

[84] J.L. Blackburn, “Symmetrical Components for Power Systems Engineering”, 1993, Marcel Dekker, Inc. New York, USA.

[85] A. P. S. Meliopoulos, “Power System Grounding and Transients (An Introduction)”, Marcel Dekker Inc., 1988.

[86] A. Ramirez, F. A. Uribe, “A broad range algorithm for the evaluation of Carsont’s Integral”, IEEE Trans. on Power Delivery, Vol.22, No.2, pp. 1188 - 1193, 2007.

[87] F. Rachidi, S.L. Loyka, C.A. Nucci, M. Ianoz, “A new expression for the ground transient resistance matrix elements of multiconductor overhead transmission lines”, Electric Power Systems Research, 65, 2003, pp. 41 - 46.

[88] A. Elhaffar, G. M. Hashmi, M. Lehtonen, “Signal Processing Considerations in Traveling Waves Fault Locators”, MEPS’06, Wroclaw, Poland, 6 - 8 Sep., 2006.

[89] W. Stevenson, “Elements of power system analysis”, McGRAWHILL publishing company LTD., London 1955.

[90] T. Mustafa , D. Thomas, C. Christopoulos, A. Raizer, “Comparison of Simulated and Recorded Transients for Traveling Wave Fault Location ”, 2003 IEEE Bologna Power Tech Conference, June 23th - 26th, Italy.

[91] R. L. Allen, D. W. Mills, “Signal Analysis: Time, Frequency, Scale and Structure”, Wiley IEEE Press, 2004.

[92] G. Ban, L.Prikier, “Fault Location on EHV Lines Based On Electromagnetic Transients”, IEEE/NTUA Athens Power Tech Conference, 1993, pp. 936 - 940.

[93] T. Tibbals, “SEL-LFL Fault Locating and Experience”, SEL Application Guide no. AG93-04, Schweitzer Engineering Laboatory Inc., 1993.

[94] A. Girgis, F. Ham, “A Qualitative Study of Pitfalls in FFT”, IEEE Trans. on Aerospace and Electronic Systems, Vol. AES 16, 4, pp. 434 - 439, July 1980.

[95] E. Styvaktakis, M. H. J. Bollen, I. Y. H. Gu, “A fault location technique using high frequency fault clearing transients”, IEEE Power Eng. Rev. 19, May, 1999, pp. 50Ű60.

[96] K. C. Hwan, R. Aggarwal, “Wavelet transform in power systems: Part 1 General introduction to the wavelet transform”, IEE Power Engineering Journal, Vol. 14, n. 2, pp. 81 - 87, Apr. 2000.

[97] N. I. Elkalashy, A. Elhaffar, M. Lehtonen, H. A. Darwish, M. A. Izzularab, and A. I. Taalab, “Impact of High Resistance Arcing Fault Characteristics on Behavior of Dwt-Based Detection in MV Networks”, Int’l conf. on Electrical and Control Technologies 3 - 4 May 2007, Kaunas, Lithuania.

[98] C. S. Burrus, R. A. Gopinath, H. Guo. “Introduction to Wavelets and Wavelet Transform”, Prentice Hall, New Jersey, 1997.

[99] S. G. Mallat, “A Wavelet Tour of Signal Processing”, 2nd Edition, Academic Press, 1998.

[100] S. G. Mallat, “A theory for multiresolution signal decomposition - The wavelet representation”, IEEE Transactions on Pattern Analysis and Machine Intelligence, Vol. 11, July 1989, p. 674 - 693.

[101] B. N. Singha and Arvind K. Tiwarib, “Optimal selection of wavelet basis function applied to ECG signal denoising”, Digital Signal Processing, Vol. 16, 3, May 2006, pp. 275 - 287.

[102] Z. Q. Bo, R. K. Aggarwal, A. T. Johns, “A novel technique to distinguish between transient and permanent faults based on the detection of current transients”, 4th International Conference on Advances in Power System Control, Operation and Management, 1997, APSCOM-97.,450, Vol. 1, 11 - 14 Nov. 1997, pp. 216 - 220, Vol.1.

[103] C. Kim, H. Kim, Y. Ko, S. Byun, R. Aggarwal, and A. T. Johns, “A novel fault-detection technique of high-impedance arcing faults in transmission lines using the wavelet transform”, IEEE Trans. on Power Delivery, Vol. 17, 4, Oct. 2002, pp. 921 - 929.

[104] S.A. Probert and Y.H. Song, “Detection and classification of high frequency transients using wavelet analysis”, Power Engineering Society Summer Meeting, 2002 IEEE, 25 - 25 July 2002, Vol. 2, pp. 801 - 806.

[105] X. Yansun, J.B. Weaver, D.M. Healy, L. Jian, “Wavelet transform domain filters: a spatially selective noisefiltration technique”, IEEE Transactions on Image Processing, Nov 1994, Vol. 3, 6,pp. 747 - 758.

[106] A.T. Johns, R.K. Aggarwal, Y.H. Song, “Improved techniques for modelling fault arcs an faulted EHV transmission systems”, Generation Transmission and Distribution, IEE Proc., Vol. 141, 2, March 1994, pp. 148 - 154.

[107] D. A. Douglass, “Current transformer accuracy with asymmetric and high frequency fault current”, IEEE Trans-PAS, Vol. 100, 3, March 1981.

[108] A. S.Meliopoulos, S. Zelingher, G. Cokkinides, L. Coffeen, “Transmission level instrument transformers and transient event recorders characterization for harmonic measurements”, IEEE Trans. On Power Delivery, Vol. 8, 3, July 1993, pp 1507 - 1517.

[109] D. Spoor, J. Zhu, P. Nichols, “Filtering Effects of Substation Secondary Circuit on Power System Traveling Wave Transients”, Electrical Machines and Systems, 2005. ICEMS 2005. Proceedings of the Eighth International Conference, Vol. 3, 27 - 29 Sept. 2005 pp.2360 - 2365.

[110] F. Blache, J-P Keradec, B. Cogitore “Stray Capacitances of Two Winding Transformers: Equivalent Circuit Measurements, Calculations and Lowering”, IEEE Industry Applications Society Annual Meeting, 2 - 6 Oct. 1994, pp. 1211 - 1217, Vol.2, 1994.

[111] A. Greenwood, “Electrical Transients in Power Systems”, 2nd edition. John & Wiley & Sons Inc., 1991, pp. 308 - 309.

[112] A. Wright, “Current Transformers, Their Theory and Steady state performance”, Chapman and hall Led, 1968.

[113] J. Hällström, M. Pykälä, “Evaluation of Power transformer Transfer Function from Impulse Test Records”, Nordic Insulation Symposium, NORD-IS03, Tampre, June 11 - 13, 2003. pp. 89 - 96.

[114] L. Ljung, “System Identification, Theory for the user”, 9th printing, Nov. 2006, Prentice-Hall, Inc. .

[115] A. Elhaffar, M. Lehtonen, “High Frequency Current Transformer Modeling for Traveling Waves Detection”, IEEE Power Engineering Society General Meeting, 24 - 28 June 2007, pp. 1 - 6.

[116] A. Abur, F. H. Magnago, “Use of time delays between modal components in wavelet based fault location”, International Journal of Electrical Power and Energy Systems, Vol. 22, 6, Aug. 2000, pp. 397 - 403.

[117] L. M. Wedepohl, “Application of matrix methods to the solution of travelling-wave phenomena in polyphase systems”, IEE Proceedings, Vol. 110, 112, Dec. 1963, pp. 2200 - 2212.

[118] I. Daubechies, “Ten lectures on wavelets”, SIAM, Philadelphia, PA, 1992.

[119] “MATLAB user’s guide”, The Math Works Inc., Natick, MA.

[120] M. Misiti, Y. Misiti, G. Oppenheim, J. Poggi, “Wavelet toolbox user’s guide”, Version 2, The MathWorks.

[121] D.C. Robertson, O. I. Camps, J. S. Mayer, W. B. Gish, “Wavelets and electromagnetic power system transients”, Transactions on Power Delivery, IEEE, Vol. 11, 2, April 1996, pp. 1050 - 1058.

[122] C. E. Shannon, “A Mathematical Theory of Communication”, The Bell System Technical Journal, Vol. 27, pp. 379Ű423, 623Ű656, July and October, 1948.

[123] A. Elhaffar, M. Lehtonen, “Travelling waves based earth fault location in 400-kV transmission network using single-end measurement”, Large Engineering Systems Conference on Power Engineering 2004, LESCOPE-04, 28 - 30 July 2004, pp. 53 - 56.

[124] L. G. Weiss, “Wavelets and Wideband Correlation Processing”, IEEE Sinal Processing Magazine, 13 - 32 Jan. 1994.

[125] J. Liang, S. Elangovan, J. B. X. Devotta, “Application of Wavelet Transform in Travelling Wave Protection”, International Journal of Electrical Power and Energy Systems, Vol. 22, 2000, 8, pp. 537 - 542.

[126] A. Ametani, K. Adachi, T. Narita, “An investigation of surge propagation characteristics on an 1100-kV transmission line”, Electrical Engineering in Japan, Vol. 147, 2, April 30th, 2004, pp. 22 - 29.

[127] T. Hisakado, K. Tanaka, K. Okumura, “A transmission Line Fault Location System using the Wavelet Transform”, Electrical Engineering in Japan, Vol. 140, 4, 2002, pp. 27 - 37.

[128] A. Borghettia, S. Corsib, C.A. Nuccia, , M. Paolonea, L. Perettoa, R. Tinarellia, “On the use of continuous-wavelet transform for fault location in distribution power systems”, International Journal of Electrical Power & Energy Systems, Vol. 28, 9, Nov. 2006, pp. 608 - 617.

[129] C.K. Jung, J.B. Lee, X.H. Wang, Y.H. Song, “Wavelet based noise cancellation technique for fault location on underground power cables”, Electric Power Systems Research, Vol. 77, 10, Aug. 2007, pp. 1349 - 1362.

[130] Z. Galijasevic, A. Abur, “Fault Area Estimation via Intelligent Processing of Fault-Induced Transients”, IEEE Transactions on Power Systems, Vol. 18, No. 4, Nov. 2003, pp. 1241 - 1247.

[131] A. O. Ibe, B. J. Cory, “Traveling Wave Fault Locator for Two and Three Terminal Networks”, IEEE Transactions on Power Delivery, Vol. PWRD-1, 2, April 1986, pp. 283 - 288.

[132] H. Lee, “Development of an Accurate Traveling Wave Fault Locator using Global Positioning Satellites”, Spring Meeting of the Canadian Electrical Association, Montreal, Quebec, March 1993, pp. 197 - 204.

[133] H. Lee, A. M. Mousa, “GPS Travelling Wave Fault Locator Systems: Investigation into the Anomalous Measurements Related to Lightning Strikes”, IEEE Transactions on Power Delivery, Vol. 11, 3, July 1996, pp. 1214 - 1223.

[134] M. da Silva, M. Oleskovicz, D.V.Coury, “A Fault Locator for Three-Terminal Lines Based on Wavelet Transform Applied to Synchronized Current and Voltage Signals”, Transmission and Distribution Conference and Exposition: Latin America, 2006, TDC’06. IEEE/PES Aug. 2006, pp.1 - 6.

[135] N. Chen, X. Zeng, X. Tang, Y. Wang, Z. Liu, “Software for Power Grid Fault Location with Traveling-wave”, International Conference on Power System Technology, PowerCon 2006, Oct. 2006, pp. 1 - 5.

[136] K.E. Martin, “Precise timing in electric power systems”, Proceedings of the 47th IEEE International Frequency Control Symposium, 1993, 2 - 4 Jun. 1993, pp. 15 - 22.

[137] E. W.Dijkstra, “A note on two problems in connection with graphs,” Numer. Math., Vol. 1, pp. 269 - 271, 1959.

[138] T. D. Sudhakar, N. S. Vadivoo, S. M. R. Slochanal, S. Ravichandran, “Supply restoration in distribution networks using Dijkstra’s algorithm”, International Conference on Power System Technology, 2004. PowerCon 2004. 2004, 21 - 24 Nov. 2004, Vol. 1, pp. 640 - 645.

[139] W. Y. Huang, R. Kaczmarek, “Wave Propagation Regime to Point to Faulted Feeder in Mixed Cable-and-Line Distribution Systems with Single-Line-to-Ground Fault”, International Conference on Power Systems Transients (IPSTŠ07) Lyon, France, June 4 - 7, 2007.

[140] S. Qianli, D. Xinzhou, S. Shenxing, S. Bin and H. Jiali, “A new principle of fault line selection for distribution” IEE Seventh International Conference on Developments in Power System Protection, 2001, pp. 379 - 382.

[141] N. Perera, A. D. Rajapakse, A. M. Gole, “Wavelet-based relay agent for isolating faulty sections in distribution grids with distributed generators”, The 8th IEE International Conference on AC and DC Power Transmission, ACDC 2006, 28 - 31 March 2006, pp. 162 - 166.

[142] A. Elhaffar, M. Lehtonen, “An improved GPS current traveling-wave fault locator in EHV transmission networks using few recordings”, International Conference on Future Power Systems, 16 - 18 Nov. 2005.

[143] A. Elhaffar, N. I. Elkalashy, M. Lehtonen, “Experimental Investigations on Multi-end Fault Location System based on Current Traveling Waves”, Power Tech 2007, 1 - 5 July 2007, Lausanne, Switzerland.

[144] M. A. Thurein, I. P. Martin, “Global Positioning System Applications at the Bonneville Power Administration Street”, IEEE Technical Applications Conference and Workshops (Northcon95), 10 - 12 Oct. 1995, pp.244 - 251.

[145] M. R. Mosavi, Z. Habibi, F. Hosseini, “Increasing of DGPS Accuracy Using Recurrent Neural Networks”, 7th International Conference on Signal Processing, 2004 Proceedings. ICSP ’04. 2004, 31 Aug.- 4 Sept. 2004, Vol. 2, pp.: 1574 - 1577.

[146] M. R. Mosavi, “Performance Enhancement of GPS based Line Fault Location Using Radial Basis Function Neural Network”, 5th Annual International Conference and Exhibition on Geographical Information Technology and Applications, Map Asia 2006, 29 August - 1 September, 2006.

Appendix A

Test System Data

In this appendix the transmission line parameters and configuration date and the single-line diagram of 400-kV network configuration are presented.

A.1 A Typical 400-kV Transmission Line Configuration Data

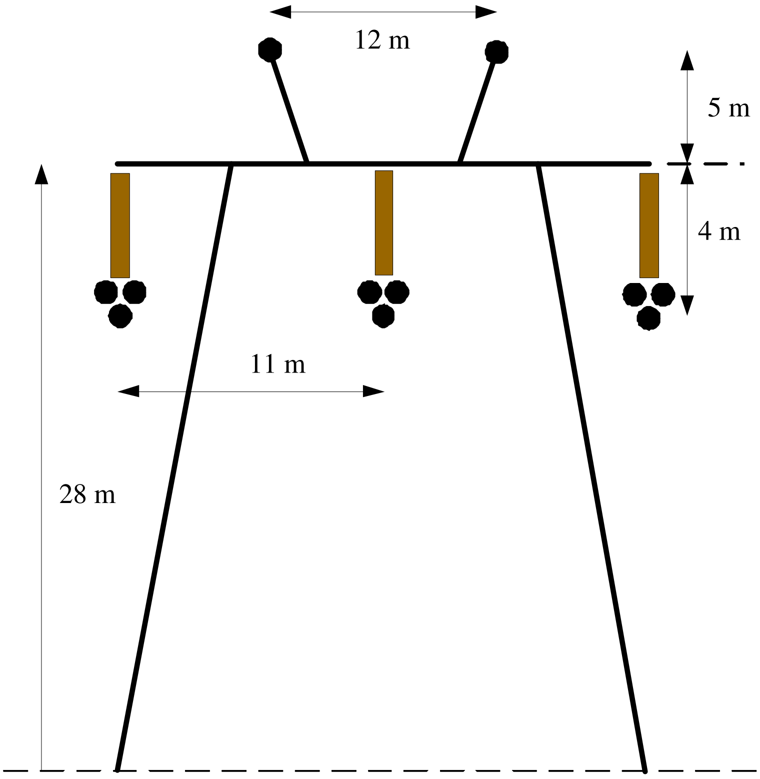

Figure A-1: A typical 400-kV tower construction

A.2 A Typical 400-kV Network

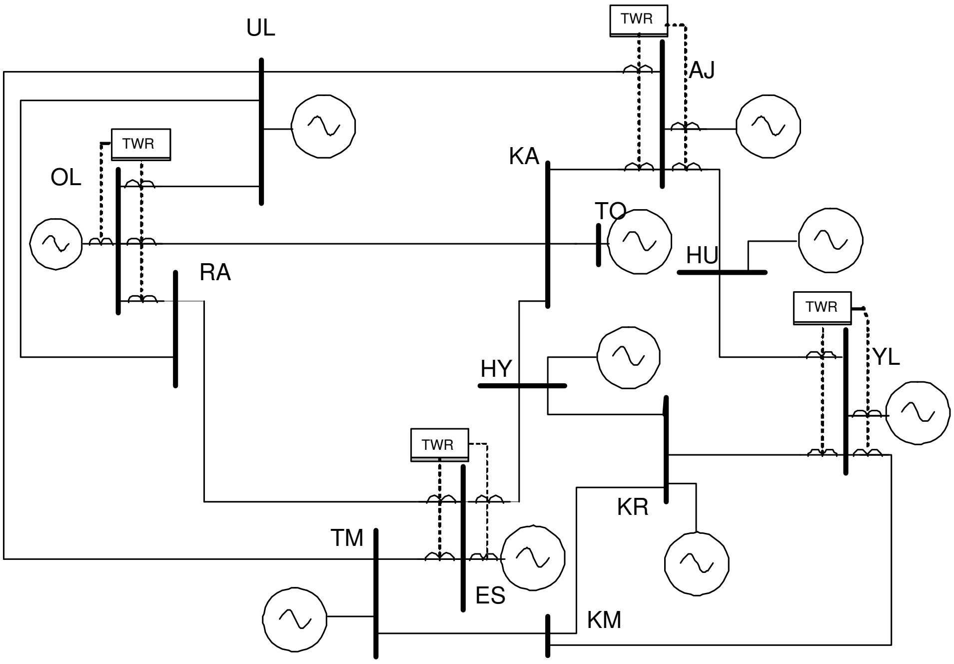

Figure A-2: A typical 400-kV transmission system

Appendix B

Current Transformer Measurements

B.1 CT Open and Short Circuit Calculations

Experimental open and short circuit measurements for a 110-kV, 200/5 current transformer with three secondary windings and separate iron cores are presented.
The CT nameplate data are listed in Table I.

TABLE -I CT DATA

CT data	Core 1	Core 2	Core 3
Primary	200	200	200
Secondary	5	5	5
Class	0.5	0.5	1
VA	60	60	60
Security factor	<3	<3	>10

B.1.1 Short Circuit Test

1) Short Circuit Test from the Primary Winding:

The average of three measurements was considered,

```
Ip=mean([ 10 10.03 10.03]);            %Amp
Vp=mean([ 101.2 101.3 101.4])*1e-3;    %Volt
PF=mean([ .551 .552 .553]);            % Lag
P=mean([ .5587 .5619 .5638]);          % Wat
[Rw Xw]=ShorTest(Ip,Vp,P);
Zscp=Rw+j*Xw;
```

Where: $R_w = P/I_p^2$ and $X_w = \frac{\sqrt{((I_p \times V_p)^2 - P^2)}}{I_p^2}$ and in terms of primary and secondary windings:

$R_w = R_1 + a^2 * R_2$ and $X_w = X_1 + a^2 * X_2$

2) Short Circuit Test from Secondary 1

```
Is1=mean([ 4.88 4.9 4.91]); %amp
Vs1=mean([ 34.55 34.55 34.55]);%volt
PFs1=mean([ .253 .253 .253]);
```

```
Ps1=mean([42.8 42.9 43]);% wat
[Rws1 Xws1]=ShorTest(Is1,Vs1,Ps1);
Zsc1=Rws1+j*Xws1;
```

where: $R_{ws1} = R_p/a^2 + R_2$ and $X_{ws1} = X_p/a^2 + X_2$

3) Short Circuit Test from Secondary 2

```
Is2=mean([ 5.01 5.02 5.01]); %amp
Vs2=mean([ 34.54 34.53 34.53]);%volt
PFs2=mean([ 0.254 0.253 0.255]);
Ps2=mean([43.9 44 44.2]);% wat
[Rws2 Xws2]=ShorTest(Is2,Vs2,Ps2);
Zsc2=Rws2+j*Xws2;
```

where: $R_{ws2} = R_p/a^2 + R_2$ and $X_{ws2} = X_p/a^2 + X_2$

4) Short Circuit Test from Secondary 3

```
Is3=mean([ 4.98 4.96 4.95]); %amp
Vs3=mean([ 89.4 89.4 89.4]);%volt
PFs3=mean([ .564 .571 .574]);
Ps3=mean([252 253.6 254.3]);% wat
[Rws3 Xws3]=ShorTest(Is3,Vs3,Ps3);
Zsc3=Rws3+j*Xws3;
```

Where: $R_{ws3} = R_p/a^2 + R_2$ and $X_{ws3} = X_p/a^2 + X_2$

B.1.2 Open Circuit Test

1) Open Circuit Test from Secondary 1

```
Ios1=([ 45.44e-3 ]); %amp
Vos1=([ 30.32 ]);%volt
Pos1=([ 0.5 ]);% wat
[Rms1 Xms1]=OpenTest(Ios1,Vos1,Pos1);
Zms1=Rms1+j*Xms1;
```

Where $Q_{os}=\sqrt{((I_{os}\times V_{os})^2 - P_{os}{}^2)}$, $R_m = V_{os}^2/P_{os}$, and $X_m = V_{os}^2/Q_{oc}$

2) Open Circuit Test from Secondary 2

```
Ios2=([ 53.8e-3 ]); %amp
Vos2=([ 29.84]);%volt
Pos2=([ 0.5 ]);% wat
[Rms2 Xms2]=OpenTest(Ios2,Vos2,Pos2);
Zms2=Rms2+j*Xms2;
```

3) Open Circuit Test from Secondary 3

```
Ios3=([ 61.53e-3 ]); %amp
Vos3=([ 99.7]);%volt
Pos3=([ .51 ]);% wat
[Rms3 Xms3]=OpenTest(Ios3,Vos3,Pos3);
Zms3=Rms3+j*Xms3;
```

B.1.3 Parallel Secondary Impedances Calculations

```
zp=1e-9+j*1e-9;zs1=1e-9+j*1e-9;zs2=1e-9+j*1e-9;zs3=1e-9+j*1e-9;
%
% Iteration process
for e=1:20
zp=ParZ(Zscp,zs1*a^2,zs2*a^2,zs3*a^2);
zs1=ParZ(Zsc1,zp/a^2,zs2,zs3);
```

```
zs2=ParZ(Zsc2,zp/a^2,zs1,zs3);
zs3=ParZ(Zsc3,zp/a^2,zs1,zs2);
```

Where the function {ParZ(zpsc,zs1sc,zs2sc,zs3sc)} calculates the equivalent impedance of three parallel impedances

```
% zp=zpsc-(zs1sc.*zs2sc.*zs3sc./(zs1sc.*zs2sc+zs1sc.*zs3sc+zs2sc.*zs3sc))
% Division of the impedance between primary and secondary windings
%
% Finding the secondary magnetizing impedances
%
zm1=Zms1-zs1;zm2=Zms2-zs2;zm3=Zms3-zs3;
%
% Finding the equivalents of secondary leakage and magnetizing impedances
%
Zmps1=(zm1.*zs1)./(zm1+zs1);Zmps2=(zm2.*zs2)./(zm2+zs2);Zmps3=(zm3.*zs3)./(zm3+zs3);
SUM=(Zmps1.*Zmps2+Zmps1.*Zmps3+Zmps2.*Zmps3);
%
% Finding the equivalents of primary leakage impedance
%
zp=zp-(Zmps1.*Zmps2.*Zmps3./SUM).*a^2;
```

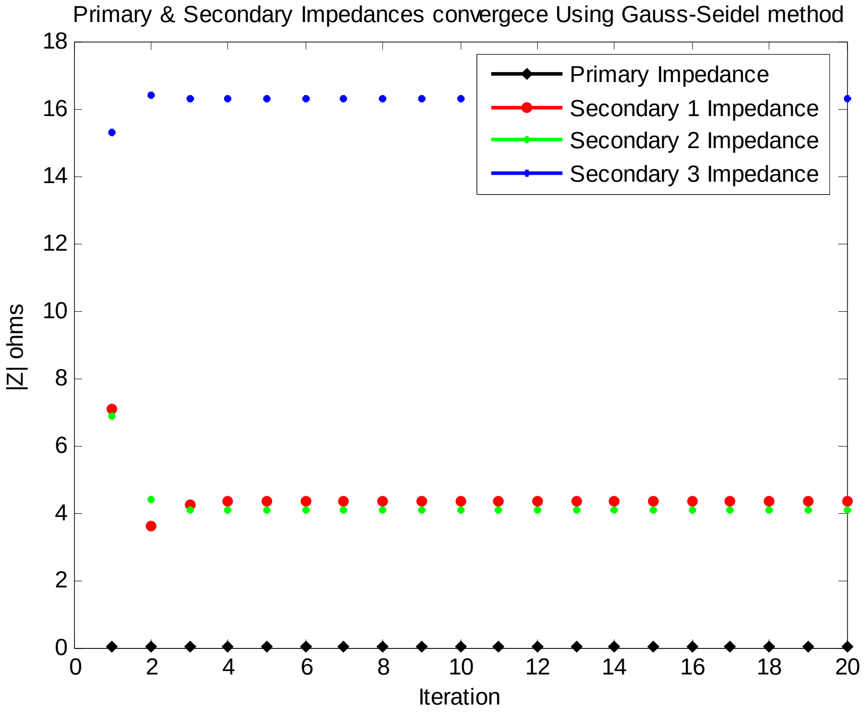

Fig. I1 Gauss-Seidel method Solution of CT parameters

B.1.4 Power frequency correction factor

At 50 Hz the primary current should be corrected according to the following factors:
Ip = CFs*Is
Where

CFs1= 1 + zs1/zm1;
CFs2= 1 + zs2/zm2;
CFs3= 1 + zs3/zm3;

From open and short circuit tests:
Impedance of Primary: Resistance= 5.0241 m ohm and Inductance = 19.5627 µH
Impedance of Secondary 1: Resistance= 0.87535 ohm and Inductance = 13.5602 mH
Impedance of Secondary 2: Resistance= 0.75443 ohm and Inductance = 12.7608 mH

Impedance of Secondary 3: Resistance= 9.8258 ohm and Inductance = 41.3475 mH
Sec 1 Magnetizing Impedance: Resistance= 120.4046 ohm and Inductance 2.2658 H
Sec 2 Magnetizing Impedance: Resistance= 118.6056ohm and Inductance = 1.8451 H
Sec 3 Magnetizing Impedance: Resistance= 373.4883ohm and Inductance = 5.1343 H

Table II: Short Circuit test results: Resistance

R_p [mΩ]	R_{s1} [Ω]	R_{s2} [Ω]	R_{s3} [Ω]
5.0241	0.87535	0.75443	9.8258

Table III: Short Circuit test results: Inductance

L_p [µH]	L_{s1} [mH]	L_{s2} [mH]	L_{s3} [mH]
19.5627	13.5602	12.7608	41.3475

Table IV: Open Circuit test results: Magnetizing Resistance

R_{m1} [Ω]	R_{m2} [Ω]	R_{m3} [Ω]
120.4046	118.6056	373.4883

Table V: Open Circuit test results: Magnetizing Inductance

L_{m1} [H]	L_{m2} [H]	L_{m3} [H]
2.2658	1.8451	5.1343

Sec. 1 Correction factor = 1.00602
Sec. 2 Correction factor = 1.00689
Sec. 3 Correction factor = 1.00689

B.2 Frequency Dependent open & Short Circuit Calculations

The following are the frequency response calculations for a 110 kV, 200/5 current transformer with three secondary windings

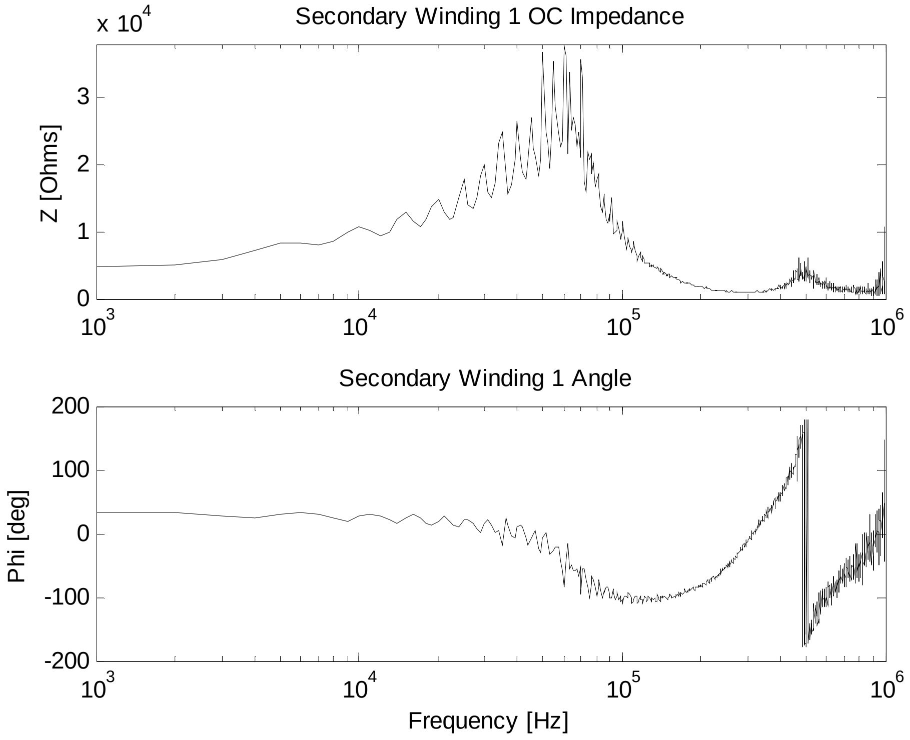

Fig. I2 Open Circuit Test from Secondary 1

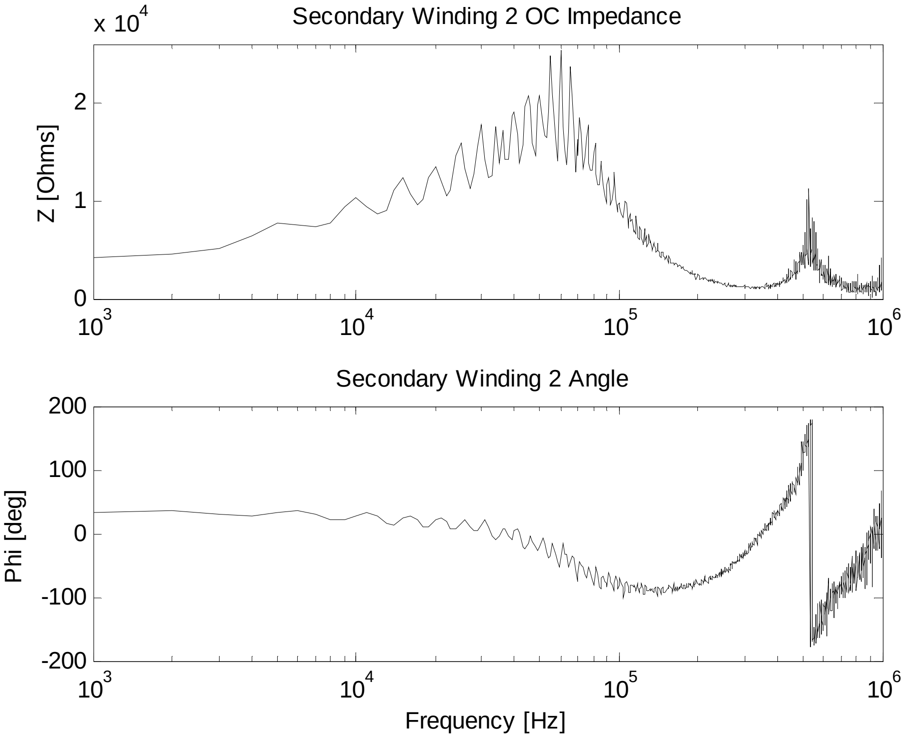

Fig. I3 Open Circuit Test from Secondary 2

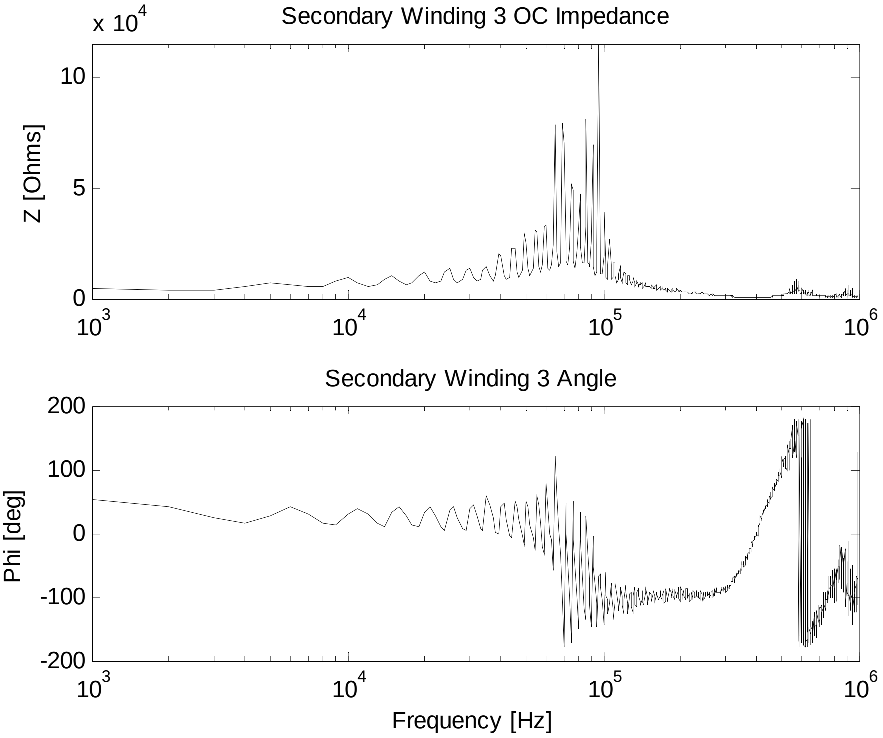

Fig. I4 Open Circuit Test from Secondary 3

B.2.1 Division of the impedance between primary and secondary

Zp=1e-12; Zs1=1e-12;Zs2=1e-12;Zs3=1e-12;
Iteration process

```
for e=1:50
Zp=ParZ(ZPsc,ZS1sc*a^2,ZS2sc*a^2,ZS3sc*a^2);
Zs1=ParZ(ZS1sc,Zp/a^2,ZS2sc,ZS3sc);
Zs2=ParZ(ZS2sc,Zp/a^2,Zs1,ZS3sc);
Zs3=ParZ(ZS3sc,Zp/a^2,Zs1,Zs2);
```

Finding the secondary magnetizing impedances

```
Zm1=ZS1o-Zs1;Zm2=ZS2o-Zs2;Zm3=ZS3o-Zs3;Zmp=ZPo-Zp;
%
% Finding the equivalents of secondary leakage and magnetizing impedances
%
Zmps1=(Zm1.*Zs1)./(Zm1+Zs1);Zmps2=(Zm2.*Zs2)./(Zm2+Zs2);Zmps3=(Zm3.*Zs3)./(Zm3+Zs3);
SUM=(Zmps1.*Zmps2+Zmps1.*Zmps3+Zmps2.*Zmps3);
```

Finding the equivalents of primary leakage impedance

```
Zp=Zp-(Zmps1.*Zmps2.*Zmps3./SUM).*a^2;

end
ZS1=Zs1(1:length(FS1));%/max(Zs1(1:length(FS1)));
ZS2=Zs2(1:length(FS2));%/max(Zs2(1:length(FS2)));
ZS3=Zs3(1:length(FS3));%/max(Zs3(1:length(FS3)));
ZP=Zp(1:length(FP));%/max(Zp(1:length(FP)));
Ls1=imag(ZS1)/(100*pi);Ls2=imag(ZS2)/(100*pi);Ls3=imag(ZS3)/(100*pi);
Lp=imag(ZP)/(100*pi);
```

B.2.2 Frequency dependent correction factor

The primary current should be corrected according to the following factors:
Ip = CFFs*Is

First Resonance capacitance was obtained from open circuit test of the
f10=35 kHz; w10=2*pi*f10; f20=33 kHz; w20=2*pi*f20; f30=48 kHz; w30=2*pi*f30;

$$C_{s1} = \frac{1}{(2\pi f_1)^2 \times I_{s1}}$$

$$C_{s2} = \frac{1}{(2\pi f_2)^2 \times I_{s2}}$$

$$C_{s3} = \frac{1}{(2\pi f_3)^2 \times I_{s3}}$$

Table VI: Open Circuit test results: Secondary winding Capacitance

C_{s1} [nF]	C_{s2} [nF]	C_{s3} [nF]
1.5249	1.8228	0.26589

$$\text{CFs1} = 1 + \frac{Z_{s1}}{Z_{m1}} + \frac{Z_{s1}}{Z_{Cs1}}$$

$$CFs2 = 1 + \frac{Z_{s2}}{Z_{m2}} + \frac{Z_{s2}}{Z_{Cs2}}$$

$$CFs3 = 1 + \frac{Z_{s3}}{Z_{m3}} + \frac{Z_{s3}}{Z_{Cs3}}$$

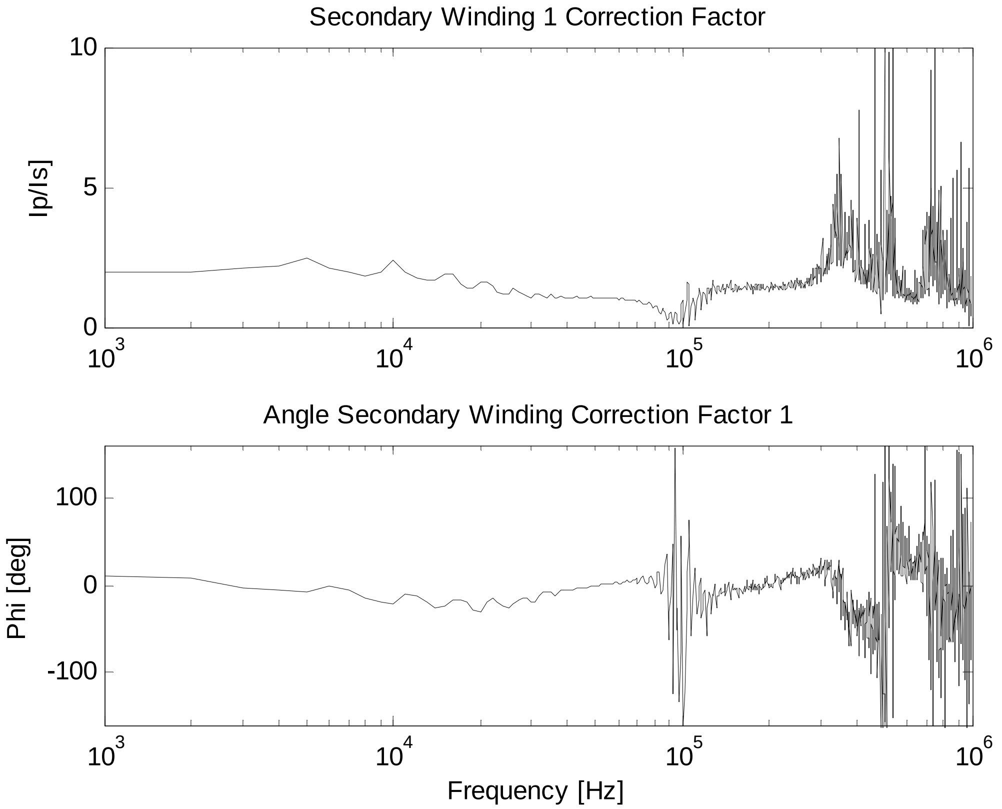

Fig. I5 Secondary winding 1 correction factor

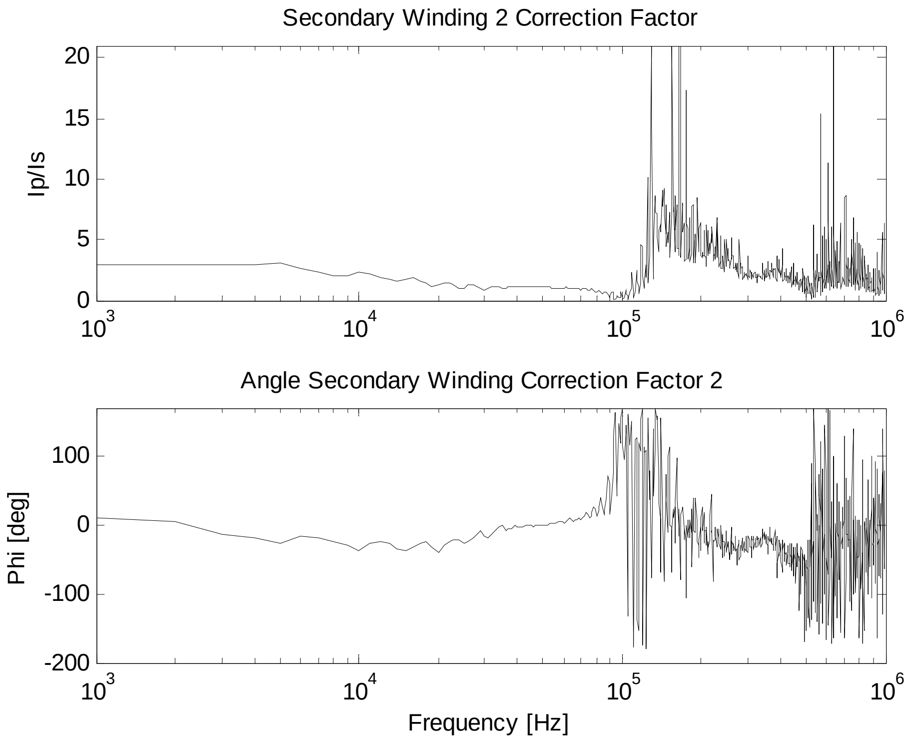

Fig. I6 Secondary winding 2 correction factor

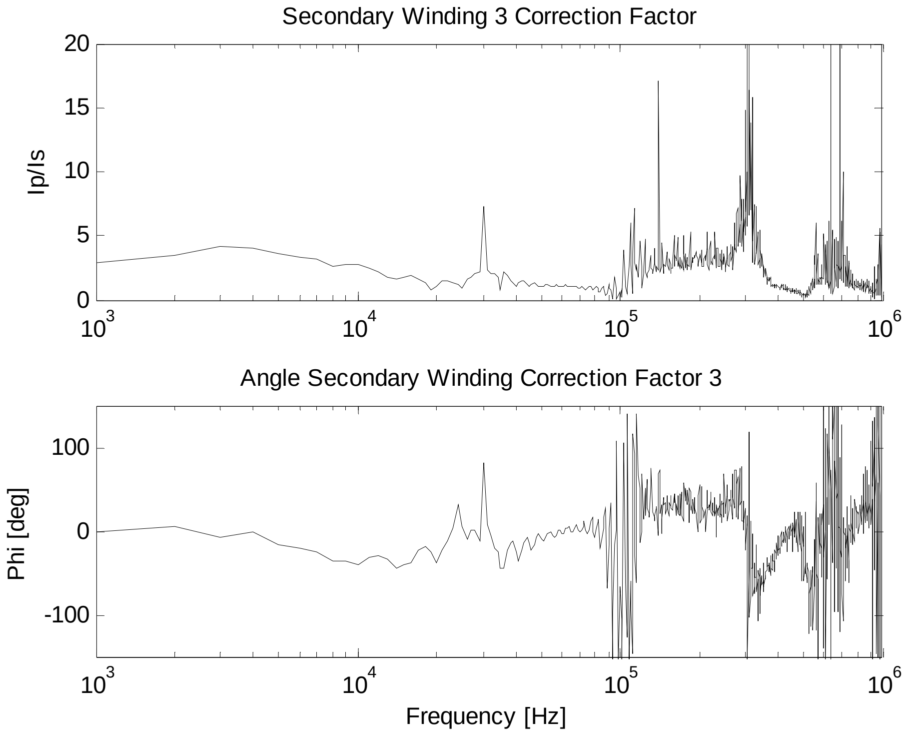

Fig. I7 Secondary winding 3 correction factor

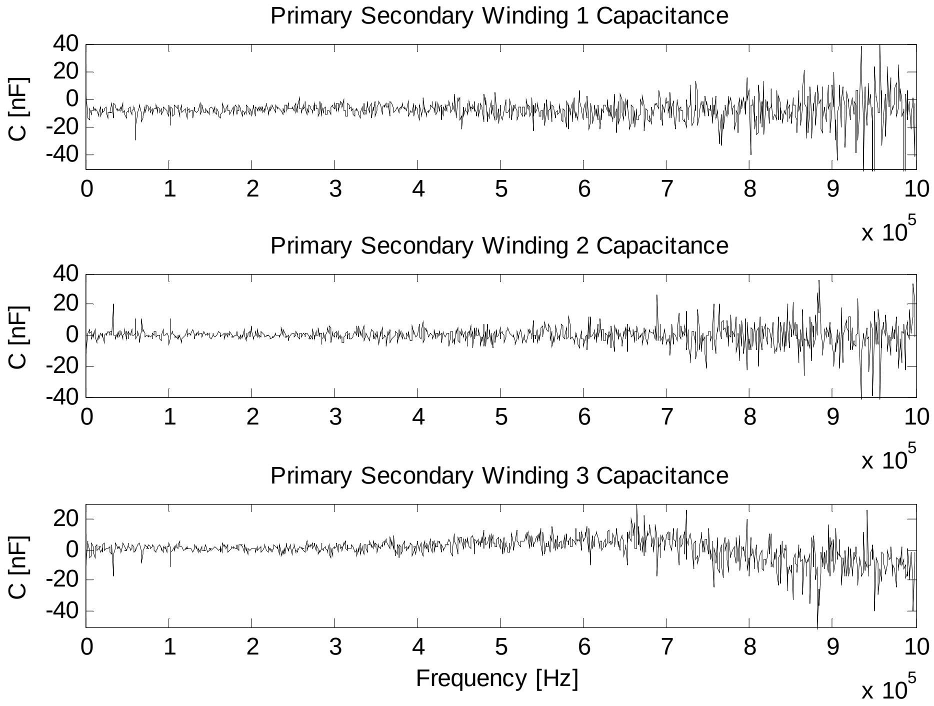

Fig. I8 Primary to Secondary windings capacitances

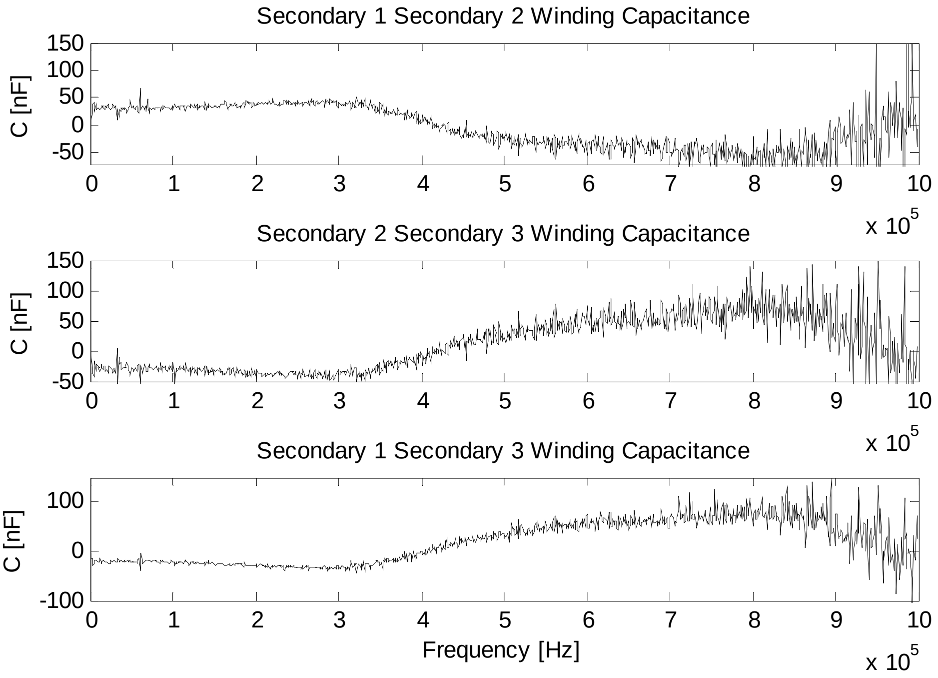

Fig. I9 Secondary to Secondary windings capacitances

Appendix C

MATLAB and ATP Functions used in Fault Distance Calculation

- **function [Ig Ia1 Ia2]=Phase2Modal(Ia,Ib,Ic)**

```
% Modal Analysis using Clarke's transformation matrix
b=([1/sqrt(3) 1/sqrt(3) 1/sqrt(3)
 sqrt(2/3) -1/sqrt(6) -1/sqrt(6)
 0  1/sqrt(2) -1/sqrt(2)]);
 IM=b*[Ia Ib Ic]';
 Ig=IM(1,:);   % Ground mode (mode 0) signal
 Ia1=IM(2,:);  % Aerial mode (mode 1) signal
 Ia2=IM(3,:);  % Aerial mode (mode 2) signa
```

- **function [OptWAVE]=OptWLTComp(x,level)**

```
%using different mothr wavelets to compare
err(1)=WLTComp(x,'db2',level);
….
err(32)=WLTComp(x,'bior6.8',level);
[m n]=min((err));%clear(ErrMatr);
Mothers=num2str(['db2   ';'db4   ';'db6   ';'db8   ';'db10  ';...
    'db15  ';'db20  ';'db30  ';'sym4  ';'sym6  ';'sym8  ';...
       'sym10 ';'coif1 ';'coif2 ';'coif3 ';'coif4 ';'coif5 ';...
       'bior1.1'; 'bior1.3';'bior1.5';...
        'bior2.2'; 'bior2.4' ; 'bior2.6'; 'bior2.8';...
        'bior3.1'; 'bior3.3' ; 'bior3.5'; 'bior3.7';...
        'bior3.9'; 'bior4.4' ; 'bior5.5'; 'bior6.8']);
[OptWAVE]=num2str(Mothers(n,:))
```

- **function [err]=WLTComp(x,wave,level)**

```
di=[];cdi=[];
[c,l] = wavedec(x,level,wave);
ca = appcoef(c,l,wave,level);
for i=1:level
cd=detcoef(c,l,i);
cdi=[cd;cd];
end
a0 = waverec(c,l,wave);
err = norm(x-a0);
```

- **function [MulDWT]=MultiLevelDWT(Signal,levels,type)**

```
Signal_length=length(Signal);
di=[];
% Perform decomposition at level 'levels' of Signal using 'type' mother wavelet,
[c,l] = wavedec(Signal',levels,type);
for i=1:levels
    % Reconstruct detail coefficients at 'levels=i' from the wavelet decomposition structure [c,l]
cd=wrcoef('d',c,l,type,i);
di=[di;cd'];
end
k=0;
for i=levels:-1:1;
```

```
k=k+1;
   d(k,:)=di(i,:);
end
    % Reconstruct approximation at 'levels',from wavelet decomposition structure [c,l].
a=wrcoef('a',c,l,type,levels);
MulDWT=[a';d];
```

ATP 400-kV Line Configuration Data for Line/Cable Module of ATPDraw

```
BEGIN NEW DATA CASE
JMARTI SETUP
$ERASE
BRANCH  IN___AOUT__AIN___BOUT__BIN___COUT__CIN___DOUT__DIN___EOUT__E
LINE CONSTANTS
METRIC
  10.374 0.05165 4         3.284    11.     24.     10.     45.   30.       3
  20.374 0.05165 4         3.284    0.0     24.     10.     45.   30.       3
  30.374 0.05165 4         3.284    -11.    24.     10.     45.   30.       3
  4  0.5    0.36 4        1.46     6.     33.     20.     0.0   0.0       0
  5  0.5    0.36 4        1.46    -6.     33.     20.     0.0   0.0       0
BLANK CARD ENDING CONDUCTOR CARDS
   2300.      50.                      128.019     1
   2300.    0.005                      128.019     1   8  5
BLANK CARD ENDING FREQUENCY CARDS
BLANK CARD ENDING LINE CONSTANT
               1       0       0   3.E-8
             0.3      30       0       1       0       0       0
             0.3      30       0       1       0       0       0       0
$PUNCH
BLANK CARD ENDING JMARTI SETUP
BEGIN NEW DATA CASE
BLANK CARD
```

ATP 110-kV Line Configuration Data for Line/Cable Module of ATPDraw

```
BEGIN NEW DATA CASE
JMARTI SETUP
$ERASE
BRANCH  IN___AOUT__AIN___BOUT__BIN___COUT__CIN___DOUT__DIN___EOUT__E
LINE CONSTANTS
METRIC
  10.374 0.05165 4         3.284    4.2     16.     10.     0.0   0.0       0
  20.374 0.05165 4         3.284    0.0     16.     10.     0.0   0.0       0
  30.374 0.05165 4         3.284    -4.2    16.     10.     0.0   0.0       0
  4  0.5    0.36 4        1.46     2.2    19.7     13.     0.0   0.0       0
  5  0.5    0.36 4        1.46    -2.2    19.7     13.     0.0   0.0       0
BLANK CARD ENDING CONDUCTOR CARDS
   2300.    7.5E4                        51.5     1         1
   2300.      50.                        51.5     1         1
   2300.     0.05                        51.5     1   8  8   1
BLANK CARD ENDING FREQUENCY CARDS
BLANK CARD ENDING LINE CONSTANT
               1       0       0   3.E-8
             0.3      30       0       1       0       0       0
             0.3      30       0       1       0       0       0       0
$PUNCH
BLANK CARD ENDING JMARTI SETUP
BEGIN NEW DATA CASE
BLANK CARD
```

ISBN 978-951-22-9244-8
ISBN 978-951-22-9245-5 (PDF)
ISSN 1795-2239
ISSN 1795-4584 (PDF)